THE PRODUCTION OF POLYMER FIBRES WITH HIGH PERFORMANCE

&

FT-RAMAN SPECTROSCOPY AT 1.3μm

A thesis submitted to the
University of Southampton
in support of candidature for
the degree of
Master of Philosophy

by
Colm Donal Murphy
BSc. (Hons.)

Department of Chemistry, June 2002

UNIVERSITY OF SOUTHAMPTON

ABSTRACT

FACULTY OF SCIENCE
CHEMISTRY

Master of Philosophy

THE PRODUCTION OF POLYMER FIBRES WITH HIGH PERFORMANCE.
&
FT-RAMAN SPECTROSCOPY AT1.3μm

by Colm Donal Murphy

The work described in this thesis involved the role of molten metal baths in the quench cooling of polyethylene in the production of polymer fibres with high performance. A melt-spinning rig was designed and constructed. **Chapter 2** describes how polymer fibres were produced from the melt by spinning fibres through a reservoir of molten melt which was held at temperatures near the melting point of the polymer. Polyethylene fibres with a tensile modulus of the order of 25 GPa and tensile strength approaching 1 GPa were produced by a process of melt spinning followed by cold drawing to a draw ratio of 15.

Raman spectroscopy is an invaluable analytical tool used in a multitude of applications. The ease and versatility of the technique provides a simple method for identification and studying crystallinity of specimens. The foremost choice of laser source for FT-Raman has been the continuous wave Nd^{3+}:YAG solid state laser operating at 1.064 μm. **Chapter 4** investigates the possibility of using the 1.319 μm lasing emission from the Nd^{3+}:YAG laser as an alternate source. The sensitivity of the source is determined, applications are illustrated and the limitations commented upon.

AFFIDAVIT

The investigations described in this Chapters 2 and 4 involved collaboration with other scientists, namely Dr. Yvonne West and Dr. Shilin Lu during their postdoctoral appointments to the project in question. Where this was the case, i.e. the design and construction of the original polymer processing rig or the results from polyethylene fibre production, it has been clearly stated.

do mo thuismitheoirí, Siobhán agus Diarmuid

Acknowledgements

Right so...I'd just like to say a few words as a mighty big *go raibh míle maith agaibh* to a whole bunch of characters for their help, generosity and support throughout the campaign....

Firstly, the man himself, my supervisor, Professor Patrick Hendra for giving me this opportunity, for his support, advice and great chats on music... not forgetting the kind loan of the fiddle when mine was at the surgery.

To Dr. Yvonne West for giving me so much encouragement and for helping with the computer stuff .... and all that for just a bottle of Bailey's.... *cheers Yvonne.*

To Dr. Andrea Russell for her patience and kindness in putting up with me wandering in and out of the office over this past year as well as the use of the computer for the write-up.

To the various muckers of the research group past and present for their support and friendship not to mention some really lousy jokes: Liz, Andy Brim, Andy Bro, Shelly, Maureen and especially Malcolm (for selling me a grand Ford Sierra); and those carrying on the group traditions with Andrea, with a special word of thanks to Fabrice, Anne and Abbe.

To my fellow "Paddies" Tomás Harrington and Stewart Meehan for the great *craic, ceol agus uisce beatha* at Monte and 303 Burgess Rd; and all the TNC back in Cork especially David Bevan for sending the minutes of all the "meetings" I've missed.

To Wendy, Louise, Colin and Paul for all their help in the preparation of this thesis.

To the staff of the Chemistry Department, Mike and Bruce in the Electronics Workshop, all the gang in the Engineering Workshop (especially John for fixing the polymer rig after I'd turned the volume up to 11), all at Chemistry Stores, the tea ladies (and Anne ... for the words of wisdom and all the complements about my legs !!) Also to all the people I knew who made my time in the University at Southampton such an enjoyable one, with a special mention to all the wasters in "Cold Fusion" ... *ye'll win nathin'* !

To Mary and Martin for rescuing me and putting a roof over my head at No. 48, to Todd for teaching me all about the aviaries and apiaries, Ken for his sordid organic tit bits....and all from my previous abode at 71 Welbeck Ave.

To all of the fine musicians (and fantastic friends) I've had the privilege playing with around Southampton and further afield, especially Arnie, Pat, Jock, Jamie, Brendan, Mike, Donal, Broderick, Seanachaí, The Velvet Doonicans and all at "The Heads" *It's been a great howl !*

To the Murphy clan: my sisters and brothers, the extending family and above all, my brilliant parents *Siobhán agus Diarmuid, . Táim fíor bhuíoch as ucht gach cabhair a thug sibh dom.*

CONTENTS

CHAPTER 1 : THE RELATIONSHIP BETWEEN MOLECULAR STRUCTURE AND MECHANICAL PERFORMACE

1.1 Introduction 1
1.2 The structure of polymer melts and solids 2
1.2.1 Crystallisation from static dilute solutions 3
1.2.2 Crystallisation from condensed systems 5
1.2.3 The nature of the fold surface 8
1.2.4 Extended chain crystals 13
1.3 Stress in semi-crystalline polymers 13
1.3.1 Deformation of single crystals and Peterlin's model 14
1.3.2 Deformation of melt crystallised polymers 16
1.3.3 Deformation of molecules in solution 18
1.4 Stress in melts 19
1.4.1 The structure of the static polymer melt 20
1.4.2 Strain Induced Crystallisation 22
1.5 The Young's modulus of drawn fibres 24
1.6 References for Chapter 1 25

CHAPTER 2 : NOVEL METHODS FOR THE PRODUCTION OF HIGH PERFORMANCE POLYMER FIBRES

2.1 Developments in Polyethylene Fibre Production 28
2.2 The Processing of Polymer Melts 30
2.3 Fibre Spinning Rig 31
2.3.1 The Extruder 33
2.3.2 The Flange and Die Block Assembly 34
2.3.3 The Molten Metal Bath 37
2.3.4 The Spin line and Wind-off facility 37
2.4 Mechanical Testing 38
2.4.1 Fibre Cold-Drawing Apparatus 40
2.5 Annealing 41
2.5.1 Theoretical treatment 41
2.5.2 Effects of Annealing 42
2.6 Initial Investigations of the Polymer Processing Rig 42
2.7 Initial investigations with Hostalen GF4760 50
2.7.1 Results 51
2.8 References for Chapter 2 55

CHAPTER 3 : VIBRATIONAL SPECTROSCOPY : THEORY AND INSTRUMENTATION

3.1	Vibrational Spectroscopy	56
	3.1.1 Infrared Activity	61
	3.1.2 The Raman Effect	62
3.2	Fourier Transform Instrumentation	67
	3.2.1 From Interferogram to Spectrum	68
	3.2.2 Data Point Resolution	72
	3.2.3 Nyquist Criterion	73
	3.2.4 The advantages of FT over Conventional Spectrometers	73
3.3	Practical Spectroscopy	75
	3.3.1 Practical Infrared Spectroscopy	75
	3.3.2 Practical FT Raman Spectroscopy	76
3.4	The Fluorescence problem with Raman Spectroscopy	77
3.5	References for Chapter 3	79

CHAPTER 4 : FT-RAMAN SPECTROSCOPY AT 1.319 MICROMETERS

4.1	System Characteristics	81
	4.1.1 The laser source	81
	4.1.2 Laser filters: Rayleigh rejection filters and bandpass filters	82
4.2	The design of a NIR FT-Raman instrument to operate at 1.319 μm	84
	4.2.1 Instrument response function	86
	4.2.2 Signal to noise performance	89
4.3	Applications and selected results	93
	4.3.1 Use of the FT-Raman spectrum of Na_2MoO_4 to study sample heating by the 1.319 μm laser	93
	4.3.1.1 Experimental	94
	4.3.1.2 Results and discussion	95
	4.3.1.3 Conclusion	99
	4.3.2 The Ratio of Stokes and anti-Stokes line intensities at 1.319 μm as a method of sample temperature measurement	99
	4.3.3 Fluorescence rejection as a function of excitation wavelength	102
4.4	Discussion	108
4.5	References for Chapter 4	110

CHAPTER 5 : CONCLUSIONS 111

1. Chapter One: The relationship between molecular structure and mechanical performance

1.1 Introduction.

Polymeric materials constitute the principle proportion of many things we use in our everyday life. Natural biological polymers are present in our bodies and our food - while non-biological, synthetic polymers make up a multitude of convenience goods available in modern times. Although natural polymers have long being known to exist, synthetic polymers have a very short history and have only been widely used since the middle of the last century. Nowadays, polymers represent a very large section of the chemical industry. The plastics industry commenced operations in the mid 1830's by utilising natural rubber, and later derivatives of cellulose were discovered and commercialised. Production of synthetic polymers started in the early 1900's with the group of phenol-formaldehyde resins (one of which is commercial "Bakelite") and the use of styrene in synthetic rubbers. However, the discovery of these synthetic polymers was made much earlier: polystyrene in 1839, poly(ethylene glycol) in 1860 and isoprene in 1879, to name a few examples[1].

In 1920, the concept of macromolecules was proposed and accepted mainly because of Staudinger's investigations based upon the polydispersity of synthetic polymers[2]. Since then, many scientists have studied in the fields of polymer chemistry and polymer physics to investigate and characterise the structure and properties of polymers. The very size of these materials has led to many models being proposed, particularly in order to understand the morphologies of polymer chains in the liquid and solid phase, models which are still a subject of some controversy.

This chapter presents a review of contemporary ideas and understanding, using Polyethylene (PE) as the most appropriate illustration, having received more attention than any other polymer by the scientific community to date.

1.2 The structure of polymer melts and solids

Most polymers are semi-crystalline and so display complex morphologies in their solid state. Crystalline polymers are described as being composed of an ordered or crystalline phase, where the chains are packed parallel to one another, surrounded by a disordered or amorphous phase, thus defining a two-phase model. Early X-ray diffraction studies on the morphology of polymers[3] showed that perfect order could not be achieved in polymer crystals. Thus rings in X-ray diffraction patterns appear broad and diffuse, densities are intermediate between those of the crystal and those of a liquid and melting points are broad, etc.[4].

From X-ray diffraction studies, Bunn[5] gave a detailed description of the unit cell of the polyethylene crystal as shown in Figure 1.1.

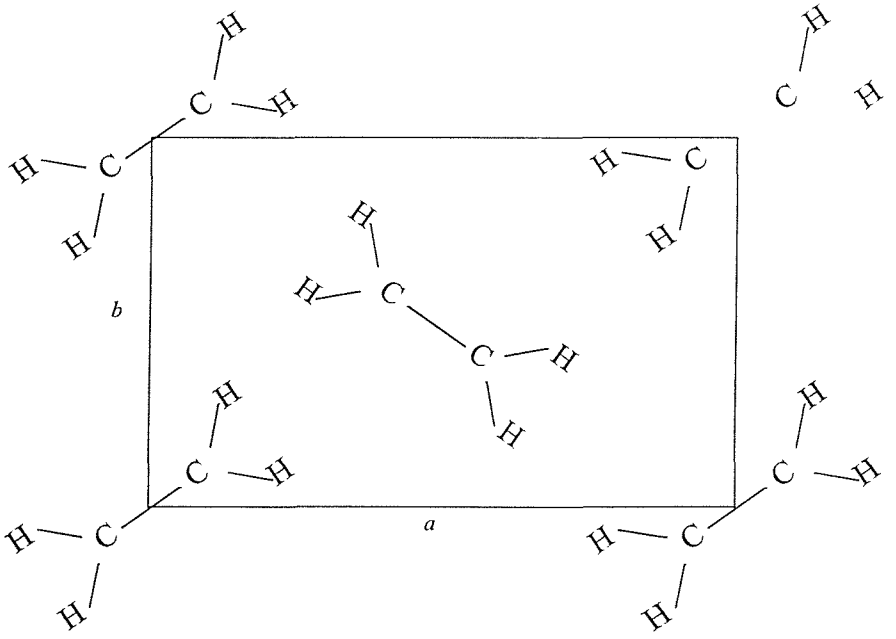

Figure 1.1 : The crystal structure of polyethylene. a = 7.4 Angstroms, b=4.9 Angstroms and c= 2.5 Angstroms (c lies normal to the plane of the page)[6]

The crystalline polyethylene exists in an orthorhombic structure with a D_{2h} point group, containing two molecular chains and four CH_2 groups per unit cell.

In dealing with the crystalline state, two different cases must be addressed. A distinction must be made between the material generated by crystallisation from dilute solutions and that generated from melts, since from dilute solution, a crystal entity can be isolated and it can be studied independently of others, which is not the case for phases generated from melts and concentrated solutions.

1.2.1 Crystallisation from static dilute solutions.

In 1957 several groups of different workers such as Keller[7] and Till[8] showed how single crystals of polyethylene could be grown from dilute solutions (<0.1%) in xylene at 60°C. These lamella-like crystals were generally lozenge shaped hollow pyramids which collapsed under their own weight when drying and were of the order of 50-200 Å thick (as shown in Figure 1.2).

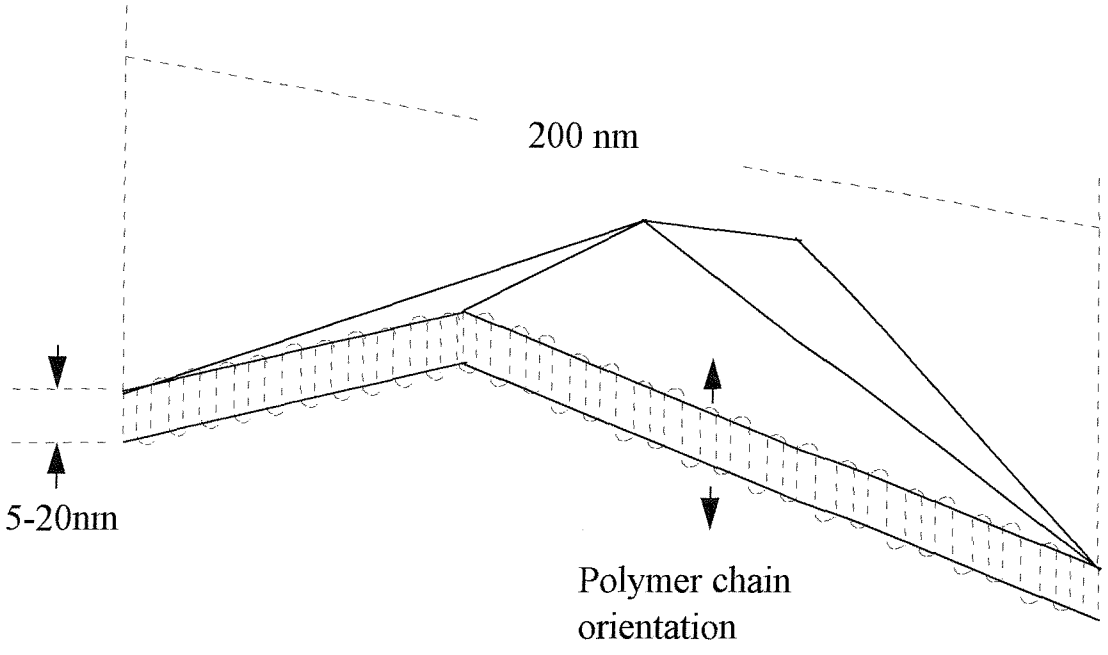

Figure 1.2: showing an illustration of a solution-grown polymer crystal.

Using electron microscopy and electron diffraction, Keller[9] demonstrated that the polymer chain axes in the crystal body were essentially perpendicular to the large flat faces of the crystal, and since the chains were know to be ~ 2000Å long with the crystal thickness of the order of 100Å it was concluded that the molecules in the crystal had to be folded back upon themselves. These crystals were expected to exhibit the properties of the pure crystalline material. However, density and heat of fusion experiments showed that they had a significant amorphous content which it was presumed must be due to the surface, i.e. of molecular folding, and/or to polymer molecules adsorbed on the crystal surface. Much debate then followed as to the nature of the chain folding. Different models were proposed as shown in Figure 1.3, where the surface is either represented by adjacent re-entries with regular or irregular folds or a complete model ("switchboard" model) with adjacent and non-adjacent re-entries with regular and irregular folds.

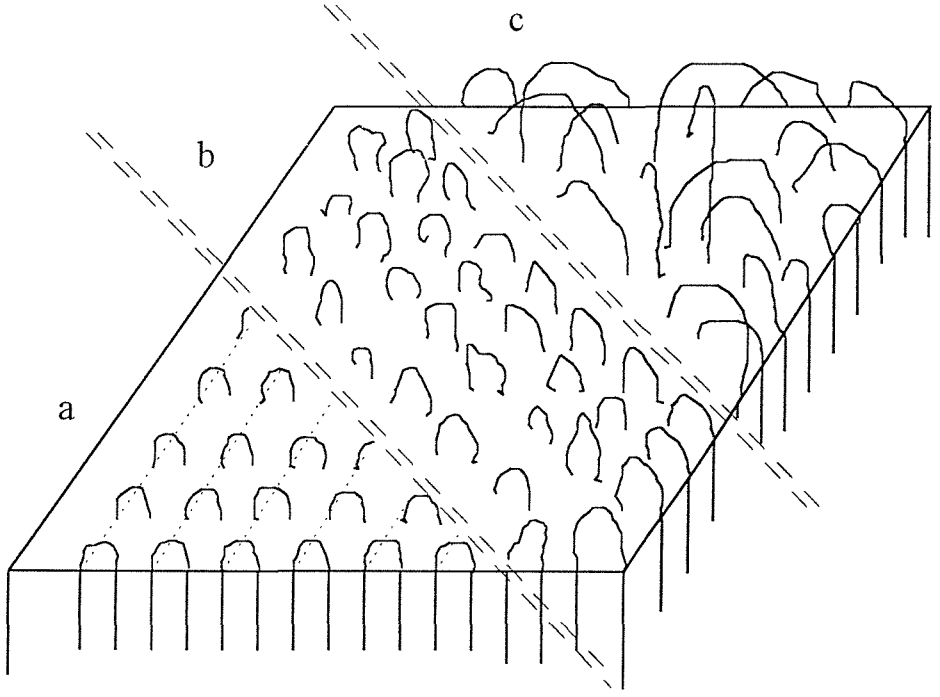

Figure 1.3 Schematic representation of models of the fold surface in polymer lamellae

a - regular adjacent re-entry

b - adjacent re-entry with loose folds

c - non-adjacent re-entry

Mandelkern[10] put forward the idea that many physical properties of dilute solution grown crystals of polyethylene cannot be explained by a smooth regularly folded surface. Keller, however, is a supporter of this model for a number of reasons, such as for example the perfect orientation of the chains in crystals[9].

Atomic models have shown[11] that at least five carbon atoms are required to complete the sharp fold of a chain. However, selective degradation studies[12] showed that the chain length distribution of the segments removed was around C_{11}, which strongly favours irregular folds rather than adjacent re-entries.

The controversy on the nature of chain folding in single crystals still exists, but it seems that the "switchboard" model does not apply to single crystals[13]. In the case of polymers crystallised from condensed systems, the situation is much more complex due to the higher incidence of molecular entanglements.

1.2.2 Crystallisation from condensed systems

Following the discovery of single lamellar crystals grown from solution came the search for similar structures in melt crystallised material. Compact multi-layer polyhedral crystals were found to form from concentrated solutions[14] (0.3-45% in the case of polyethylene in xylene) and were termed hedrites or axialites. These species are thought to be in some respects an intermediate to melt crystallisation, since in some spherulites the nuclei closely resemble hedrites[15].

It is possible to grow single crystals from the melt[13] in some special cases (slow growth rate in thin films), but usually, due to the entangled nature of macromolecules in the melt and the almost inevitably rapid rate of crystallisation, spherulitic growth occurs. Spherulites are recognised by their characteristic Maltese cross pattern when thin sections are viewed between crossed polarisers under an optical microscope. The arms of the Maltese Cross lie parallel to the extinction directions of the polariser and analyser. On rotating the specimen in its own plane, the cross remains stationary

implying that all radii are crystallographically equivalent. The basic structure is quite well understood, appearing to consist of a large number of crystallites (of comparable thickness to solution grown single crystals) radiating in all directions from a central point - the nucleus. The nucleus can be homogeneous (a molecular stem) or heterogeneous (an impurity). Figure 1.4 illustrates how the spherulite develops from a homogeneous nucleus, developing through sheaf like embryos before attaining its characteristic spherical envelope.

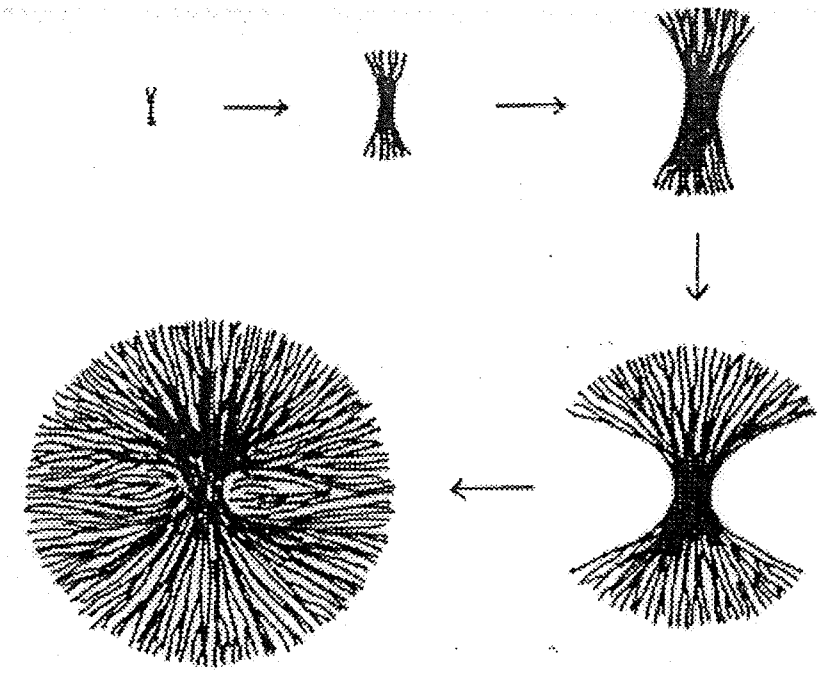

Figure 1.4: The development of a spherulite from a homogeneous nucleus

At the initial stages of crystallisation spherulites appear spherical but at later stages they impinge on their neighbours. In cases where spherulites are nucleated simultaneously, the boundaries between them are straight, but if nucleated at different times they are different in size when they impinge on one another, causing their boundaries to form hyperbolae.

X-ray diffraction studies of the spherulites[16] indicates that the fibril axis (the c axis) of the molecules is oriented tangentially to the radial growth direction of the spherulites. The c axis is perpendicular to the lamellar flat surface which shows a structural resemblance to a single crystal solution grown crystal. It has been shown that the lamellae for polyethylene have a screw like twist along their b axis[16], on the radius of the spherulite. The distance corresponding to one half pitch of the screw gives rise to the distinctive banded appearance of the Maltese Cross pattern. The radiating array of fibrillar structural units in the spherulite is shown schematically in Figure 1.5.

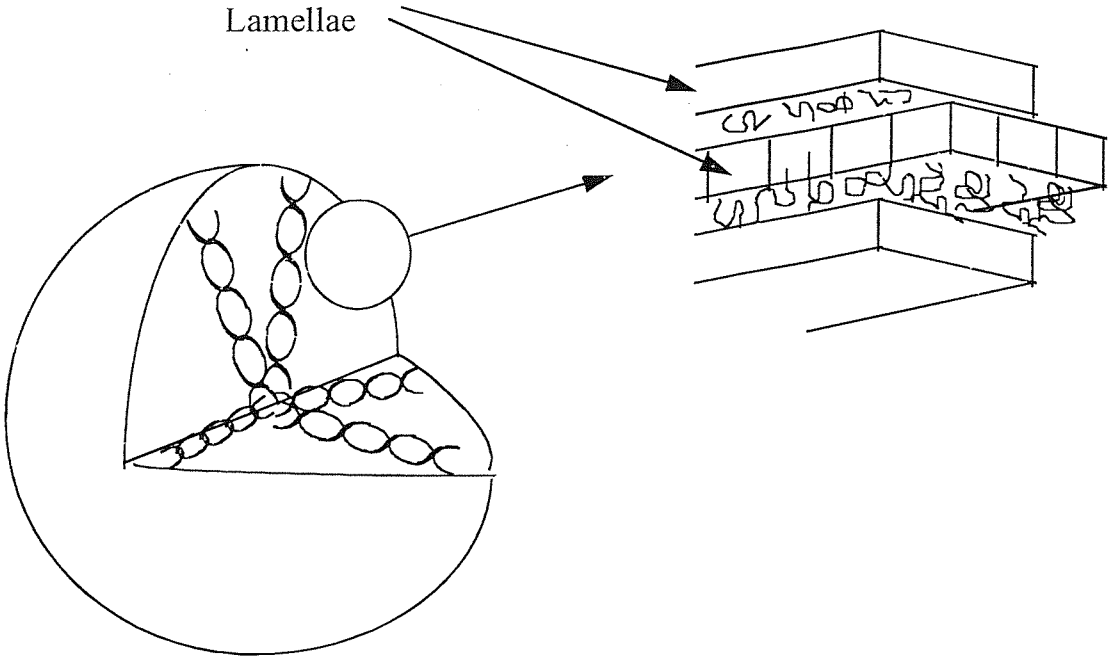

Figure 1.5: A schematic representation of the spherulitic structure

The crystallisation process of the melt occurs in two different stages[17]. Primary crystallisation occurs until the radial growth of the spherulites is completed and then secondary crystallisation happens when the remainder of the material crystallises. The latter stage involves the solidification of any impurities, the low molecular weight material and branched molecules in the inter-lamellae and inter-spherulitic regions. When two spherulites impinge during crystallisation, lamellae from both extend across the boundaries into any uncrystallised material available resulting in a higher strength to fracture of the interspherulitic regions[18].

The size of the lamellae inside the spherulites varies as a function of both molecular weight and crystallisation temperature. The lamellar size is almost always thinner than the average chain length, consequently it is assumed (as it is for single crystals) that molecular chain folding occurs at the lamellar interfaces. The most likely structure for melt crystallised polyethylene seemed to be that of single crystals, that is adjacent re-entry with regular folding, but the degree of entanglement and viscosity of the melt suggested that regular folding would be, perhaps at least to some extent, partially hindered. The complex nature of the melt has led to many views being put forward in order to determine the nature of the fold surface, which even now is not completely resolved.

1.2.3 The nature of the fold surface

As in the case for single crystals where the thickness of the lamellae is smaller than the average chain length, the same is seen with respect to melt crystallised polyethylene, and consequently correlations between these two forms were drawn.

The first model for crystallisation from the melt which gained widespread acceptance was proposed by Hoffmann and Lauritzen[19] when working on molecular models for polyethylene crystals. The model had adjacent re-entrant folding with regular fold periods and is illustrated in Figure 1.6. This was supported by Frank and Toshi[20] with the exception that the fold lengths were irregular as in Figure 1.7. Geil[21] accounted for the difference claiming that the regular folds were formed in slow crystallised samples and irregular folds were formed in quench cooled samples.

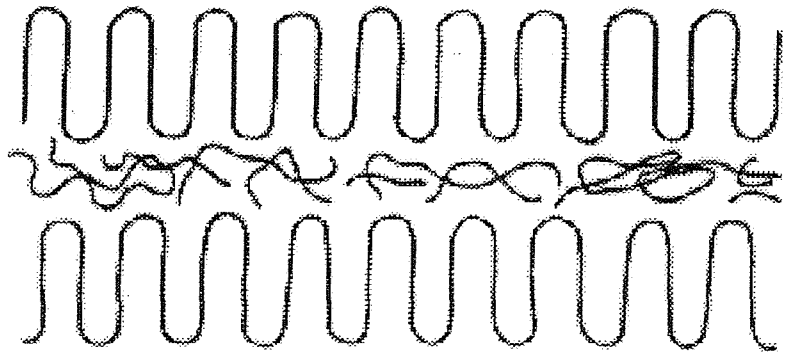

Figure 1.6: Adjacent re-entry model with regular folding for melt crystallised polyethylene

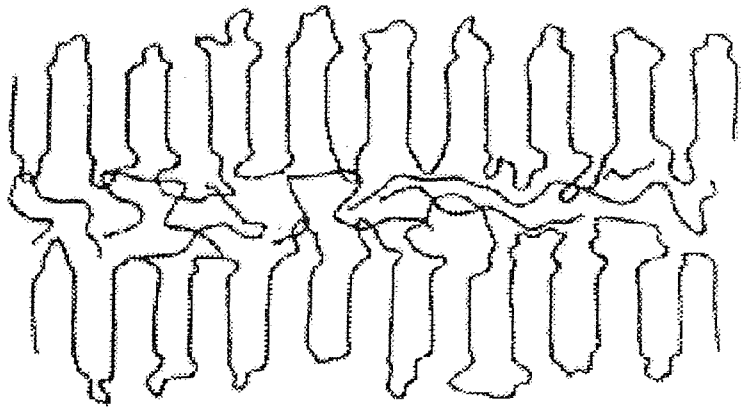

Figure 1.7: Adjacent re-entry model with irregular folding for melt crystallised polyethylene

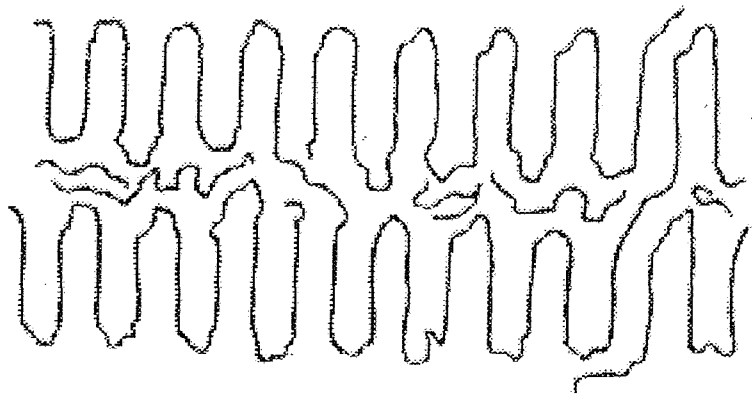

Figure 1.8: The function of tie molecules in the adjacent re-entry model for polyethylene

Adjacent re-entry soon became almost universally accepted as the mode by which crystallisation took place from the melt. However, physical and chemical properties indicated that a stronger bonding was present between lamellae. To account for this interlamellar strength, the concept of "tie molecules" between lamellae added to the regular adjacent re-entry model was introduced. Krigbaum's "tie chain" theory[22] proposed that tie molecules, unlike the rest, did not fold back immediately, but instead bridged the neighbouring lamellae by passing through the independent amorphous phase (uncrystalliseable material such as low molecular weight molecules, chain branches and impurities), as shown in Figure 1.8.

Mandelkern[10] did not believe in the concept of "tie molecules". He held the opinion that they were portions of a molecule, not straight or extended as it has been inferred in the past. Flory and Yoon[23] described the theory of "tie molecules" as a "clever invention".

In 1962 Flory[24] argued that from spatial requirements no more than half the chains leaving a crystalline region could be accommodated in the neighbouring amorphous region. To facilitate this the chains would need to reverse direction and re-enter the crystals, resulting in the formation of loops which would be situated in an interfacial zone located between the crystalline layer and the isotropic amorphous layer. It did not imply, however that these chains need be folded regularly as in single crystals. Many chains were considered to grow not only into and out of one lamella randomly via the amorphous and interfacial regions, they were also able to cross from one neighbouring lamella to another. This new model became known as the solidification model, represented in Figure 1.9. The model explained the high amorphous content, this being indicative of the molecules involved in the loops at the crystal surface, or those joining different lamellae. It also accounted for the mechanical strength of the polymer since there was a large number of chains bridging individual lamellae. In 1979, a major public discussion[25] on the organisation of macromolecules in the melt was published. The arguments supporting either the solidification model or adjacent re-entry model were based on two analyses, a theoretical analysis and an experimental one.

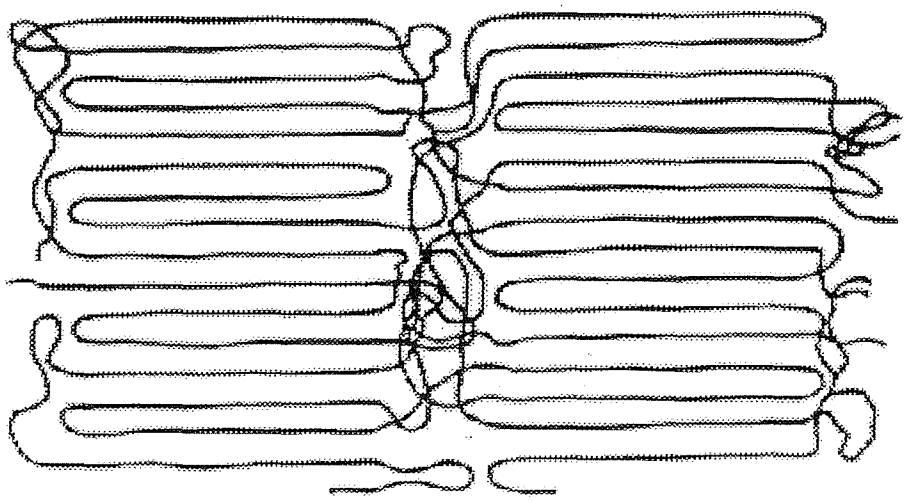

Figure 1.9: The Flory random re-entry (solidification) model for melt crystallised polyethylene.

Support for the adjacent re-entry model is based on the assumptions on the mobility of the chains in the melt phase. De Gennes reptation theory[26] overcame the handicap of chain mobility being restricted during crystallisation by devising a model where a chain is assumed to move with a worm-like motion through a tube imbedded in a matrix of entangled molecules as is shown in Figure 1.10.

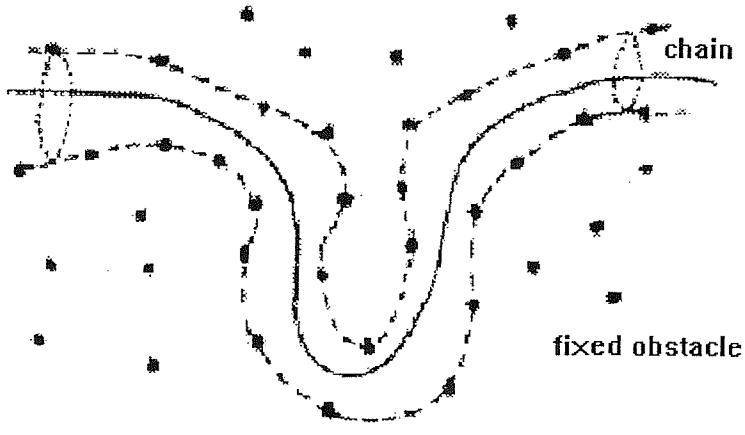

Figure 1.10: A chain trapped in a "tube" of surrounding polymer chains, (DeGennes reptation theory[26]).

The motion can be considered to be a "reeling in" of the slack along the length of the molecule, combined with some movement of the surrounding chains. This "suction" of the chains due to the crystallisation process would explain the achievement of adjacent re-entries. Flory and Yoon[23] claimed that a molecule relaxes and disentangles at a much slower rate compared to the crystallisation rate enveloping this same molecule.

In reference to the reptation model Hoffman[25] pointed out that because the kinetic theory of nucleation with chain folds has not yet been developed to account for "errors" such as interlamellar tie molecules or nucleation at two different sites of the molecule, the radius of gyration of melt crystallised material is overestimated, even though a significant fraction of the stems in the crystals exhibit adjacent re-entry

To corroborate this point it is important to mention that if nucleation occurs at many different points along the molecule, (there is no reason to think that it cannot occur) random re-entries will occur at the surface of the crystals.

Krimm and Jing's[27] infrared studies analysed the bending mode of CH_2 and CD_2 in melt crystallised mixed crystals and concluded that random re-entry folding predominates and that folding along the (2,0,0) planes is probably not significant contrary to earlier published work[28].

For neutron scattering experiments, mixtures of P.E.D and P.E.H must be quench crystallised to prevent isotopic segregation. The results indicate that the chains are located in approximately the same position after crystallisation as they did in the melt[29] which has also been put forward by Hendra *et al*[30]. Wignall *et al*[31] have suggested that since the mixtures are made with little or no time for segregation to occur, there must also be no time for reptation to occur either. Even Krimm has now conceded that almost 70% of the molecules present in the melt crystallised lamellae have a random re-entry conformation, the rest being folded adjacently over three or four chains[32].

Hendra *et al*[33] studied the crystallisation of polyethylene chains whose mobility had been artificially restricted by crosslinking. From their work they concluded that the chains crystallise by a mechanism of random re-entry. Thus, it seems that the solidification model is close to reality for polyethylene crystallised from the melt.

1.2.4 Extended chain crystals

Extended chain crystals may be grown from the melt when crystallised under very high pressure[34] (~ 5000 atm). Polyethylene crystallises into a completely extended chain conformation for molecular weight up to ~12000, above which chain folding is found. These extended chains exist in a metastable hexagonal conformation[35], the transition to orthorhombic phase occurs if the pressure and/or the temperature falls.

Extended chain crystallisation also occurs when polyethylene is crystallised from stirred solution[35], this subject will be discussed in greater detail in part 1.3.3.

1.3 Stress in semi-crystalline polymers

Generally speaking whenever high molecular orientation exists, arising either from crystallisation under stress, deformation of semi-crystalline polymers or natural oriented semi-crystalline polymers, there is an associated fibril-like morphology. It is particularly important to understand the mechanism of formation of these fibrils since it is commonly used to increase the mechanical strength of many polymers used in the textile industry.

The famed fringed-micelle model has been used extensively to elucidate the structural aspect of polymers. However, since 1957, this fibrous structure has had to be related to the then newly discovered lamellae.

The deformation process of single crystals is an appropriate and logical starting point, the investigation of which has served to unify the different theories.

1.3.1 Deformation of single crystals and Peterlin's model

An extensive examination of the deformation of single crystals adhering uniformly upon drying on a deformable membrane was carried out in the later 60's by a number of scientists, particularly by Peterlin[36].

He proposed a detailed model for the plastic deformation of single crystals of polyethylene and other semi-crystalline polymers as well as that of the melt crystallised ones. He made the assumption from a practical point of view, that spherulites are quite often composed of aggregates of chain folded crystal species.

This model based on wide and small angle X-ray diffraction data[37] and supported by electron microscopy[37,38], describes a three stage process for plastic deformation.

The first stage involves plastic deformation of the spherulite structure. It follows the elastic extension, where a slight b-axis orientation takes place (in polyethylene spherulites with the radial orientation of the b-axis), then it yields at very small strain to irreversible deformation and orientation of the c-axis in the draw direction with b and a axes in the plane perpendicular to it.

After twinning and phase transformation, which represent only a small plastic strain, a much larger extension can be achieved by chain tilting and slipping. Crack formation occurs between spherulites due to weaker boundary layers between spherulites, rather than the densely packed lamellae. It is possible to observe microfibrils bridging the cracks by electron microscopy.

The second stage consists in the fragmentation of the lamellae or the breaking off of blocks of folded chains, which are then incorporated in to the microfibrils. The spherulitic structure having been subjected to local preparation (sliding motion, rotation, chain tilt and chain slip) during the first stage is transformed to a fibrous one by this process.

The final stage is in fact closely related to the second since it may well begin before the second stage is completed. This comprises of the plastic deformation of the fibrous structure, when the bundles of microfibrils can slide past each other. These microfibrils are linked by tie molecules which can represent as many as 30% of the chains in polyethylene with a high draw ratio[36]. The fibrous structure would explain the anisotropy in mechanical properties as well as the strain hardening.

Figure 1.11 illustrates the model for plastic deformation of single crystals proposed by Peterlin[39], which was then extended to bulk samples[36] on the basis of the regular adjacent re-entry model for melt crystallised polymers.

The deformation of bulk polymers will likely be highly dependent on the morphology of the interlamellae connections before drawing.

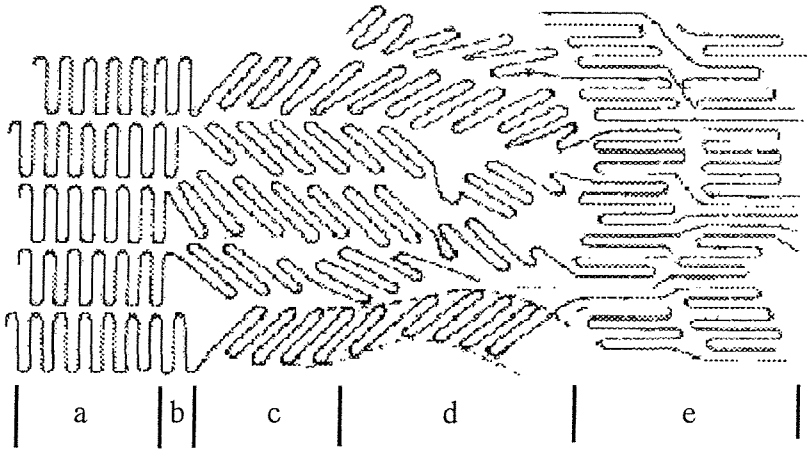

Figure 1.11: The suggested model for plastic deformation by chain tilting, slipping and breaking off of blocks of folded chains (Peterlin's model). a) represents the undeformed crystals; b) phase change and twinning; c) tilting, slipping and twisting; d) cracks forming, more tilting, slipping and twisting and e) fibril formation

1.3.2 Deformation of melt crystallised polymers

Deformation of a film of polymer involves the deformation of the spherulites, those of the crystallites which will result in the orientation of the crystalline (lamellae) and the amorphous substructure. Scattering techniques provide the best methods[40] for analysing the deformation of spherulites, but as Samuels[40] pointed out, the sample preparation is the major problem if one wishes to apply these techniques.

Spherulite deformation leads to the fibrous structure mentioned in 1.3.1. One could easily assume that the three stage scheme described also applies to the deformation of spherulites, however the process is much more complex than for the single crystal. The extent of unzipping of the chains is not clearly understood due to the uncertainty surrounding the nature of the inter-lamella connections.

There are two main features which can be observed during the process:
Firstly, the spherulite shape changes finitely with the overall shape of the sample[40], however, at ambient temperature, in polyethylene the spherulite strain amounts to less than 1%[41]. Secondly, there is a separation at the boundaries and destruction of the spherulites, a process associated with necking[41].

Samuels[40] has shown that the deformation and structural changes are largely controlled by the non-crystalline molecules and that different behaviours take place in lamellae lying at different angles to the draw direction as can be seen from Figure 1.12.

A simple schematic representation of the overall structural changes which occur during spherulitic deformation is illustrated as a stress-strain curve in Figure 1.13.

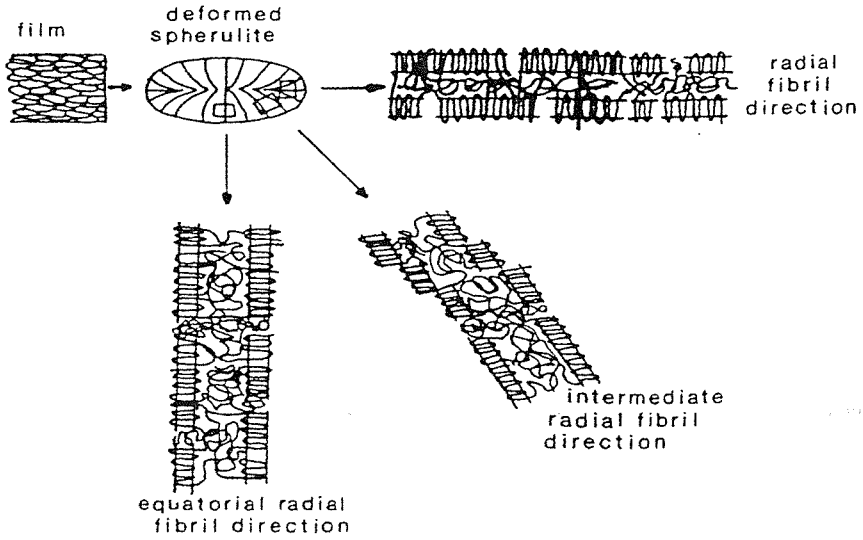

Figure 1.12: Schematic representation of the deformation process at the lamellae level (assuming adjacent re-entries[40]).

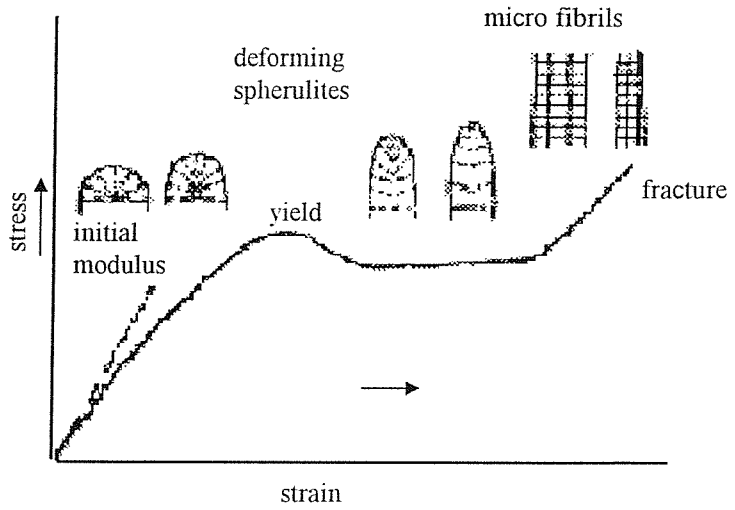

Figure 1.13: Schematic representation of the structural changes in different regions of the stress-train cure.

As was discussed previously in part 1.2.3, it is difficult to assess the changes which take place at the molecular level if it is assumed that the fold surface of the crystallites is better represented by random re-entries and entangled molecules connecting the lamellae.

The exact incidence of local melting and re-crystallisation prior to fibrillar extension is not yet fully understood, although it is becoming more and more apparent when rapidly crystallised samples are deformed. Taylor's work[42] however, showed that melting was an essential step in the plastic deformation process when moderately high draw rates and environmental temperatures were involved. This result contrasted with both Peterlin's and Samuels' models.

1.3.3 Deformation of molecules in solution

When polyethylene is crystallised from stirred solution, crystals develop on the rear of the stirrer blades with a different morphology than those which form unperturbed solutions. The crystals have a fibrilar striated appearance with a high modulus and small elongation to fracture. Electron microscopy reveals a structure composed of lamellae strung together at intervals of ~100 nm[43]. Electron diffraction studies indicate molecules being orientated mainly along the fibril axes. The distinctive shape of these crystal entities has earned them the name of "shish-kebabs".

The crystal core is thought to be composed of partially extended crystal material[44], but not of fully extended molecules. The kebabs form by epitaxial growth using the central shish as a nucleus. Kebab overgrowth can be removed by successive washing of the material with hot solvents. Figure 1.14 gives a schematical representation of the shish-kebab structure.

Since longitudinal velocity gradients in solution extend chains and result in shish-kebab formation, the question is raised as to whether the same structures can be formed in shearing melts. Several workers have studied melts under shear[45,46] and it appears

that they can indeed crystallise in a similar form to stirred solutions, producing extended chain backbone crystals which nucleate radial by chain folded lamellar growth.

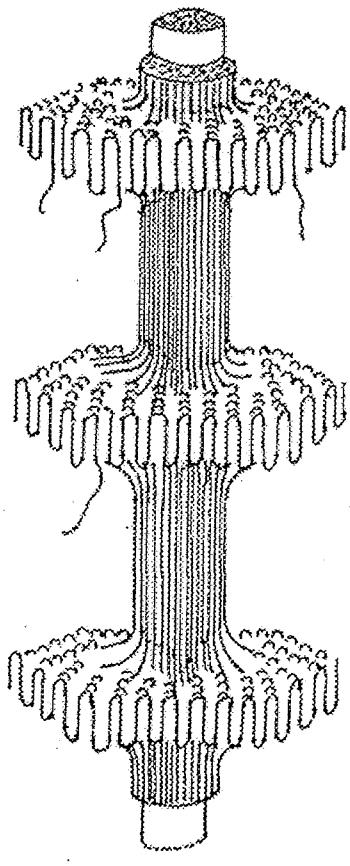

Figure 1.14: The formation of a shish-kebab crystal.

1.4 Stress in Melts

An extensive amount of work has been carried out on the crystallisation of polymer melts, as has been discussed.

The process of Stress or Strain Induced Crystallisation (S.I.C.) is an extremely importance step in the production of polymer fibres and films. The definitive structure of polymers crystallised by either S.I.C. and/or Temperature Induced Crystallisation (T.I.C.) will be discussed later in the section but firstly we must examine the structure of the static polymer melt prior to crystallisation.

1.4.1 The structure of the static polymer melt

The "random coil model" presented in Figure 1.15 was the first well supported theoretical concept to describe the melt or the amorphous state, and assumed that the melt consisted of an orderless mass of coiled molecules. However, the experimental value of the melt density is higher then the theoretical one predicted by the random coil model. Robertson[47] suggested that the chains have a tendency to form nodule-like structures containing parallel chains. This result provoked the proposal of several new models for the structure of the melt state.

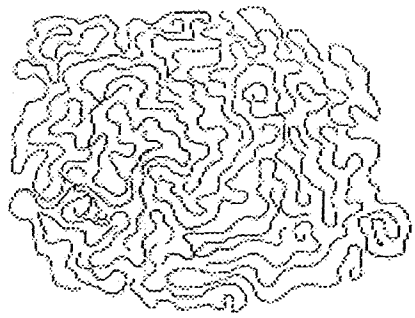

Figure 1.15: Schematic random-coil model.

Yeh[48] reported the presence of ordered regions of sizes up to 100Å from electron microscopy and electron diffraction studies, which led to the folded-chain fringed micellar model (Figure 1.16).

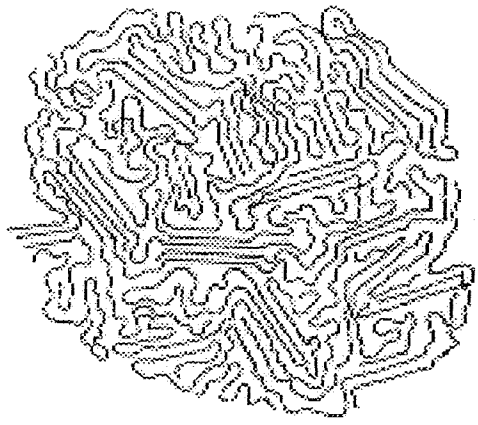

Figure 1.16: Representation of the folded-chain fringed micellar grain.

The Pechhold model[49] (Figure 1.17) has bundles of polymer molecules consisting of folded chains with a net orientation in the direction of the long axis of the bundle. These bundles then superfold upon themselves to produce, what appears on a macroscopic scale to be, an isotropically oriented material.

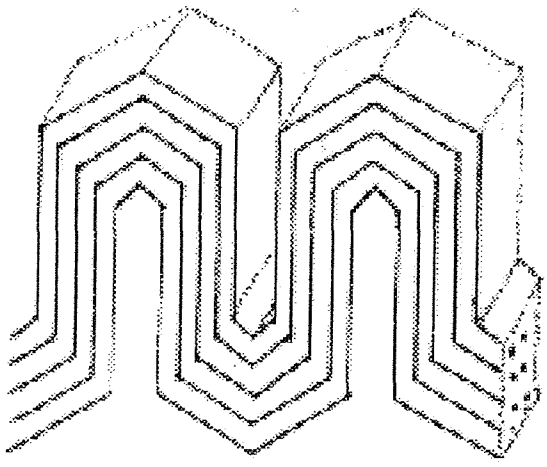

Figure 1.17: The bundle model for the amorphous structure of polymers.

Voigt-Martin and Mijlhoff[50] electron diffraction data claimed that the peak Yeh had proposed as being indicative of molecular ordering, appearing between 4 and 6Å, was absent when suitable correction for the background had been made. Uhlman's [51] investigations on glassy polymers concluded that there was no evidence for any structures larger than 5Å, noting that if the instrument was badly focused then a nodular appearance resulted.

It is more difficult however, to disprove Bundle type models. They occur from a tendency of the chains to align parallel to each other, but only for chains of a limited flexibility would such order be preferred. One such example is Polytetrafluoroethylene, PTFE, which does possess chains with of high stiffness, and has been known to exhibit partial ordering[52].

To date the situation on the order and the structure of molten and amorphous polymers is not clear. However, the majority of neutron, electron and X-ray diffraction evidence indicates no detectable order in the bulk amorphous polymers composed of flexible chains, thus supporting Flory's random coil model. There is still of course, the major concern with the anomalously high observed density in the amorphous state. Models involving partial ordering have been proposed, but with insufficient experimental evidence to support them, and so no single model appears to adequately account for all the observed physical properties.

1.4.2 Strain Induced Crystallisation

Strain Induced Crystallisation (S.I.C.) is mainly associated with the process of melt spinning for the production of polymer filaments. The molecular orientation of a filament increases with spinline tension, the difference between the take-up and extrusion velocities, and the inverse of filament diameter[53].

Chains which are extended prior to crystallisation can form long fibrous crystals where the chain axis is parallel to the filament axis. The state of the material represents a pinnacle of achievement in terms of physical properties, where the strength along the filament axis is only limited by the covalent bond strength of the constituent atoms. The maximum theoretical strength and tensile of polyethylene is certainly comparable to the best steels, and because of the low density of polymeric materials in general, the specific strength and moduli are potentially among the highest of all known materials[44].

A study was made by Hill and Keller[54] of crystallisation under stress which showed the initial appearance of a well ordered fibrous crystal, where the c-axis lies parallel to the applied stress, crystallised isothermally at ~132°C. The X-ray diffraction patterns showed sharp reflections, indicating a high degree of crystal order. The crystals melted on the removal of stress and then re-appeared as the stress was re-applied, taking 30-60 mins. at 135°C.

These were called type I crystals and were found to be of high thermal stability. Type II crystals were formed after the appearance of type I, and their degree of alignment was shown to be a function of the applied stress.

A row-nucleated structure was proposed as is represented in Figure 1.18. Type II crystals were not observed above 133°C, and so the type I crystals at 135°C were shown to be the nucleating material.

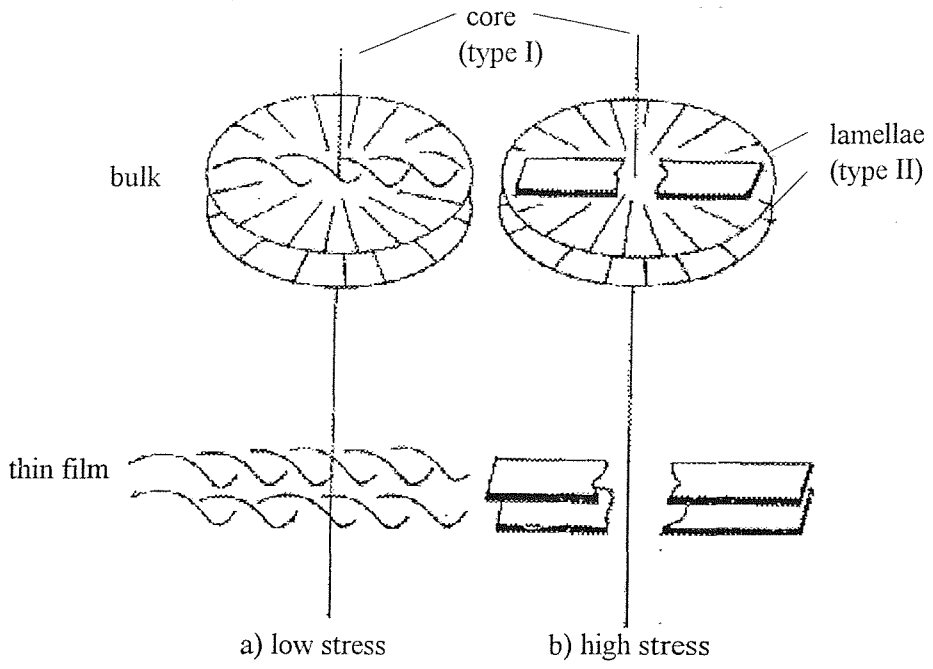

Figure 1.18: Schematic diagram illustrating row-nucleated structure of polyethylene crystallised under a) low stress and b) high stress

At low stress, the c-axis is parallel and the b-axis is perpendicular to the applied stress. The a-axis can vary randomly and the lamellae (type II) are thought to twist as in spherulite formation from quiescent melts. The twisting allows the type II crystals to be distinguished from the type I by X-ray diffraction.

1.5 The Young's modulus of drawn fibres

The tensile modulus, E (sometimes called the Young's modulus) can be derived from the initial reversible slope of a plot of applied stress against strain, where the response of the specimen is purely elastic, see Figure 1.13 (represented as the initial modulus).

All plastic products are made up of long chain molecules which, by definition, are covalently bonded. In theory if the molecular chains in an article could all be aligned the material would have exceptionally high stiffness and strength in the chain direction[44] since the stress would be opposed by the covalent bonds themselves. The existence of polymer lamellae, especially chain folded lamellae, gives qualitative evidence of why the Young's modulus of macroscopic samples (e.g. fibres) is typically 3-4 orders of magnitude less than values for the crystal lattice; the reason being that the measured values relate primarily to the low modulus disordered material. If the modulus of the crystalline lattice could be approached, in practise it would bring a new range of potential applications to polymers with stiffnesses comparable to the best steels (210 GPa).

1.6 References

1. F. Rodriguez; "Principles of Polymer Systems", 2nd ed., International Student Edition (1983).
2. H.Staudinger, Ber. 53, (1920) 1073.
3. W.T.Astbury, "Fundamentals of Fibre Structure", Oxford University Press (1993).
4. F.Khoury and E.Passaglia in "Treatise on Solid State Chemistry", vol. 3, Chap. 6, Plenum Press, New York-London (1976).
5. C.W.Bunn; Trans. Faraday Soc., 35, (1939) 482.
6. D.I.Bowers and W.F.Maddams, "The Vibrational Spectroscopy of Polymers" Cambridge university Press (1989).
7. A.Keller; Phil. Mag., 21, (1957) 1171.
8. P.H.Till; Jour. Poly. Sci., 24, (1957) 301.
9. A.Keller and A.O'Connor; Disc. Faraday Soc., 25, (1958) 114.
10. L.Mandelkern; Jour. Poly. Sci., Poly. Sympo., 50, (1975) 457.
11. A.Keller; Rep. Progr. Phys., 31, (1968) 623.
12. R.P.Palmer and A.J.Cobbold; Makromol. Chem., 74, (1964) 174.
13. H.S.Kaufman and J.J.Falcetta; "Introduction to polymer science and technology", J.Wiley and Sons, New-York (1977).
14. D.C.Bassett, A.Keller and S.Mitsuhashi; Jour. Poly. Sci., A1, (1963) 762.
15. P.H.Geil; "Growth of perfect crystals", Edited by R.H.Doremus, B.W.Roberts and D.W.Turnball, J.Wiley and Sons, New-York 579 (1958).
16. Y.Fujiwara; Jour. Appl. Poly. Sci., 4, (1960) 10.
17. J.Rohleder and H.A.Stuart; Mackromol. Chem., 41, (1960) 110.
18. F.W.Billmeyer; "Textbook of polymer science", J.Wiley and Sons (1984).
19. J.D.Hoffmann and J.I.Lauritzen; Jour. Chem. Phys., 31, (1957) 1680.
20. F.C.Frank and M.Tosi; Proc. Roy. Soc. Lon., A, 263, (1961) 323.
21. P.H.Geil; Chem. Eng. News, 43, (1965) 72.
22. W.R.Krigbaum; Jour. Poly. Sci., part C, 15, (1966) 251.
23. P.J.Flory and D.Y.Yoon; Nature, 272, (1978) 226.

24. P.J.Flory; Jour. Am. Chem. Soc., 84, (1962) 2857.
25. Discussion of Faraday Division of the Chemical Society, 68 (1979).
26. M.Daoud and P.G.DeGennes; Jour. Poly. Sci., Poly. Phys. Ed., 17, (1979) 1971.
27. X.Jing and S.Krimm; Jour. Poly. Sci., Poly. Lett. Ed., 21, (1983) 123.
28. M.I.Bank and S.Krimm; Jour. Poly. Sci., A2, 7, (1969) 1785.
29. J.Schelten, D.G.Ballard, G.D.Wignall, G.Longman and W.Schmatz; Polymer, 17, (1976) 751.
30. D.Aitken, D.J.Cutler, M.Glotin, P.J.Hendra, M.E.A.Cudby and H.A.Willis; Polymer, 20, (1979) 1465.
31. G.D.Wignall, L.Mandelkern, C.Edwards and M.Glotin; Jour. Poly. Sci. Poly. Phys. Ed., 20, (1982) 245.
32. X.Jing and S.Krimm; Jour. Poly. Sci. Poly. Lett. Ed., 21, (1983) 123.
33. P.J.Hendra, A.J.Peacock and H.A.Willis; Polymer, 28, (1987) 705.
34. P.H.Geil, F.R.Anderson, B.Wunderlich and T.Arakawa; Jour. Poly. Sci., part A2, (1964) 3707.
35. R.B.Brime and B.Wunderlich; Jour. Poly. Sci., part A2, 7, (1969) 2061.
36. A.Peterlin; Jour. Poly. Sci., part C, 15, (1966) 427.
37. A.Peterlin; Coll. Poly. Sci., 253, No.1 (1975).
38. A.Peterlin; Poly.Eng. Sci., 9, No.3 (1969).
39. A.Peterlin; Jour. Poly. Sci., part C, 9, (1965) 61.
40. R.J.Samuels; "Structures polymer properties", J.Wiley and Sons, New York (1974).
41. "Encyclopaedia of polymer science and technology", 9, J.Wiley and Sons, 262, (1968).
42. M.A. Taylor, Ph.D. Thesis, University of Southampton (1984).
43. A.J.Pennings and A.M.Kiel; Kolloid ZZ Poly., 205, (1965) 160.
44. A.Keller and P.J.Barham; Plast. Rub. Int., 6, (1981) 19.
45. A.Keller and M.J.Machin; Jour. macro. Sci., Phys-B, 1, (1967) 41.
46. M.R.Mackley, F.C.Frank and A.Keller; Jour. Mat. Sci., 10, (1975) 1501.
47. R.E.Robertson; Jour Phys. Chem., 69, (1965) 1575.
48. G.S.Y.Yeh; Jour. Macro. Sci., Phys-B, 6, (1972) 465.
49. W.R.Pechhold and H.P.Grossmann; Faraday Disc. Chem. Soc., 68, (1979) 58.

50. I.Voigt-Martin and F.C.Mijlhoff; Jour. Appl. Phys., 46 (1975) 1165.

51. D.R.Uhlmann; Faraday Disc. Chem. Soc., 68, (1979) 87.

52. R.Lovell, G.R.Mitchell and A.H.Windle; Faraday Disc. Chem. Soc., 68, (1979) 46.

53. J.E.Spruiell and J.L.White; Plast. Eng. Tech. paper, 21, (1969) 153.

54. M.J.Hill and A.J.Keller; Macromol. Sci. Phys. B3, 153 (1969).

2. Chapter Two: Novel methods for the production of high performance polymer fibres.

High performance polymer fibres have the best specific mechanical properties of any structural material – the specific stiffness and strength being the actual strength and stiffness divided by density[1]. Aramid polymer fibres such as Kevlar (Du Pont) and Twaron (Akzo Nobel) possess Young's moduli of more than 100 GPa and strengths of 3 GPa but densities of only 1500 kgm^{-3} thus offering specific mechanical properties comparable and sometimes exceeding those of metals.

There is an increasing demand for high performance polyethylene (HPPE) fibres, with applications that are complementary to those of Kevlar and carbon fibres. HPPE fibres are finding widespread use in applications such as protective clothing, body armour, high-performance ropes, as well as being used as reinforcement in advanced composites. The high tensile modulus and strength of HPPE is realised through the high degree of molecular orientation of the flexible linear molecules along the fibre axis since the load is then supported by the covalent bonds themselves[1]. Currently there are three well-established methods used to produce HPPE fibre, namely: (1) Cappaccio & Ward's ultra-drawing method[2]; (2) Zwijnenburg & Pennings' dilute solution method[3] and (3) Smith & Lemstra's gel spinning procedure[4].

2.1 Developments in Polyethylene Fibre Production:

In recent times, developments of high modulus and high strength polyethylenes has been carried out in several different, but related, activities. In the 1960's attempts were made to produce high modulus fibres either by deformation in the solid phase (tensile drawing) or by solution processing. In 1973, Cappaccio and Ward[2] demonstrated how, by hot stretching of samples to very high draw ratio (typically > 30), oriented polyethylene with a tensile modulus of 70 GPa and tensile strength of nearly 1 GPa could be achieved. Only moderately high molecular weight (Mw < 500,00) of PE could be used in this process due to the viscosity restriction during melt-spinning.

Then in 1976, Zwijnenburg and Pennings[3] showed that very fine filaments of very highly oriented polyethylene could be pulled from dilute solutions at high temperatures. This work achieved tensile moduli as high as 100 GPa and tensile strengths of 2.5 GPa. Smith and Lemstra[4] progressed, showing how gel spun fibres produced by precipitating a moderately dilute solution of polyethylene into a nonsolvent could be hot-drawn to give fibres with properties comparable to those by Pennings *et al* from the very dilute solutions. This process method is straightforward and leads itself to commercial production (DSM in The Netherlands) of HPPE fibres.

The properties of PE fibres obtained by melt-spinning and ultra-drawing are relatively low compared with those of the gel-spun PE fibres but the attraction of melt-spinning is its simplicity, relative low production cost and it is environmentally friendly[5]. Progress in developing major applications has been however comparatively slow. Research at the University of Leeds and Amsterdam[5,6,7] have produced oriented materials, however, the methods of production have been slow and not attractive for general industrial purposes.

In parallel with these developments in polyethylene fibres, there have been important developments in the areas of solid phase deformation by ram extrusion[8], hydrostatic extrusion[9] and also die drawing and roller drawing[10]. This work has demonstrated the ability to control the crystallinity and orientation in polymer fibres achieving high performance materials from commodity polymers.

Several years ago, researchers here at Southampton became interested in the quest for a glass of polyethylene. Such a material was produced by quench cooling the melt and then retaining it at a temperature below –110 °C. As part of the programme (and it was doomed to failure because temperatures were well in excess of Tg) preliminary experiments were carried out using low temperature molten metal baths as heat sinks (the idea being to achieve hitherto unprecedented cooling rates). A process was devised whereby a thread of polymer was pulled continuously from a die at the bottom of a shallow tank of molten metal. Fine filaments (~ 150μm) were drawn at rates close to 5 ms^{-1} through metal baths at temperatures of 120 °C. The rapid cooling process

produced materials which were found to be up to 80% crystalline by X-ray diffraction. The fibres were also found to be very highly oriented. The lamellar thickness derived from the Raman LA mode were around 180 Å and polarised Raman measurements showed that the z-axes of the lamellae were almost perfectly parallel to the draw direction. The fibres also showed enhanced mechanical properties compared with those allowed to cool through air[11,12].

The process demonstrated the viability of polymer processing through molten metal baths and its ability to affect crystallisation kinetics. It was necessary however to explore the overall scope and limitations of this new processing technology as a route to fibres with enhanced mechanical properties. Melt spinning through the molten metal bath followed by effective cold drawing was proposed as a method to produce PE fibres with mechanical properties comparable to those obtained by Ward *et al.* Molten metal bath processing offered the potential advantage of producing fibres at a faster rate compared with other methods of production and of being straightforward and highly cost-effective.

2.2 The Processing of Polymer Melts

Polymer processing typically involves flowing the polymer melt through a die or into a mould, followed by rapid solidification; this frequently involves crystallisation. The cooling process can determine some of the polymer properties. For instance, the combined effects of shear and extension during the cooling stage can induce a degree of orientation of the polymer. Crystallisation kinetics in flowing melts is of central importance in the processing of high performance materials. However, the main difficulty in studying such kinetics is the need to achieve a high degree of control over the processing conditions. In particular the rates of extrusion, extension and heat transfer are thought to directly determine the mechanical properties of the final material. Moreover, the conditions must be highly reproducible and achieved at a commercially realistic rate. A polymer processing system was thus designed to allow the required degree of control over these processing variables together with the high degree of reproducibility.

The use of a molten metal bath as a heat transfer medium has several features which makes it advantageous for investigating and controlling crystallisation kinetics. The bath temperature can be set to cover a wide range of temperatures (40 °C to >300 °C) through a choice of low melting point alloys (e.g. proprietary mixtures based on antimony). This allows the flowing polymer melt to be subjected to a variety of quenching rates, and hence to relate crystallisation processes to depth of quench. Metals combine a low heat capacity and high thermal conductivity making the heat transfer capacity per unit area 3 times more effective than air. The flowing polymer can be then subjected to a variety of cooling rates which can hence be related to the crystallisation rates. The combination of flow and heat transfer properties can achieve temperature gradients along the polymer as it emerges from the die. The metal has a restraining effect on the flowing polymer and affects the drag coefficient at the polymer interface on being drawn. A 'fountain' of molten metal surrounds the fibre as it emerges from the bath.

2.2 Fibre Spinning Rig

This section gives a description of the melt spinning rig, purpose built at Southampton and employed in this study. Figure 2.1 shows the apparatus which was used for the process. The rig is comprised of four distinct parts; a general purpose extruder (Baughn 1.25" commercial extruder), a die (1 mm diameter) allowing extruded polymer to enter directly into a molten metal reservoir (low melting point metal alloy) held at a temperature just below the melting point of the polymer. Fibre can then be wound onto a bobbin and stored; the speed of the spin line allows variable take up velocity of the polymer fibres which determines the extension and hence the diameter of the polymer monofilament produced.

A Hydraulic Drive
B. Hopper
C. Extruder Barrel
D. Extruder Flange
E. Reducing Flange
F. Die Block
G. Molten Metal Bath
H. Fume Hood
I. Wind-Off System

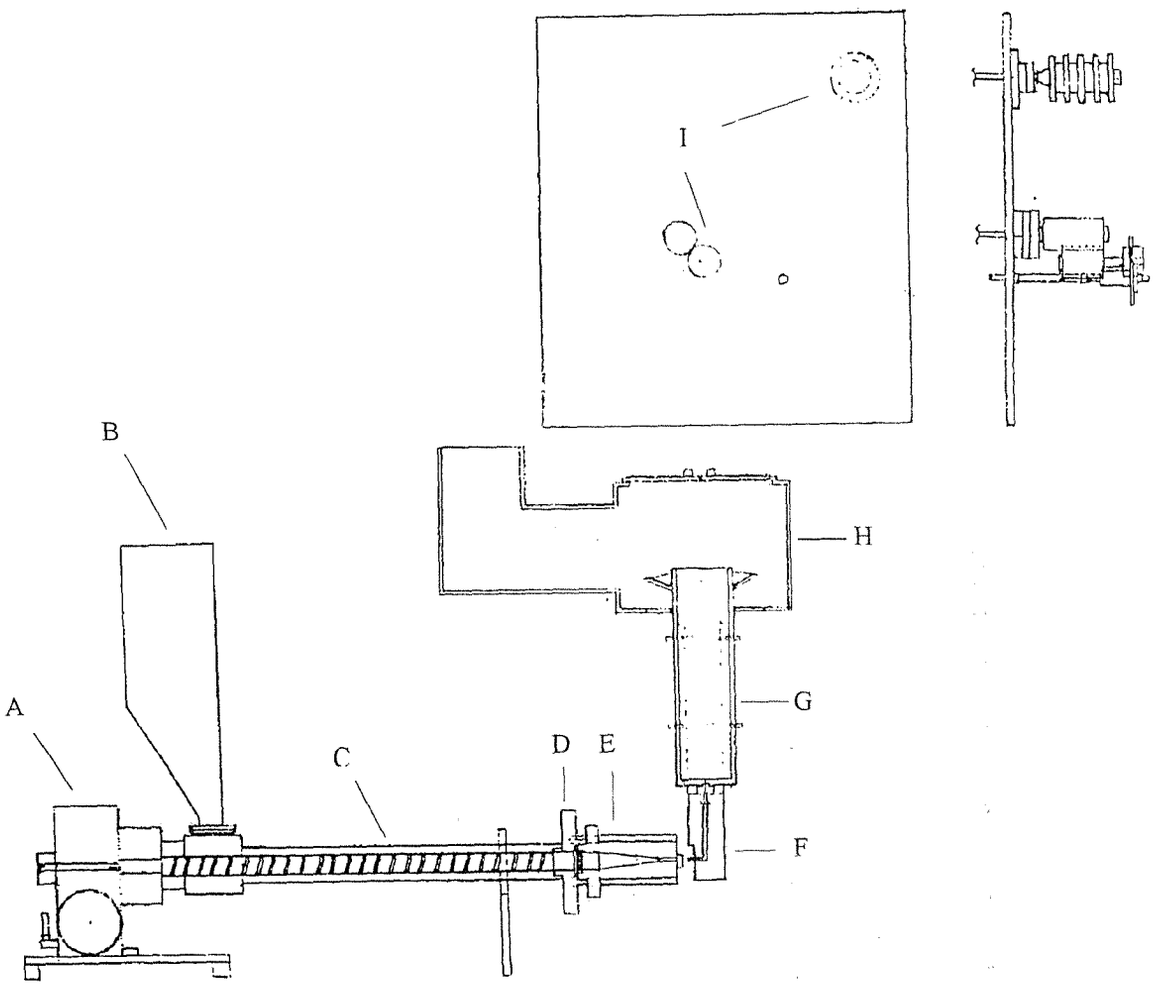

Figure 2.1: Schematic illustration of the fibre spinning rig

2.2.1 The Extruder

The extruder is the primary processing machine used in the polymer industry. Figure 2.2 illustrates its main features. It consists of a long Archimedian screw operating in a heated barrel. A hopper feeds the polymer into the water cooled feed zone, into the extruder barrel where it is then pushed towards the die by the screw; the design involves gradually decreasing clearance between the screw and the barrel walls and the consequent reduction in volume forces the polymer particles together.

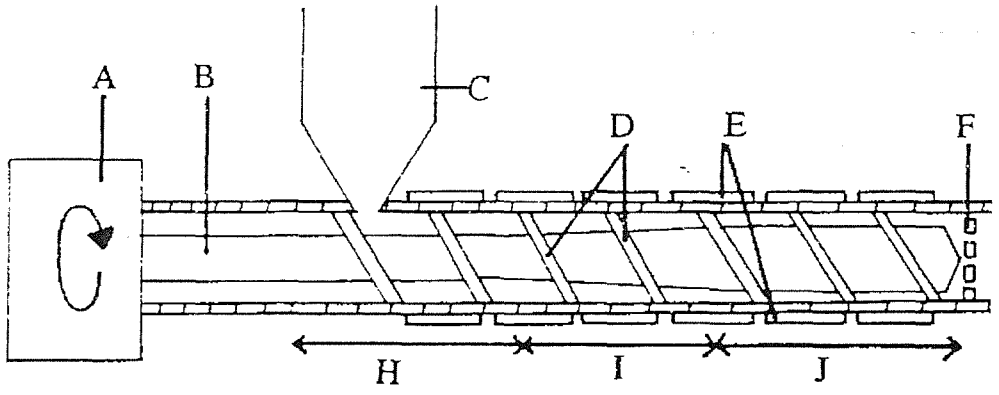

A. Motor B. Screw C. Hopper D. Screw flights E. Heater
F. Breaker plates H. Feed Zone I. Compression Zone J. Meter Zone

Figure 2.2: Schematic cross section through an extruder

The purpose of extrusion is three fold; it melts the polymer by contact with the barrel and combined with the action of the screw, homogenises and compresses the material. The screw (length to diameter ratio of 20:1) is driven at a constant speed by means of a motor and a continuously variable hydraulic drive. The maintenance of constant screw speed is important in producing a constant stability of output whilst allowing the fibre to be significantly drawn down by the melt spinning process. Heating units and chromel-alumel thermocouples maintain the extruder barrel at an operator-selected temperature sufficient enough to melt the polymer and reduce its viscosity.

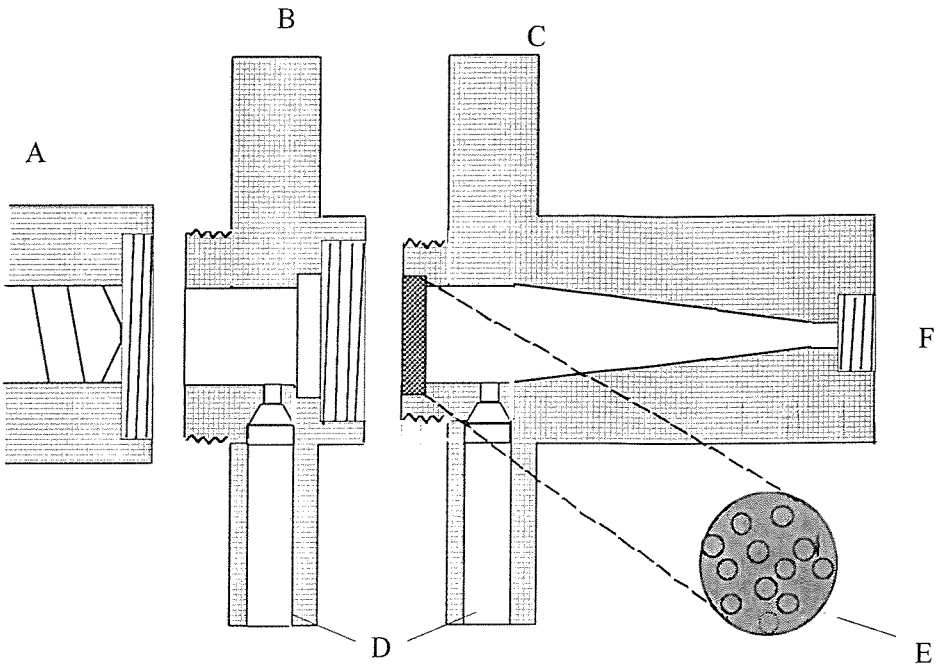

A. Extruder B. Extruder Flange C. Reducing Flange D. Pressure transducer
E. Breaker Plate and filter pack F. Fitting for die block

Figure 2.3: Components of the spinning rig

2.2.2 The Flange and Die Block Assembly

The resultant melt is then forced through the stainless steel extruder flange containing a breaker plate and a wire mesh filter pack which are used to provide a constant back pressure and also provide homogenisation. These components are illustrated in Figure 2.3. The melt pressure inside the extruder flange was monitored using a Dynisco pressure transducer with a digital read-out facility (p.s.i. units). A reducing flange then allows the melt to flow easily into the die block (6 mm internal diameter tube) which turns the melt through 90 ° upwards into the die. Each component is heated separately allowing control over the temperature gradient of the entire processing rig. The detachable die is covered with an insulating seal (as in Figure 2.4 below) to minimise heat transfer into the molten metal bath and to prevent molten metal from leaking. The seal design allows the polymer to flow straight into the molten metal bath and allows the fibre to be pulled directly from the tip of the die.

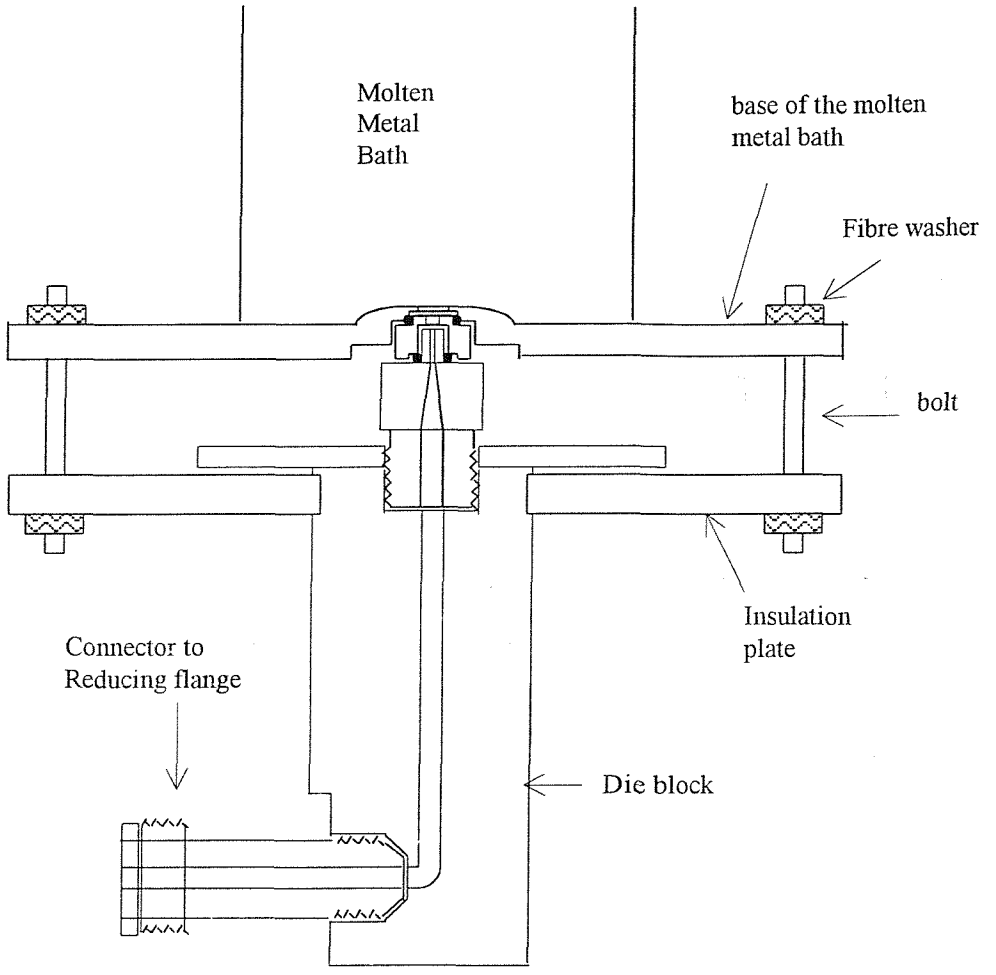

Figure 2.4: Schematic of die block and die/seal/molten metal bath assembly

The only metal to metal contact from the die to the bath in the final assembly was where the tip of the die allowed the passage of polymer directly into the liquid metal bath. In this way, the temperature of the bath and die could be controlled independently over the temperature range required for experiments.

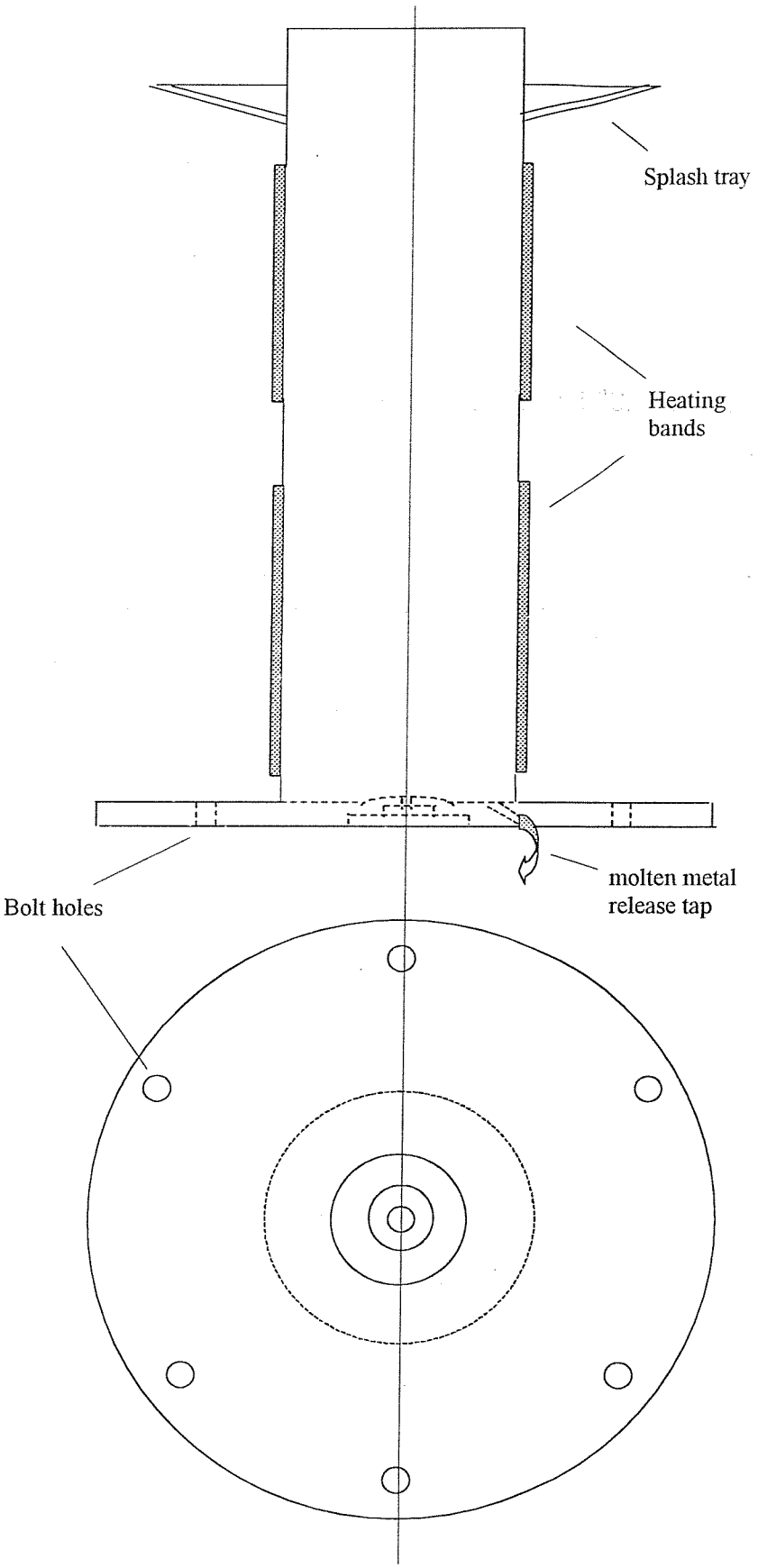

Figure 2.5: Schematic of the molten metal bath

2.2.3 The Molten Metal Bath

A mild steel cylinder was welded to a circular steel plate to act as a container for the molten metal. A stainless steel valve was fitted to the cylinder base to allow the molten metal to be drained off when required. The metal used, supplied by Hostalloys, was an alloy of bismuth, tin and lead, with a melting point of 97 °C. Two large band heaters surrounded the reservoir and were powered by heating units that maintain control of the bath temperature to within 1 °C. A stirrer was also fitted in the molten metal bath to ensure an even temperature throughout the liquid metal (a temperature difference between the top and bottom was as high as ~15 °C without the stirrer). The splash tray prevented molten metal from spattering out from the bath. To safeguard against any fumes given off from the molten metal bath an extractor was fitted which was linked from the bath to the fume hood by means of a sealed hose.

The whole assembly was bolted together through six holes in the bath base plate and an insulation plate fitted to the die block. Fibre washers were used under the bolt heads acting as thermal insulation of the bath from the bolts. The holes in the insulation plate and the metal bath base plate were drilled to allow clearance of the bolts, again improving insulation of the heat sink from the die.

2.2.4 The Spin line and Wind-off facility

Figure 2.6 shows a front elevation and side view of the wind off facility. The main support board was made of 15 mm thick plywood. The filament was wound over two rollers and then wound onto a collection bobbin. Two thyristor controllers powered two type 764 Parvalux electric motors and provided an infinitely adjustable speed such that a constant tension was maintained in the fibre. The free running roller was allowed to pivot on an arm which offered an appropriate resistance to movement and maintained fibre tension. The speed of the take-up bobbin (spinning speed) was monitored by a simple mechanical tachometer.

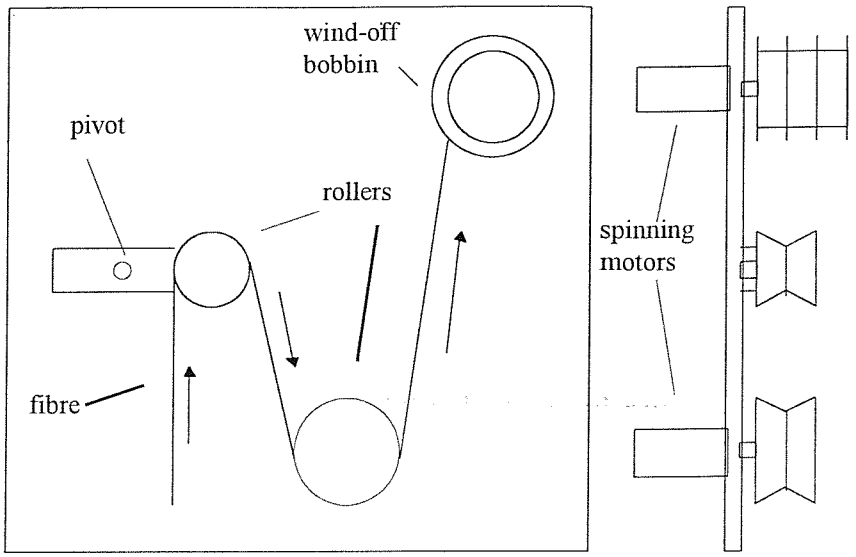

Figure 2.6: The spin line

2.4 Mechanical Testing

Mechanical testing of the fibres was performed using a tensile testing apparatus devised to fit on a Myford Super 7 mechanical lathe. The fibre sample was held between two clamps; one clamp was bolted to the bed at the tail stock end and the other attached to a load cell, which was bolted to the tool post with the thread cutting facility providing a range of crosshead speeds. The fine diameter of the specimens produced in this study was in itself a problem. To remove the possibility that the sample might be damaged during testing, the ends of the fibre were wrapped with a soft tape to protect the fibre ends from being compressed by the clamps and to prevent the fibre sample from slipping during testing.

The output from the load cell was fed to a strain gauge amplifier (see figure 2.7) which produced a voltage signal which was plotted on chart recorder. Calibration of the load cell and the chart recorder was achieved by the use of standard weights. The Young's modulus was derived from the initial slope of the stress-strain curve knowing the diameter of the fibre. The tensile strength and extension at break was calculated for the fibres.

When the applied stress causes strain in excess of the elastic limit, plastic flow follows and the sample yields. Plastic flow is accompanied by necking of the material, where the cross section of the material suffers a highly localised reduction. The orientation introduced into the material beyond this point raises the modulus above that of the unyielded material such that the neck is seen to transverse the sample length with ever increasing strain. The sample length was 30 mm and the crosshead speed was 5 mm/min. In order to accurately measure the initial slope of the stress-strain curve the paper speed of the chart recorder was set to 150 mm / min.

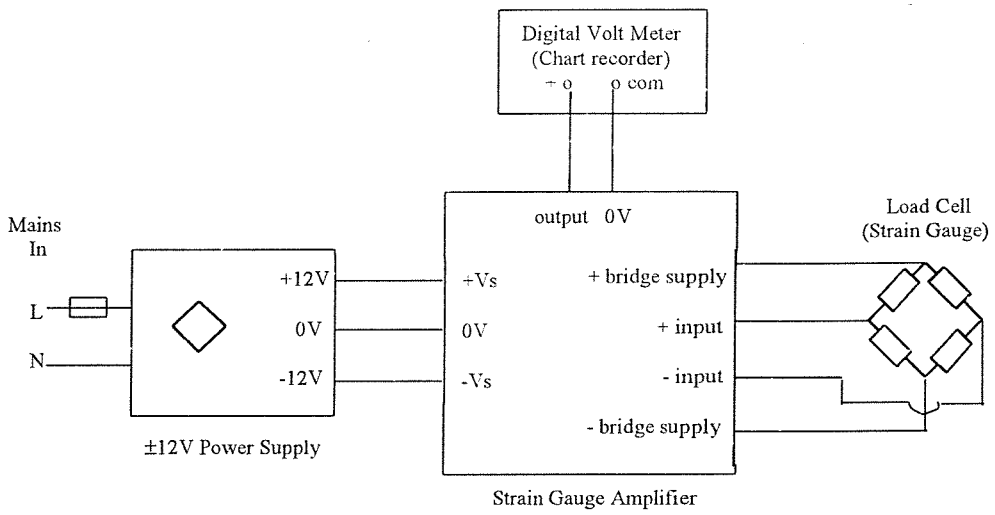

Figure 2.7: Simplified circuit diagram of the Strain Gauge Amplifier used for mechanical testing.

The quality of the fibre used was important for plastic deformation experiments as the behaviour of the samples was found to be variable; only those samples which had the same behaviour under stress (decrease in width, formation of a neck and propagation along the length) were considered for study.

2.4.1 Fibre Cold-Drawing Apparatus

A straightforward fibre cold-drawing apparatus was purpose-made to draw the fibre specimen in a controlled manner. The polyethylene fibre specimen was securely clipped at both ends. The lower clip was fixed on the bottom of the main frame, which itself was fixed in the cup. The drawing fibre length was 10 mm due to the restriction of the cup height. The fibre sample was immersed into glycerol and heated by the surrounding heating bands to a chosen temperature. The temperature can be maintained to ± 1°C. The upper clip was connected to a steel wire, which was held in a clamp bolted to a 2-kilo-load-cell. The load cell was bolted to the tool post of a Myford Super 7 mechanical lathe, so that the thread cutting facility provided a range of crosshead speeds. The draw ratio was determined by measuring the specimen lengths before and after drawing and ratioing the drawn length against the original length.

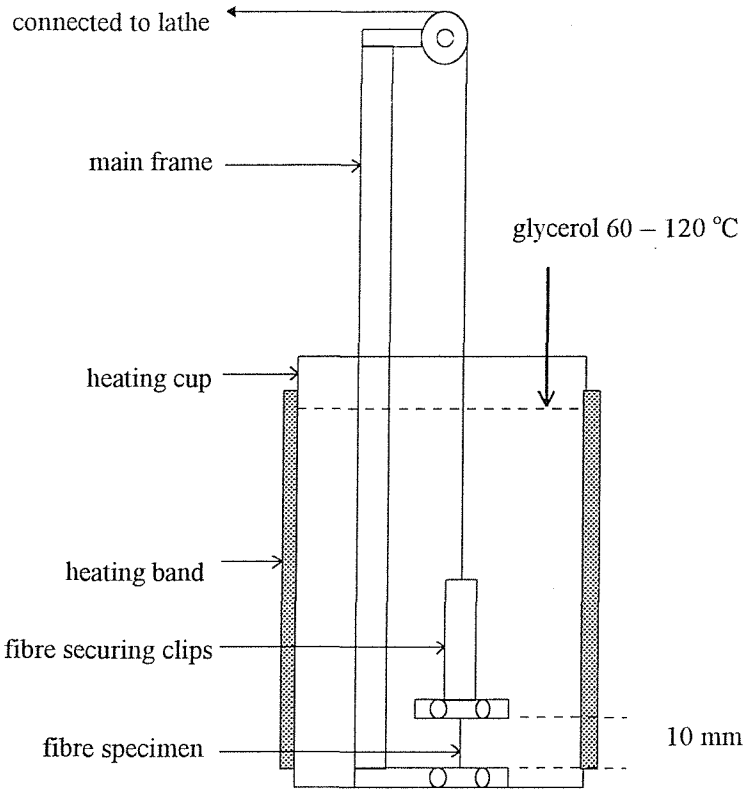

Figure 2.8: Schematic representation of the fibre cold-drawing apparatus

2.5 Annealing

The heat treatment of materials in order to relax stress or to reduce defects is termed "annealing". Annealing of PE fibres at a temperature close to but less than its melting point may activate internal mobility and promote greater stability by, for example, the elimination of stresses or defects in a general movement towards the thermodynamic equilibrium condition[13].

2.5.1 Theoretical treatment

The thermodynamic equation for a change of state is represented as

$$\Delta G = \Delta H - T\Delta S \qquad \text{(Eqn.2.5.1)}$$

where the terms have their usual meaning.

Considering the solid to liquid phase transition, ΔH is the heat of fusion of the material, subscripted ΔH_f. $T\Delta S$ increases with rising temperature until, at the melting point of the material, T_m, ΔG vanishes and the two phases exist in equilibrium.

Equation 2.5.1 applies to all low molecular weight, homogeneous materials that have a well-defined melting point. Polymers are, of course, high molecular weight materials of heterogeneous composition, and the melting point may be related to the heat of fusion by[14]

$$T_m = T_m^{\circ} [\, 1-2\sigma_e / \Delta H_f \, L] \qquad \text{(Eqn.2.5.2)}$$

where T_m° is the melting point of an infinitely thick crystal (146°C)
$2\sigma_e$ is the fold surface free energy
L is the lamellar thickness.

The lamellar thickness, L, may also be related to the heat of fusion, ΔH_f, by[15,16]

$$L = [\, 2\sigma_e \, T_m^{\circ} / \Delta H_f \, \Delta T] + \delta l \qquad \text{(Eqn.2.5.3)}$$

where ΔT represents the supercooling and δl varies slowly w.r.t. ΔT as a consequence of kinetic theory[14].

It is clear from equation 2.5.3 that the lamellar thickness decreases with increasing supercooling, and from equation 2.5.2 that the melting point decreases with decreasing lamellar thickness. This implies that a sample which has been rapidly quenched from the melt has thinner lamellae and a lower melting point than a sample allowed to crystallise at a temperature close to the melting point i.e. with a smaller ΔT, and this is known to arise.

2.5.2 Effects of Annealing

The thickness of crystals formed during crystallisation may be increased by heat treatment of the condensed phase. Raising the temperature of the solid material to a value close to its melting point increases the thickness of the lamellae; this follows of course from equation 2.5.3 above. Annealing polymer fibres increases the chain mobility within the crystal lattice to an extent where the lamellae are allowed to approach their thermodynamic equilibrium state more closely.

2.6 Initial Investigations of the Polymer Processing Rig

The Polymer Processing Rig produced was based on a small Baughan Laboratory extruder loaned to and then donated to the University by the EPSRC Polymer Engineering Directorate. The extruder operated horizontally but the original research had involved turning the direction of the flow from horizontal to vertical beneath the molten metal bath, as in Figure 2.9. At the start of the programme, it was pointed out that since one of the major problems in the past had been sealing the base of the molten metal bath to the unit below it therefore was logical in running the whole system vertically. A machine was therefore designed (by Dr. Y.D. West during her appointment to the project) around the barrel of the extruder set vertically, the drive system re-engineered, die and bath above the extruder flanges and wind-off facility positioned above that; the total height was around 3m.

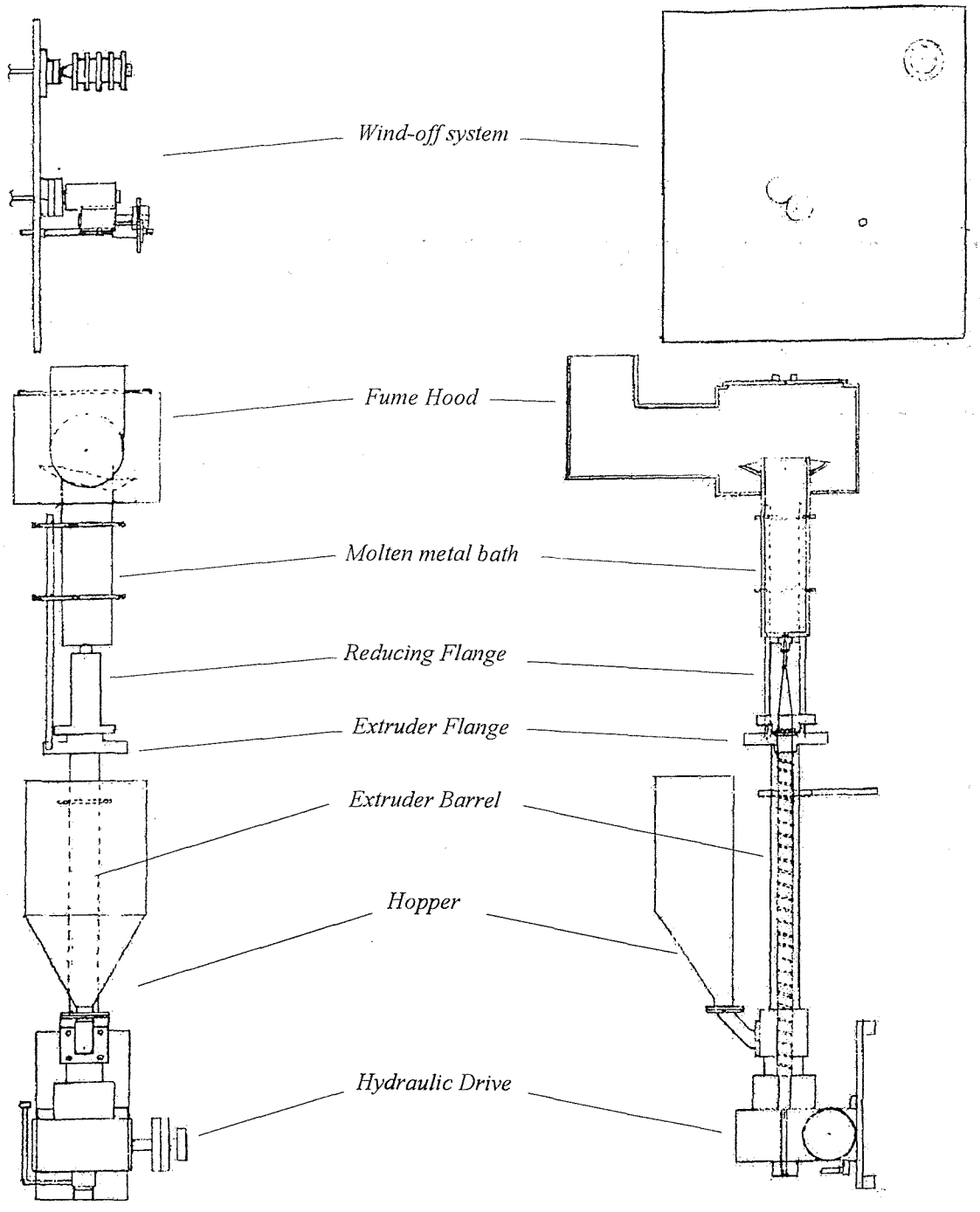

Figure 2.9: Schematic illustration of the original fibre spinning rig operating vertically

A wide range of operating conditions was investigated initially in order to determine the optimum conditions for the production of polyethylene monofilaments. The extruder was set up with an experimentally optimised increasing linear temperature gradient from 150 to 180 °C along its length; this temperature gradient was maintained throughout the course of these experiments.

In order to produce monofilaments it is essential to have a constant flow of polymer through the die. Necessarily this requires the uniform production of the polymer melt which must also be free of all inhomogeneities. To achieve this, it is also necessary to feed a constant amount (at a constant rate) of polymer directly onto the screw of the extruder barrel. A number of hopper units of varying design were produced and tested but all proved ineffective in giving consistent output of polymer fibre. On occasions a reasonable flow of polymer fibre was achieved from the die and enabled preliminary experiments to be carried out employing the molten metal bath. Varying the parameters of screw speed (0-20 rpm) and temperature gradient of the extruder / die assembly failed to give a reproducible, homogeneous and continuous flow of polymer from the die. In essence, the extruder assembly was a complete failure – the extruder was not feeding properly.

During the course of these initial experiments the rig suffered a major structural failure between the top of the extruder barrel and the filter pack /reducing flange unit. It should be stressed that melt pressures around >10000 p.s.i. were accidentally achieved and so failure had serious mechanical consequences. The rupture of the system caused the extruder flange/ bath assembly to be distorted in the process and thus the rig was dismantled for repair and as it turned out – complete redesign.

The reason for the failure was ascertained to have been the result of inappropriate pressure tolerances being allowed during the initial experimentation with the rig. The sample of polymer used may have also degraded with time (over a period of ~20 years) or possibly the melt viscosity may have been too high for this particular application. The exact reasons were never fully investigated during the time of these initial experiments (admittedly inexperience on behalf of the author) and the polymer was discarded.

The repair and reconditioning of the damaged components was successfully carried out by the Departmental Workshops. The extruder was rebuilt to operate horizontally (as it was originally manufactured) to eliminate the problem associated with the feeding. The original design of the extruding rig was such that adjustment to make the extruder operational in a horizontal position was easy. The new extruder rig incorporated a specially designed die block enabling polymer melt to flow from the reducing flange and be turned by 90 ° upwards through the die, see Figure 2.4. Hostalen GF7750M high density PE (extrusion grade for monofilaments) was selected as a starting material to determine the optimum conditions for the production of polyethylene fibres with the redesigned apparatus.

The extruder was set up with an increasing linear temperature gradient along its length from 150 to 190 °C. The temperature of the molten metal bath was set between 108 and 130 °C. Initial investigations were quite successful and numerous fibre samples were obtained. However, several problems also became evident. Firstly the extruder screw speed controller was unreliable hence giving a non-reproducible flow rate. It was thus necessary to monitor the flow rate; this was achieved by weighing samples of the extruded polymer at 1-minute-intervals. This process was repeated several times and an average taken. If the screw speed was too slow, fibre production was unstable and often discontinuous, whilst if the screw speed was too high, air bubbles were found in the fibre resulting in the material being inhomogeneous. A screw speed of 5 rpm was found to be optimal, allowing stable flow.

On a number of occasions, the polyethylene melt and/or molten metal leaked through the seal joining the die to the bath. A number of different seals were designed and tested. The arrangement illustrated in figure 2.10 was found to yield the best result. The seal design allowed the polymer to flow and be drawn directly from the tip of the die straight through the seal (without having to pass through any 'dead space' inside the seal itself) and easily through the oversized hole into the molten metal bath. The top 'O' ring stopped liquid metal from leaking around the outside of the seal while the lower 'O' ring prevented the liquid metal from leaking through the inside of the seal.

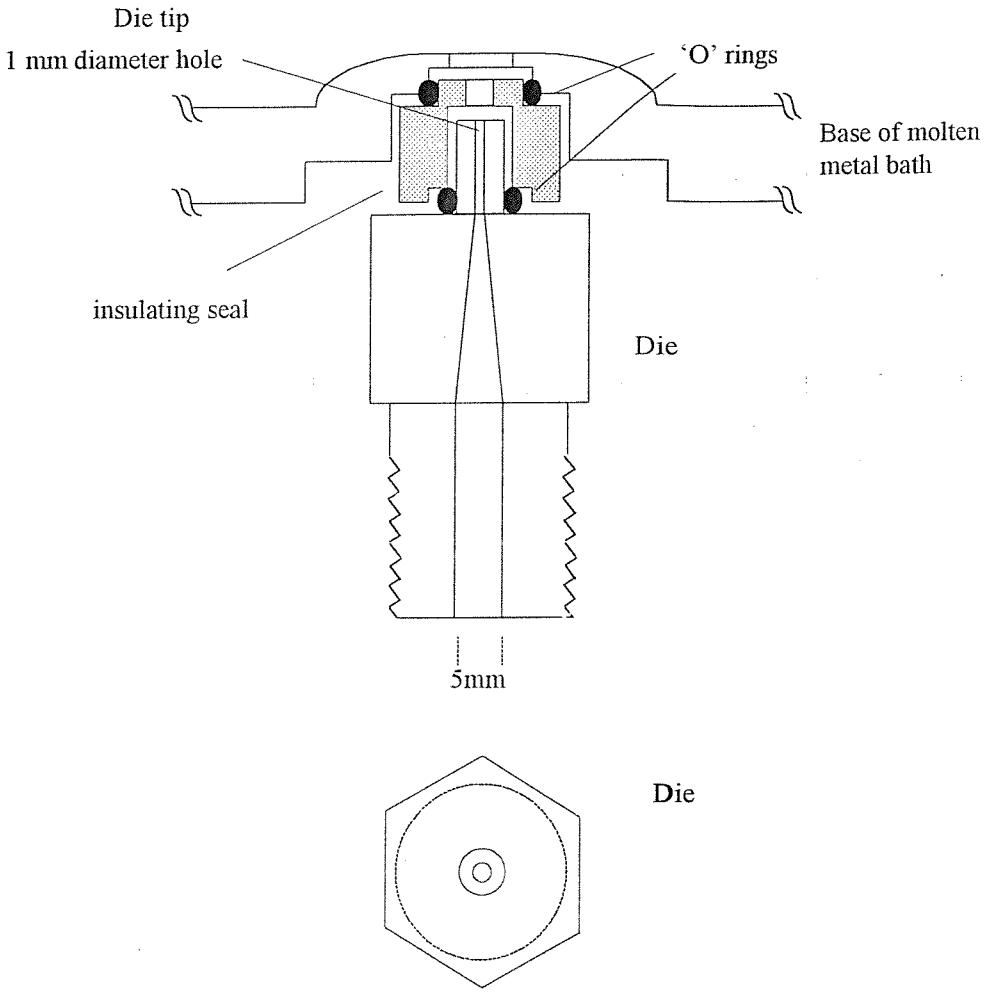

Figure 2.10: The seal and die assembly
(die section enlarged from figure 2.4)

Some initial spinning conditions and properties of the fibres obtained from polyethylene grade Hostalen GF7750M are presented in Table 1. The results presented were achieved working in collaboration with Dr. S. Lu during the period of his appointment to the project.

Table 1. Spinning conditions and properties of fibre obtained from GF7750M.

Sample number	Polymer spun through	Spinning speed m min^{-1}	Fibre diameter μm	Young's modulus GPa	Tensile strength MPa	Extension at break %
1	Air	100	330	1.6	380	1230
2	Air	100	300	1.5	490	1370
3	Sample 2*		120	4.2	570	15
4	Air	300	230	1.4	360	960
5	Air	300	260	1.9	370	570
6	Sample 5*		110	2.1	540	26
7	Metal/115 °C	60	420	1.2	50	56
8	Metal/112 °C	90	330	2.3	69	12

* specimen was re-tested for mechanical properties

It is clear from the results listed above that the fibres spun through air are quite different from those spun into molten metal. The fibres spun into air can be further extended by ~10 times before they fracture, whereas those spun into the molten metal are quite brittle and can only be extended by 50%.

Several factors may explain the mechanical properties obtained from the molten metal bath spun fibres. The fibre spun through molten metal may have a higher degree of orientation along the fibre axis due to the drag on the fibre in comparison with the fibre spun through air of the same diameter. The degree of orientation in the fibres limits the maximum achievable draw ratio. The polyethylene grade used may not have had the

appropriate molecular weight and molecular weight distribution for molten metal processing. It should also be noted that the relevant molecular weight data for the selection of different PE grades was not available from the supplier†. These initial investigations however allowed the candidate to gain experience with the molten metal bath technology, spinning operation and mechanical testing.

Following rather obscure advice from Hoechst UK Limited Polymer Division (suppliers of Hostalen grades of PE) GF4670 grade was "selected" for the next phase in the production of high performance fibres. At this stage (due to the time restriction on the project) it was decided to concentrate efforts on the possibility of a commercially interesting discovery.

Researchers at Southampton [11,12] had in the past carried out extensive investigations into the production of polyethylene fibres using molten metal bath technology. The fibres showed a decrease in diameter and an increase in modulus as the wind off speed at each temperature was increased. The decrease in fibre diameter was due to the fibre experiencing greater draw down at higher wind off velocities before crystallisation occurred to halt the draw down process. The higher degree of melt draw-down in-turn clearly produced a higher degree of orientation in the fibre and a corresponding increase in the observed modulus. It was also shown that the modulus of fibres spun into the molten-metal cooling bath was in excess of those spun into air at similar rates.

France[11] conducted experiments to assess the affect of drawing at elevated temperatures* produced with the molten metal bath at set 130 °C. Initial experiments determined the maximum achievable draw ratio at 90 °C. Drawing was attempted at 90 °C and 125 °C although the latter failed to produce a draw ratio in excess of $\lambda = 4$ before breakage of the fibres. Fibres drawn at 90 °C showed an increase in modulus and a decrease in fibre diameter. The fibre produced at 2.5 ms^{-1} showed the highest

† Considerable efforts were made to obtain the M_w & M_n values and of course, the molecular weight distribution of the polyethylene samples we could therefore access. Unfortunately the suppliers pleaded ignorance so we found the selection of materials very difficult and unsatisfactory.

* This process may still be referred to as 'cold drawing' since the temperature of the environment was below that of the crystalline melting point. 'Plastic deformation' at elevated temperatures might be a more suitable description.

achievable draw ratio at 90 °C before failure, consistently attaining high value λ. The corresponding modulus (40 times the value for an unoriented pressed sheet of the same polymer) were the highest achieved and exhibited the highest degree of crystalline orientation.

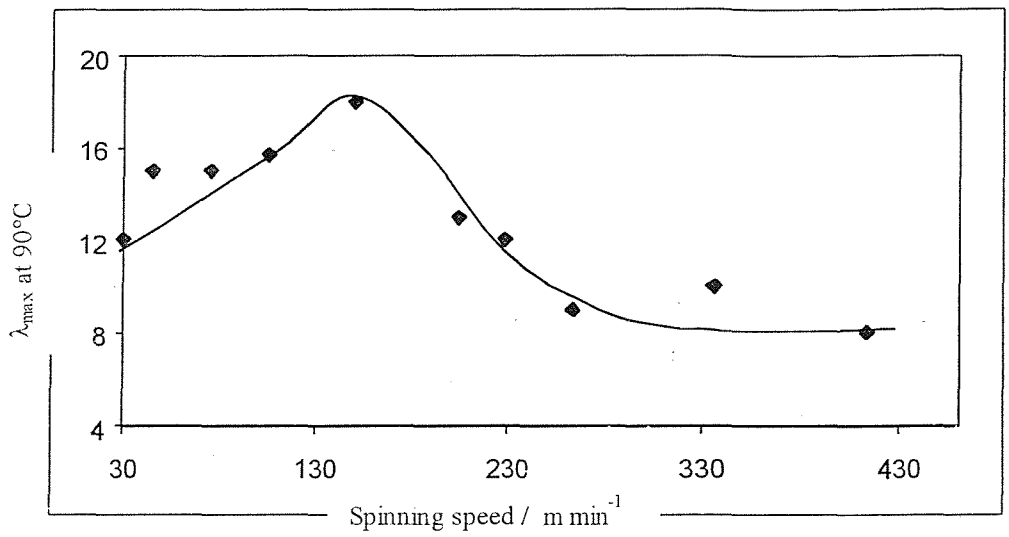

Figure 2.11. Plot of λ_{max} at 90 °C against spinning speed

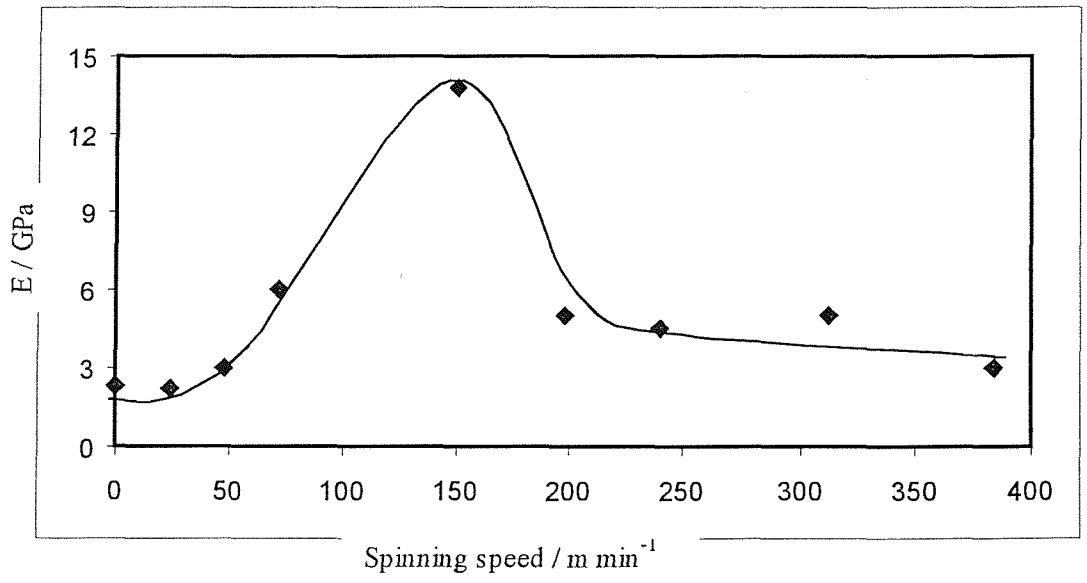

Figure 2.12. Plot of the corresponding modulus (E) against spinning speed.

Figure 2.11 shows a plot obtained by France of the maximum draw ratio at 90 °C (λ_{max} 90) against the original take-up velocity of the as-spun fibres, produced with the bath at 130 °C. The corresponding moduli of the fibres after cold stretching (tested at 18 °C) is shown in Figure 2.12. There is an obvious similarity between the two plots and hence the modulus of the material reflects the degree of drawing. The fibre produced at 150 m min^{-1} with diameter ~ 200μm showed the highest draw ratio, $\lambda = 18$, yielding a modulus of 13.8 GPa.

These results led the candidate to carry out further investigations into melt spinning through the molten metal baths followed by cold drawing as a method of producing a high modulus fibre with commercial potential.

2.7 Initial investigations with Hostalen GF4760

The wide range of running conditions described in section 2.5 were again repeated using Hostalen GF4760 grade PE. The extruder was again set up with an increasing linear temperature gradient along its length from 150 °C to 190 °C, and was maintained throughout the course of these experiments. The extruder screw speed set at 5 rpm was also found to be optimal for both flow stability and draw down of the fibre.

The effect of extruding the polymer through a smaller die (0.5 mm) was also investigated. The decrease in thickness of the fibre however made it significantly more difficult to spin and draw-down resulting in frequent fibre breakage. The melt pressures experienced in the extruder flange were found to be in excess of 12000 p.s.i. at a screw speed of 5 rpm which was considered as too high for the processing rig. Having experienced a major structural failure during initial testing in the past, a more cautious approach was taken during these experiments. The 1mm diameter die was thus selected.

The effect of varying the temperature of the molten metal bath was studied. It was found that the bath temperature had to be in excess of 104 °C to allow the polyethylene melt to flow evenly from the die and be wound on the collecting bobbins. The

maximum achievable take up velocity was expectedly[11-12] found to rise with increasing bath temperature, for example, at 130 °C the fibre can be spun at ~360 m min^{-1} with a thickness of ~100μm. The candidate conducted further experiments using France's technique of melt spinning through the molten metal followed by cold drawing to produce a high modulus fibre.

2.7.1 Results

In Table 2 an example is illustrated of some of the mechanical properties obtained from a 200μm fibre spun into air and cold drawn at 95 and 75 °C. The mechanical testing apparatus used during these experiments has been described in section 2.3.2.

Table 2. Fibre spun at 300 m min^{-1} through air, cold drawn and tested at room temperature.

Drawing Temp. °C	Draw ratio (λ)	Fibre diameter μm	Young's modulus GPa	Tensile strength MPa	Extension at break %
As spun ^{air}		200	0.9	560	650
95	8.7	95	3.4	314	
75	14.4	60	9.0	780	17.6

The most significant feature from these results is the high draw ratio achieved at 75 °C. The modulus of this fibre was 9.0 GPa which was 10 times greater than the as-spun specimen. The fibre drawn at 95 °C was found to behave like a brittle material when tested. The extension at fracture value was therefore not noted.

An examination was then carried out on series of fibres produced by spinning through the molten metal bath at 125 °C. The polyethylene was spun at a rate of 180 m min^{-1} and produced fibre with a diameter of 190μm. The modulus was measured and is presented in Table 3. The fibre was then annealed in an oven for 1 hour at 120 °C and

re-tested. Both fibre specimens gave identical moduli when tested. An interesting aspect however was the manner in which the as spun fibre behaved like a brittle material whereas the opposite was observed from the annealed fibre. The annealed fibre extended to almost twice its length before fracture when tested.

Table 3. Mechanical properties of as spun through molten metal bath at 125 °C and annealed fibre.

Fibre Specimen	Fibre diameter μm	Young's modulus Gpa	Tensile strength MPa	Extension at break %
Metal $^{125°C}$	190	2.2	64	
Annealed ^{120} °C	190	2.2	50	180

The fibre annealed at 125 °C for 1 hour was then subjected to cold drawing at a series of different temperatures using the experimental set up described in section 2.3.1. A plot of the maximum draw ratio (λ_{max}) against the cold drawing temperature is represented in figure 2.13. The highest draw ratio of 14.7 was achieved at a temperature of 70 °C. Plots of the corresponding Young's modulus and tensile strength against the cold drawing temperature for the series of fibres are illustrated in figures 2.14 and 2.15 respectively.

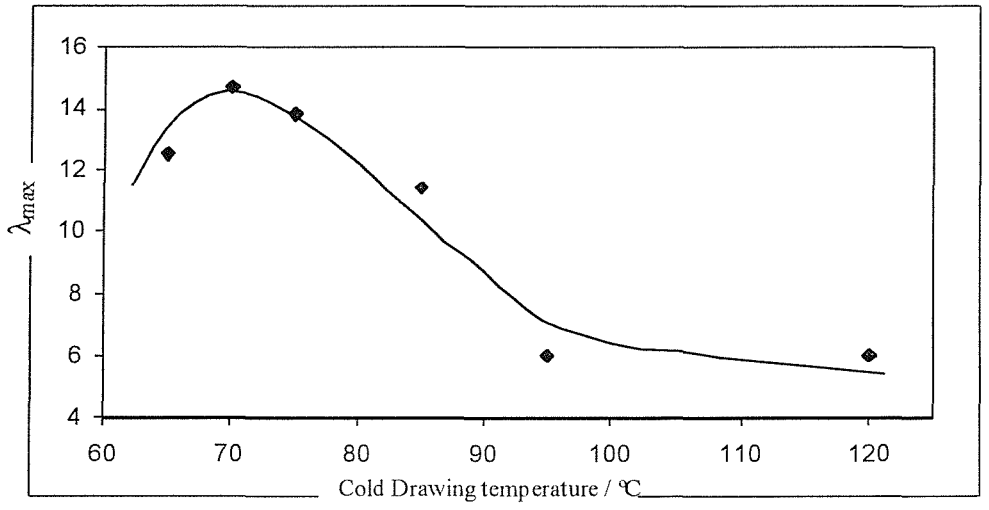

Figure 2.13. Plot of the maximum draw ratio (λ_{max}) against cold drawing temperature

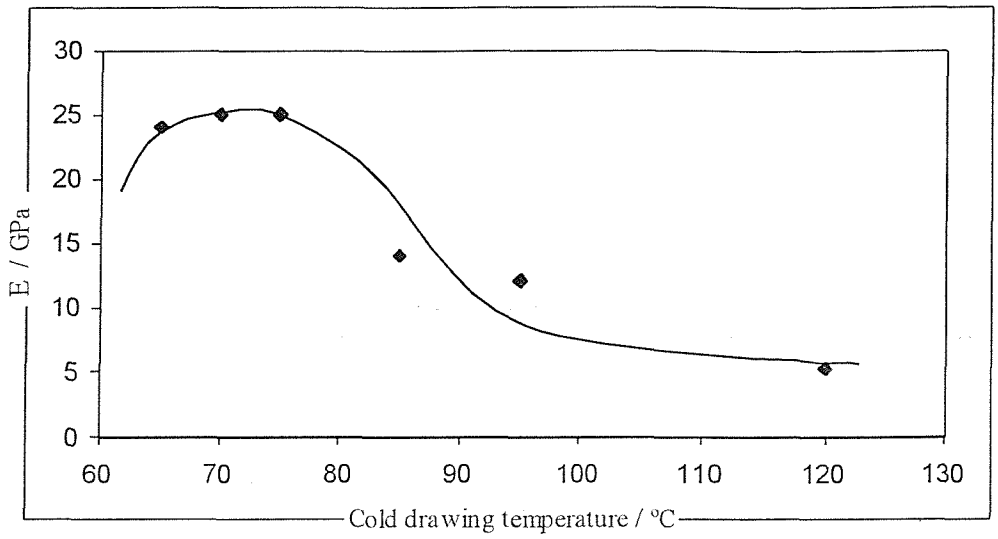

Figure 5.4. Graph of the Young's modulus (E) against cold drawing temperature

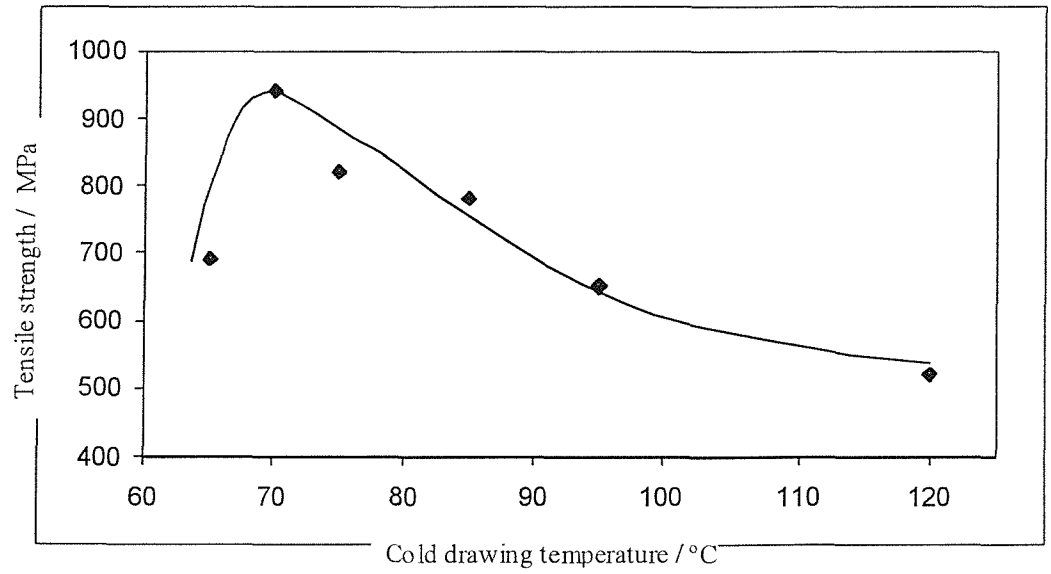

Figure 5.5. Graph of the tensile strength against cold drawing temperature

There is an obvious similarity between the three plots. The modulus of the fibres reflects the degree of drawing. The fibres that were cold drawn at 70 °C showed the highest draw ratio and consistently attained a value of $\lambda \approx 15$. The corresponding tensile modulus of this fibre at 25 GPa and strength approaching 1 GPa was the highest achieved and is significantly enhanced in comparison with those previously obtained. The maximum draw ratio was found to be less than that reported by France however this may simply be a consequence of the grade of polymer which was used. The increased tensile modulus achieved from these fibres is in support of a higher degree of orientation being present, which may in turn limit λ_{max}.

Table 4. The variation of fibre diameter and extension at break with the drawing temperature.

Drawing Temp. °C	**Draw ratio (λ)**	**Fibre diameter μm**	**Extension at break %**
120	6	85	
95	6	90	
85	11.4	80	
75	13.8	75	15
70	14.7	70	12
65	12.5	75	8.9

During the cold drawing process, the samples extended by necking and displayed the whitening characteristic of void formation[1]. This would explain the non-linear relationship between the draw ratio and the fibre diameter from the results presented in table 4. The values for extension at break were again not noted for the brittle fibres when tested. The results serve only as an indication of the potential that molten metal bath melt spinning offers for the production of high modulus fibres. The results are promising but it is strongly felt that they can be further improved upon using a more appropriate grade of polyethylene for the technology.

2.8 References

1. A. Keller and P.J.Barham, Plastics and Rubber International, February, Vol.6, No.1, 1981, p.19.
2. G. Cappaccio and I.M. Ward, Nature Phys. Sci., 243 (1973) 143.
3. A. Zwijnenberg and A. J. Pennings, J. Polym. Sci., Polym. Lett. Edn., 14 (1976) 339.
4. P. Smith and P.J. Lemstra, J.Mater. Sci., 15 (1980) 505.
5. I.M. Ward, Plastics, Rubber and Composities Processing and Applications, Vol. 19, No.1, 1993, p.7.
6. R.H. Olley, D.C. Bassett, P.J. Hine and I.M. Ward, J. Mater. Sci, 28,4 (1993) 1107.
7. A. Grefenstein, S. Herren, P. Hock, K. Kocker and J. Vanmarwick, Eng. Plasts, 7, 6 (1994) 391.
8. N.E. Weeks and R.S. Porter, J. Polym. Sci., Polym. Phys. Edn., 12 (1974) 635.
9. K. Nakamura, K. Imada and M. Takayanagi., Int. J. Polym. Mater., 2 (1972) 71.
10. A.G. Gibson, I.M. Ward, B.N. Cole and B. Parsons., J. Mater. Sci., 9 (1974) 1193.
11. C.N. France, Ph. D Thesis, University of Southampton, 1988.
12. C. Hodges; Ph. D Thesis, University of Southampton, 1994.
13. D.C. Bassett, "Principles of Polymer Morphology", Cambridge University Press, 1981.
14. J.D. Hoffmann and J.I. Lauritzen, J. Appl. Phys. 44, 4340, (1973).
15. F.C. Frank and N. Tosi, Proc. R. Soc. A263, 323, (1961).
16. G.V. Fraser, A. Keller and J.A. Odell, J. Appl. Polym. Sci. 22, 2979-89 (1978).

3. Chapter Three: Vibrational Spectroscopy: Theory and Instrumentation

Over the course of this century, vibrational spectroscopy has evolved into a very powerful, yet routine analytical technique. Both infrared and Raman spectroscopies offer us the opportunity to study the structural and morphological properties of a large variety of materials. Applications have been developed to a stage appropriate for rapid, routine and convenient analyses of most liquids and solids.

The underlying principles of vibrational spectroscopy remain as important a foundation as ever. It is with this in mind that a brief account of the fundamentals of molecular vibrations and basic instrumentation is described in this chapter.

3.1 Vibrational Spectroscopy

In any molecule, the atoms are in continual motional state, oscillating or vibrating about their equilibrium positions. Gas phase molecules are free to rotate freely about their three orthogonal axes. The angular velocities about these three axes can only have precisely permitted values, i.e. the rotational energy of the molecules is quantised. Molecules can only change their rotational energy level by taking in or releasing an amount of energy equivalent to the difference in energy between two of its states.

In addition to rotation in the gas phase, molecules vibrate at all times and these vibrations also have quantised energy levels. Transitions between these levels generally occur via the emission or absorption of energy as electromagnetic radiation. The study of this interaction between electromagnetic radiation and molecular vibrations, as a function of the energy of the radiation forms the basis of *vibrational spectroscopy*.

Molecules exhibit a complex series of vibrations which area superposition of many fundamental modes of vibration. A fundamental mode of vibration occurs when all the nuclei undergo harmonic vibrations at the same frequency and move in phase, not necessarily with the same amplitude, and with the centre of mass remaining fixed.

N atoms in a molecule can be modelled as a series of point masses connected by springs such that when the spring and mass arrangement is set into motion a complicated movement results. Each atom within a molecule has three possible motions corresponding to the (arbitrary) orthogonal co-ordinate system, X, Y and Z. The total number of co-ordinates required to specify the location of all N atoms is 3N. Three co-ordinates are needed to specify the location of the centre of mass of the molecules, and so three of the displacements correspond to the translational motion of the molecule as a whole. Of the remaining 3N-3 non-translational 'internal' modes of the molecule, 2 (linear) or 3 (non-linear) co-ordinates describe rotational displacements. This leaves 3N-5 (linear) or 3N-6 (non-linear) displacements which yield the number of fundamental modes of vibration in a molecule.

The vibrations of a diatomic molecule may be approximated using the convenient but acceptable model of the simple harmonic oscillator. Two masses m_1 and m_2 are connected via a spring with a restoring force proportional to displacement, hence following Hooke's law with a spring constant, or modulus, k (Nm^{-1}).

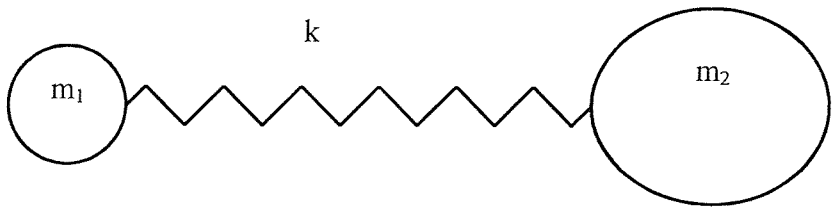

Figure 3.1: The ball and spring model

When m_1 and m_2 are set into motion the arrangement vibrates with simple harmonic motion (SHM) about the centre of mass and with a frequency given by the well known relationship

$$\nu = \frac{1}{2\pi}\sqrt{\frac{k}{\mu}} \qquad (3.1)\ ;\ (3.2) \qquad \mu = \frac{m_1 m_2}{m_1 + m_2}(kg)$$

where μ is known as the reduced mass.

The potential energy, V, at displacement r is given by the parabolic function

$$V = \frac{kr^2}{2} \qquad (3.3)$$

The model is a reasonable approximation but is over simplistic; in a real molecule one of the atoms could be displaced to the point where the bond breaks. Molecules actually vibrate anharmonically and the potential energy versus displacement curve is not parabolic. One of the older but reasonably accurate analytical descriptions is the "Morse function", derived in 1929[1] and shown below:

$$V = D_{eq}[1-\exp\{ a (r_{eq} - r) \}]^2 \qquad (3.4)$$

where

D_{eq} = the dissociation energy

r_{eq} = the equilibrium bond length

r = internuclear distance

a = constant for a particular molecule

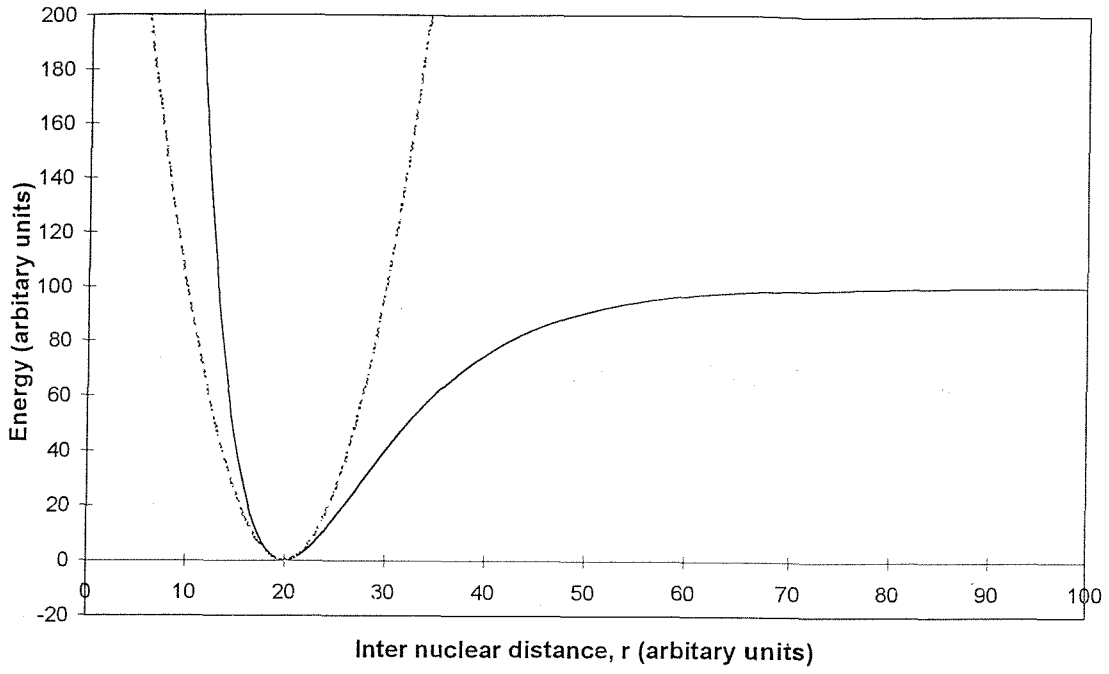

Figure 3.2: A comparison of Morse and simple harmonic potential energy approximations for a diatomic molecule.
The simple harmonic approximation and the Morse function are shown by the dotted and full lines respectively.

Schrödinger's time independent equation solved for the Morse potential function yields a set of discrete energy levels which converge rapidly as the dissociation energy is approached.

The Morse potential function is an approximation based on a solution of the form in equation (3.6) below; the full series for the energy levels will be

$$E_v = hc\nu\,[(V + 0.5) - X_e(V + 0.5)^2 + Y_e(V + 0.5)^3 + \text{higher order terms}] \qquad (3.5)$$

The Morse potential function gives

$$E_{vib} = h\,[(V + 0.5)\,\nu_{vib} - (V + 0.5)^2\,\nu_{vib}\,X_e] \quad \text{Joules} \qquad (3.6)$$

where

ν = vibration wavenumber of the SHM model, in Hz
c = speed of light
h = Planck's constant
V = 0, +1, +2, +3, the vibrational quantum number
X_e = anharmonicity constant

The permitted energy levels for a molecule if drawn on the Morse curve would consist of a series of horizontal lines which converge as V increases. Therefore changes in the energy of a molecule are accompanied by the absorption or release of a quantum of energy corresponding in the difference in energy between the two states.

The anharmonicity constant describes the deviation of the allowable energy levels compared with the SHM approximation. X_e is usually quite small, ~ 0.02. Subsequently for small displacements both the Morse function and the SHM approximation are very similar, and so the SHM model can be used as a valid approximation for much of vibrational analysis.

3.1.1 Infrared Activity

If during the course of a vibration a change in the dipole occurs, then electromagnetic radiation can interact with this fluctuating dipole, μ, given that the energy of the incoming photon matches that of the vibrational transition. Figure 3.3 represents the energy of a fluctuating dipole with the so called *normal co-ordinate*, q, which represents the progress of the vibration, given in units of phase angle between 0 and 2π radians.

The selection rule governing infrared activity is given by the following expression,

$$\left(\frac{\partial \mu}{\partial q}\right)_{q=0} \neq 0 \qquad (3.7)$$

where q_0 is the equilibrium position of the vibration.

If we consider the symmetric stretching vibration, ν_1 of CO_2, we can observe that although the oxygen atoms move with respect to the carbon atom, the relative separation between each O atom and the C atom is always equal. Consequently, the vibration does not produce a change in dipole, and is not IR active. On the other hand, for ν_3, and $\nu_{2,4}$, the dipoles can be seen to change, the selection rule is obeyed, and absorption bands are observed in the IR spectrum.

(a)

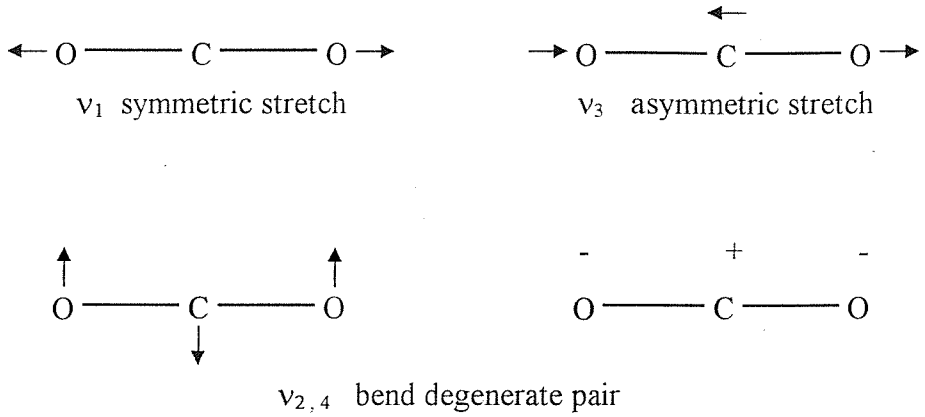

Figure 3.3 (b)

(b)

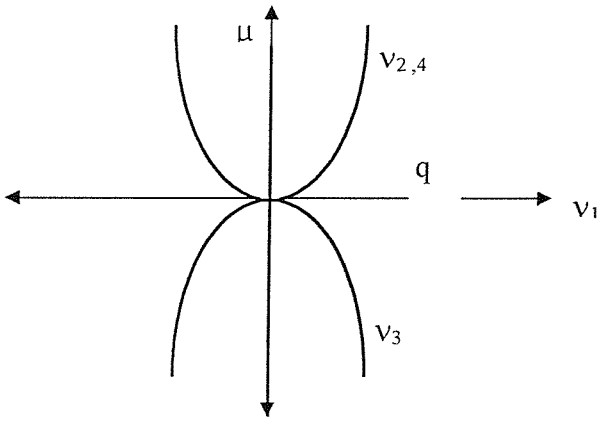

Figure 3.3: (a) The fundamental vibrational modes of CO_2
(b) The plot of dipole moment versus q for the vibrational modes.

3.1.2 The Raman effect

All molecular systems have a property called a *bulk polarizability*, α_0, which gives rise to properties such as dielectric constants and the index of refraction. Polarizability is a difficult concept to visualise, but can be explained as the ability with which electrons within a molecule can be induced to move around the molecule under the influence of an applied field. Thus, when a molecule is place in an electric field, its natural electron distribution will be distorted. Separation of negatively charged electrons within the field creates a dipole, P, whose direction is opposite to that of the applied field. This induced dipole is related to the field and the molecular polarizability, α, by the following expression,

$$P = \alpha E \qquad [Vm^{-1}] \tag{3.8}$$

If the field is the component of an electromagnetic radiation field of frequency ν_0 (Hz) then the induced dipole will oscillate with the same frequency as the electric field.

$$P = \alpha E_0 \cos(2\pi\nu_0 t) \tag{3.9}$$

where t = time and E_0 = maximum amplitude of the electric field (Vm^{-1}).

If this irradiated molecule is already vibrating at a frequency ν_{vib}, its distortion from its equilibrium position is given by

$$q = q_0 \cos(2\pi\nu_{vib} t) \tag{3.10}$$

where q_0 is the maximum distortion (or amplitude) and ν_{vib} is the vibration frequency in hertz. The vibration frequency arises directly from the energy, $E=hc\nu$.

Equation (3.8) assumes that α does not change during the cycle of a vibration. However, for the more general case where α is a function of the position q, along the axis of the vibration, assuming small vibrational amplitudes, α can be expanded in a Taylor series of the normal co-ordinate q_0.

$$\alpha = \alpha_0 + \left(\frac{\partial \alpha}{\partial q}\right)_{q=0} q + \frac{1}{2}\left(\frac{\partial^2 \alpha}{\partial q^2}\right)_{q=0} q^2 + \textit{higher order terms} \tag{3.11}$$

The second and higher order terms give rise to the Hyper Raman Effect but are so small that they can be effectively ignored. Substituting equation (3.10) into equation (3.11) yields an expression for the polarisability as a function of q

$$\alpha = \alpha_0 + \left(\frac{\partial \alpha}{\partial q}\right)_{q=0} q_0 \cos(2\pi \upsilon_{vib} t) \tag{3.12}$$

which gives

$$P = \alpha_0 E_0 \cos(2\pi \upsilon_0 t) + \left(\frac{\partial \alpha}{\partial q}\right)_{q=0} q_0 \cos(2\pi \upsilon_{vib} t)\cos(2\pi \upsilon_0 t) \tag{3.13}$$

This can be simplified using the trigonometric identity

$$\cos A \cos B = \tfrac{1}{2}[\cos(A+B) + \cos(A-B)] \tag{3.14}$$

and equation (3.13) becomes

$$P = \alpha_0 E_0 \cos(2\pi \upsilon_0 t) + \tfrac{1}{2}\left(\frac{\partial \alpha}{\partial q}\right)_{q=0} q_0 [\cos(2\pi(\upsilon_0 + \upsilon_{vib})t) + \cos(2\pi(\upsilon_0 - \upsilon_{vib})t)] \tag{3.15}$$

Thus, the induced dipole in a molecule vibrating with frequency ν_{vib} and irradiated with frequency ν_0, will vary as ν_0 as well as $(\nu_0-\nu_{vib})$ and $(\nu_0+\nu_{vib})$. Immediately after the radiation is incident, the polarised molecule attains a higher energy than the molecule in its equilibrium state. Therefore, the polarisation process is endothermic and relaxation to a lower energy must be accompanied by a release of energy. When the energy is released as a photon, it is referred to as *scatter*.

An oscillating dipole emits radiation corresponding to it's oscillation frequency. The radiation emitted by the dipole corresponding to ν_0, the incident laser frequency and gives rise to Rayleigh or *elastic* scattering. Two *inelastic* scattering components correspond with the Raman light, and occur at lower frequency (ν_0-ν_{vib}), called the *Stokes* (red shifted) scatter, and at higher frequency (ν_0+ν_{vib}), called the *anti-Stokes* (blue shifted) Raman scatter.

The processes can be depicted as shown in figure 3.4. V_0, V_1, V_2, ... correspond to the discrete energy levels for vibrational quantum numbers V=0,1,2,.. respectively. V' and V" are virtual energy states which are not solutions of the Schrödinger equation but represent the short lived ceiling, associated with the laser excitation wavenumber ν_0.

The virtual states are not fixed but are dependent upon the incident exciting radiation ν_0 , which enables Raman scatter to be produced from an excitation source with any wavelength, resulting in UV, visible and near infrared excitation sources.

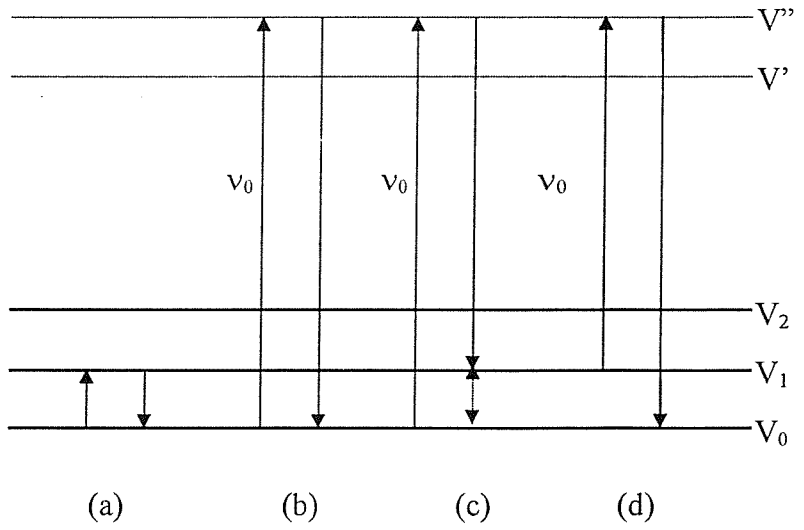

Figure 3.4: The energy level diagram showing the origins of infrared and Raman spectroscopy.

(a) infrared absorption *(b) Rayleigh scattering*

(c) Stokes Raman *(d) Anti-Stokes Raman*

For Raman scattering to occur, a change $\Delta V = \pm 1$ is required in the vibrational quantum number, corresponding to he molecule decaying to a state of greater or lower energy. If $\Delta V = +1$, there is a net energy absorption by the molecule, and the radiation is Stokes scattered at $\nu = \nu_0 - \nu_{vib}$. Conversely, if $\Delta V = -1$, the molecule loses energy, and the radiation is anti-Stokes scattered at $\nu = \nu_0 + \nu_{vib}$. For the $\Delta V = 0$ transition, the scattered radiation occurs at the same frequency as the excitation (Rayleigh scatter).

The relative intensity of the Stokes and anti-Stokes Raman bands can be determined by the relative populations in the ground and first excited vibrational states between which vibrational transitions take place. The relative populations of these two states is calculated from the Boltzmann distribution.

$$\left(\frac{I_{AS}}{I_S}\right) = \frac{(\upsilon_0 + \upsilon)^4}{(\upsilon_0 - \upsilon)^4} \exp\left(\frac{-hc\upsilon}{kT}\right) \tag{3.16}$$

It is apparent from equation (3.15) that Raman scattering only occurs when there is a change in the polarisability during the vibration. That is, the selection rule requires a finite change in polarisability so that

(3.17)

$$\left(\frac{\partial \alpha}{\partial q}\right)_{q=0} \neq 0$$

Analogous to figure 3.3b, the change in polarisability for carbon dioxide as a function of phase angle may also be plotted.

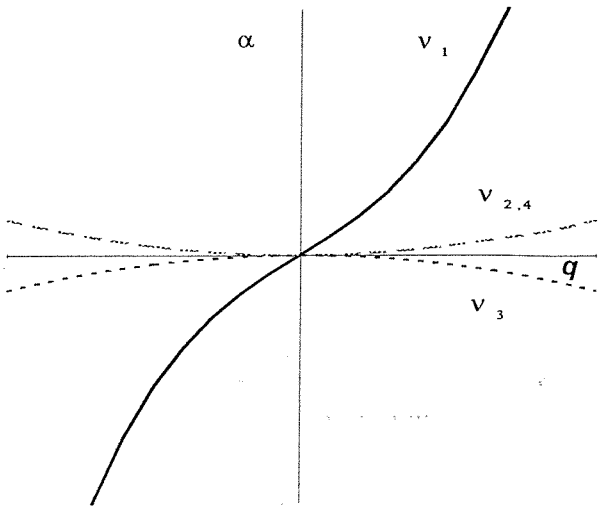

Figure 2.5: The plot of polarisability versus normal coordinate q

For the ν_1 vibration the polarisability shows a large change around q=0; thus this mode is Raman active. However for ν_2, ν_3 and ν_4 the polarisability does not exhibit such a change, and so these modes are not Raman active. The example of carbon dioxide displays the property of "mutual exclusion", that is vibrations that give rise to infrared absorptions do not appear in the Raman spectrum and vice versa. This applies only to centrosymmetric molecules.

The above derivation for Raman activity applies to an isotropic situation. Considering the model of a set of nuclei connected with springs with different k values then if one of the atoms is moved by a force applied in the x direction (arbitrarily), then the displacement of the other atoms may move in any of the x, y and z directions by different amounts. The same is true for a force applied in the y and z directions. Using this analogy polarisability under an applied field, α, also behaves in this way, and as such is said to be anisotropic. The anisotropy is described by a tensor such that $P=\alpha E$ becomes

$$\begin{pmatrix} P_{ix} \\ P_{iy} \\ P_{iz} \end{pmatrix} = \begin{pmatrix} \alpha_{xx} & \alpha_{yx} & \alpha_{zx} \\ \alpha_{xy} & \alpha_{yy} & \alpha_{zy} \\ \alpha_{xz} & \alpha_{yz} & \alpha_{zz} \end{pmatrix} \begin{pmatrix} E_x \\ E_y \\ E_z \end{pmatrix} \qquad (2.18)$$

or

$$\underline{P} = \alpha_{ij}\,\underline{E} \qquad (2.19)$$

where

$\underline{P}$ = resultant induced dipole vector

α_{ij} = polarisability tensor

$\underline{E}$ = applied electric field

In general α_{ij} reduces to a symmetric matrix with six independent components, i.e. $\alpha_{ij} = \alpha_{ji}$.

Since the selection rules governing infrared and Raman activity are different, both methods are complementary in contributing information about the vibrational degrees of freedom of any molecule. A general rule is that the higher the molecular or crystalline symmetry, the lower the likelihood that normal modes are both infrared and Raman active. In addition the rule of mutual exclusion requires that: if a molecule has a centre of symmetry then Raman active vibrations are infrared inactive, and vice versa. If a molecule has no centre of symmetry then some (but not necessarily all) vibrations may be both Raman and infrared active.

3.2 Fourier Transform Instrumentation

In recent years many Raman and infrared experiments have been carried out on Fourier transform (FT) instruments. The basic component of a FT spectrometer is an interferometer based on the two-beam interferometer originally designed by Michelson[2] in 1891. The general arrangement of these instruments are shown in figure 3.6 below.

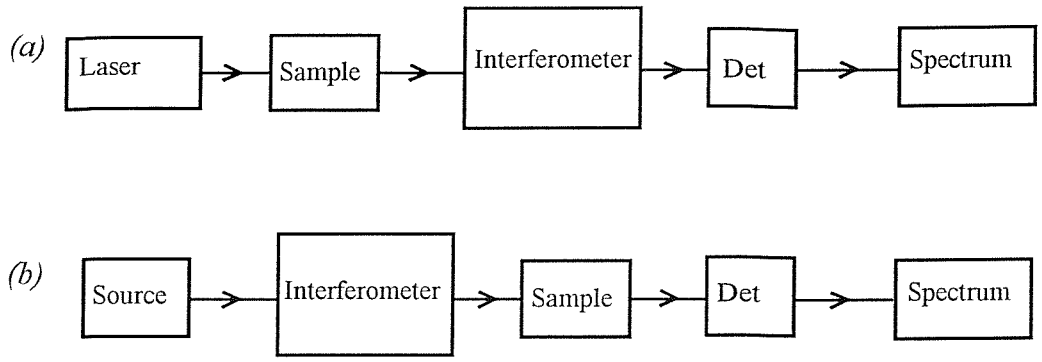

Figure 3.6 Schematic diagram of FT (a) Raman and (b) infrared spectrometers

3.2.1 From Interferogram to Spectrum

The optical diagram for the simplest form of the Michelson interferometer is shown in figure 2.7. The device passes a collimated beam of radiation towards a 50:50 beamsplitter (made of KBr for infrared and quartz for near infrared excited Raman) where it is split by reflectance and transmission into roughly equal parts. One beam of light is transmitted towards a fixed mirror and the second is deflected towards a moving mirror. It should be noted that some interferometers e.g. Perkin Elmer instruments, both mirrors can in fact move, one toward and the other away from the beamsplitter. Both of these plane mirrors are 100% reflective and the beams recombine at the beamsplitter. Interferences are produced as a function of the optical path difference (OPD) that the beams have experienced. It is this variation which ultimately yields the spectral information required. The semi- reflective nature of the beamsplitter is such to cause the interference pattern to be passed not only on towards the detector, but also back out through the entrance path.

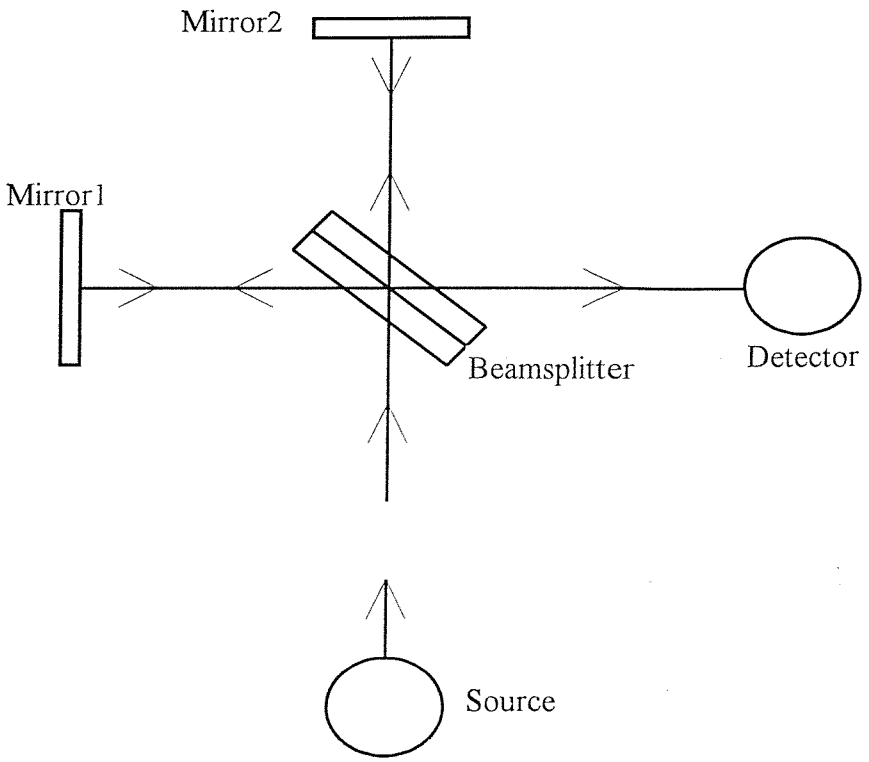

Figure 2.7: Schematic diagram of a Michelson interferometer.

If monochromatic radiation emitted by a source, wavelength λ_0 (in cm) and hence wavenumber ν_0 (cm^{-1}) enters the interferometer, assuming that the beamsplitter is ideal, there is path difference, or retardation, δ, between the difference in the lengths of the paths of the two beams. This is known as the OPD (optical path difference).

Constructive interference occurs when,

$$\delta = n\lambda_0$$

$$\text{where } n = 0, \pm 1, \pm 2, \ldots$$

and destructive interference occurs when,

$$\delta = (n + \tfrac{1}{2}\lambda_0)$$

Displacing the moving mirror by $\lambda/4$, and so adding a further path difference of λ, causes constructive interference again. It should noted with monochromatic radiation that it is not possible to distinguish between zero retardation and retardation equal to an integral number of wavelengths.

If the optical path difference (OPD), is changed as a function of time, i.e. if one of the mirrors are moved at constant velocity, the signal at the detector will be measured as a cosinusoidally varying amplitude. By mathematical manipulation, the resultant signal monitored at the detector may be written as a function of time or OPD. The following equations are presented as a function of OPD.

$$I(\delta) = 0.5\ I_0\ (\nu_0)\ \{\ 1 + \cos 2\pi\delta/\lambda\ \} \qquad (3.20)$$

$I_0\ (\nu)$ = intensity of the source

ν_0 = wavenumber of the monochromatic radiation

(for HeNe laser 15802.8cm^{-1} in vacuo)

The signal at the detector, called an interferogram, depends on the OPD, and will therefore be a function of the OPD velocity and thus the scan speed. This is typically 0.1 to 1.0 cm s^{-1}. Furthermore the information about the wavenumber of the source is independent of a set scan speed.

The interferogram comprises of the modulated component of the signal, the AC component, at the detector. For an ideal interferometer the modulated component of the signal is given as

$$I(\delta) = 0.5\ I\ (\nu_0)\{\ \cos 2\pi\nu_0\delta\ \} \qquad (3.21)$$

However, the interferometer is not ideal i.e. the beamsplitters do not perfectly reflect and transmit 50% of the radiation and so equation 3.21 must modified using a single wavenumber dependent factor, $H(\nu_0)$. Combining $H(\nu_0)$ and $I(\nu_0)$ into $B(\nu_0)$,

$$I(\delta) = B(\nu_0)\ \{\ \cos 2\pi\nu_0\delta\ \} \qquad (3.22)$$

where $B(\nu_0)$ is the source intensity at ν_0 modified by the instrumental characteristics.

Spectral information within the signal can be obtained by carrying out a Fourier transform. In 1822 J.J.B.Fourier published his analysis of heat conduction which provided the basis of Fourier Transform theory[3]. The basic principle states that any function can be represented by a superposition of a continuum of trigonometric functions of different amplitudes. Moreover, in this case, if F(t) is the function in the time domain and f(ν) is the same function in the frequency domain, it is possible to switch between the two domains by the means of a Fourier Transformation.

$$F(t) = \int f(\nu) \cos 2\pi\nu\delta \, d\delta \qquad (3.23)$$

$$f(\nu) = \int F(t) \cos 2\pi\nu\delta \, d\nu \qquad (3.24)$$

The above equations assume that F(δ) is a summation of symmetric functions, i.e. a series of cosines centred about zero path difference, from +∞ to -∞.

The final spectrum is calculated by computing the cosine Fourier transform of I(δ). All modern FT spectrometers use a computer algorithm based on the "fast Fourier transform (FFT)" devised by Cooley and Tukey in 1965[4]. The algorithm reduces the number of arithmetic operations required from N^2, where N is the number of sampled data points to $N\log_2 N$.

Performing the Fourier Transform of a measured interferogram of a monochromatic source is a trivial exercise, however taking the process further for several spectral lines or continuous radiation, the measured interferogram is the resultant of all the interferograms corresponding to each wavenumber. These interferograms from all the wavelengths superimpose at zero path difference and hence add together to give a beat frequency which is so long it produces a characteristic *centre burst*.

In principle by measuring the complete interferogram from -∞ to +∞ a complete spectrum of infinite resolution can be acquired. To achieve this one of the mirrors in the interferometer would need to move through an infinite path difference (δ) and the interferogram calculated

at infinitely small intervals. If one samples the interferogram at interval d, and δ has length l, then the number of data points available for computation is l/d and hence the resolution however defined can never exceed l/d. The effect of limiting δ is to cause the spectrum to attain a finite resolution.

3.2.2 Data Point Resolution

To sample data points along the interferogram a low power Helium neon (HeNe) is used to trigger the collection of each point. As the interferometer is moved, typically over a distance of 10 mm in a time period of 1 s, the intensity at the detector is sampled several thousand times at the zero cross-over point of the independently measured interferogram of the HeNe laser. This procedure triggers an analogue to digital converter (ADC) which places the data serially into the same number of storage points in a computer memory. The HeNe beam passes through a parallel and optically identical set of optics as the rest of the analysed radiation which means that any physical disturbances (e.g. knocks) will affect both the HeNe and experimental beams of radiation similarly and data sampling is still triggered at the appropriate points. The wavelength of the HeNe laser is 632.8 nm, so that for every centimetre of optical path difference an instrument will collect 31606 data points if it samples at the zero intensity crossing points of the reference laser interferogram. Thus, the interferograms of the infrared or near infrared will comprise 31606 numbers. If the interferogram is double sided the number will be 63212 which has advantages in phase in phase correction.

Resolution is limited to the number of data points acquired and hence the moving mirror's disturbance of travel. The digitalized interferogram is then processed by a computer, which carries out the Fourier transformation, to produce the spectrum, which is in reality a histogram. Depending on the manufacturer of the instrument, the computer either carries out the transformation immediately after each scan, producing a *pseudo* real-timeout spectral accumulation (e.g. Perkin Elmer instruments), or it carries out the transformation at the end of the accumulation of superimposed interferograms, to give the spectrum.

3.2.3 Nyquist Criterion[4]

The Nyquist or sampling theorem requires that a data point be taken at least twice every wavelength in order to accurately produce a given wave or band form by discrete sampling. Therefore, for a typical 2 cm^{-1} resolution spectrum, a data point should be presented every 1 cm^{-1} . In practical terms this means that the interferogram must be sampled at a minimum of twice the frequency of the shortest wavelength of interest in the required spectrum. The highest frequency that can be reconstructed from a sampled data set using, for example, a HeNe laser as the reference scale is 15802 cm^{-1} ; This is known as the Nyquist limit .

3.2.4 The advantages of FT over Conventional Spectrometers

The Jacquinot advantage[5]

This is associated with the relative optical throughputs of an interferometer and an "equivalent" dispersion spectrometer assuming the collection optics of the grating spectrometer and the interferometer have similar **f**-numbers. The **f**-number (f/#) denotes the ratio of the equivalent focal length of a lens/mirror aperture of its entrance aperture. A parameter called the Étendue is used to compare the optical efficiency of instruments quantitatively. It is the product of the half angle of the cone of light collected and the area of the entrance aperture.

$$\text{Étendue} = \tan^{-1}(\tfrac{1}{2}\,\mathbf{f})\,.\,\text{Area}$$

In a conventional spectrometer, radiation is focused onto a slit whose image is observed by the detector. The resolution is increased by narrowing the slit width, hence the energy throughput is reduced. However, the entrance of an interferometer is called a Jacquinot (J) stop, a relatively large circular aperture. In a comparison of commercial analytical interferometric and diffraction spectrometers the J stop has an area approximately 50-70 times larger which leads to a higher energy throughput in an

interferometer than in a dispersive spectrometer for the same resolution. Thus the optical throughput and hence the signal to noise ratio in the spectrograph derived from of an interferometer is far superior to that of a conventional grating spectrometer. This is known as the Jacquinot advantage.

The Felgett Advantage[6]

In a grating instrument only a single wavelength of radiation falls on the detector at one time, the rest is wasted. In a spectrograph the entire spectrum, or at least a large part of it, is recorded continuously. For a given acquisition time, a spectrograph will therefore detect far more photons and have a much higher signal-to-noise ratio. This is known as the multiplex advantage.

An interferometer possesses a similar advantage termed the Felgett advantage. In an interferometric instrument, although the optical delay is scanned sequentially, each delay contains information about all wavelengths entering the instrument and hence the Fourier Transformation samples the full interferogram. However to obtain an interferogram, the moving mirror must scan for a finite time (usually a few seconds) to record a spectrum, thus the Felgett advantage is not as great as the multiplex advantage.

The Connes Advantage[7]

When spectra are averaged, an improvement in the signal to noise ratio is observed i.e. signal/ noise ratio improves with the √number of scans. This relies on the fact that the spectra can be exactly superimposed. For a grating instrument, mechanical wear errors may cause significant spectral displacement errors which can lead to band shapes being distorted. As a result, the signal-to-noise ratio will fail to improve. This has since been solved with the advent of holographic gratings. Interferometers have an advantage whereby the abscissa scale for the spectrum is generated from the HeNe laser, the wavelength of which is invariant and known precisely. Thus, errors are reduced and spectra can be almost exactly superimposed.

3.3 Practical Vibrational Spectroscopy

3.3.1 Infrared Spectroscopy

Sources for infrared radiation spectroscopy are usually filaments which are maintained at red- or white-heat by an electric current. Two common sources are the Nernst filament which consists of rare earth oxides and the somewhat thicker "globar" filament comprising of a rod of carborundum. The beamsplitter is made from a thin layer of germanium sandwiched between potassium bromide plates. Detection of the radiation is usually achieved with either a deuterated triglycine sulphate (DTGS) or a mercury cadmium telluride (MCT) detector. The latter needs can be cooled to cryogenic temperatures with liquid nitrogen to yield greater sensitivity for some experiments.

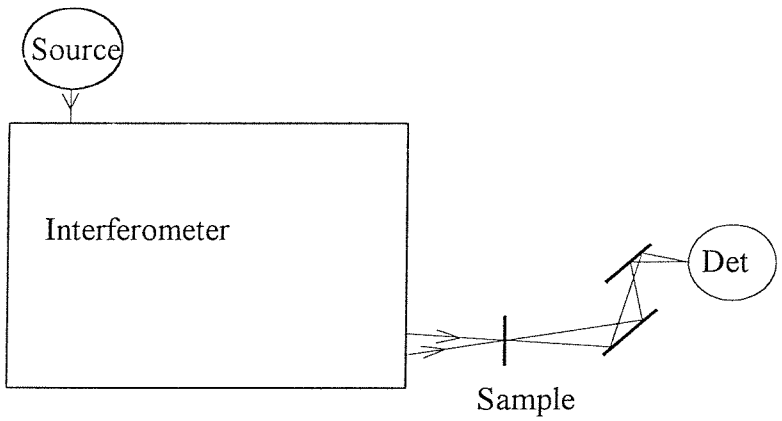

Figure 3.8: A standard infrared experimental arrangement

3.3.2 F.T. Raman spectroscopy

The standard Fourier transform Raman spectrometer is essentially a modified FT-IR instrument[8]. The main difference is that there is no direct radiation source. Instead, a laser illuminates the sample and collection optics are used to collect the Raman scattered light. This produces an image at the J-stop.

The excitation source for a NIR FT-Raman instrument is usually a neodymium yttrium aluminium garnet (Nd^{3+}:YAG) laser, which excites at 1064 nm (9398.5 cm^{-1}). Optical set-ups operating in this spectral region can use relatively inexpensive conventional glass or quartz components. The usual infrared potassium bromide beamsplitter is frequently replaced with a quartz one, offering a higher transmission for light scattered in the range 9400 - 5400 cm^{-1}. Scattered light can be collected at any angle to the incident laser beam but by far most common is the 180° (backscattering) geometry. A diagrams illustrating the geometry is shown in Chapter Four.

The scattered light from the sample passes through a Rayleigh line rejection filter which attenuates the elastically scattered component by a factor of 10^8 before entering the interferometer. The Rayleigh line intensity is then comparable to the strongest Raman scatter. The HeNe beam is also filtered out before reaching the detector.

Operating at a higher wavenumber range, an FT-Raman spectrometer also requires a different detector than an infrared instrument. In the PE 1700 series an Indium Gallium Arsenide detector is used although the germanium detector is popular with other manufacturers. These are both photodiode detectors. The InGaAs detector operates to slightly longer wavelengths (and hence higher shifts) than the germanium, but is noisier.

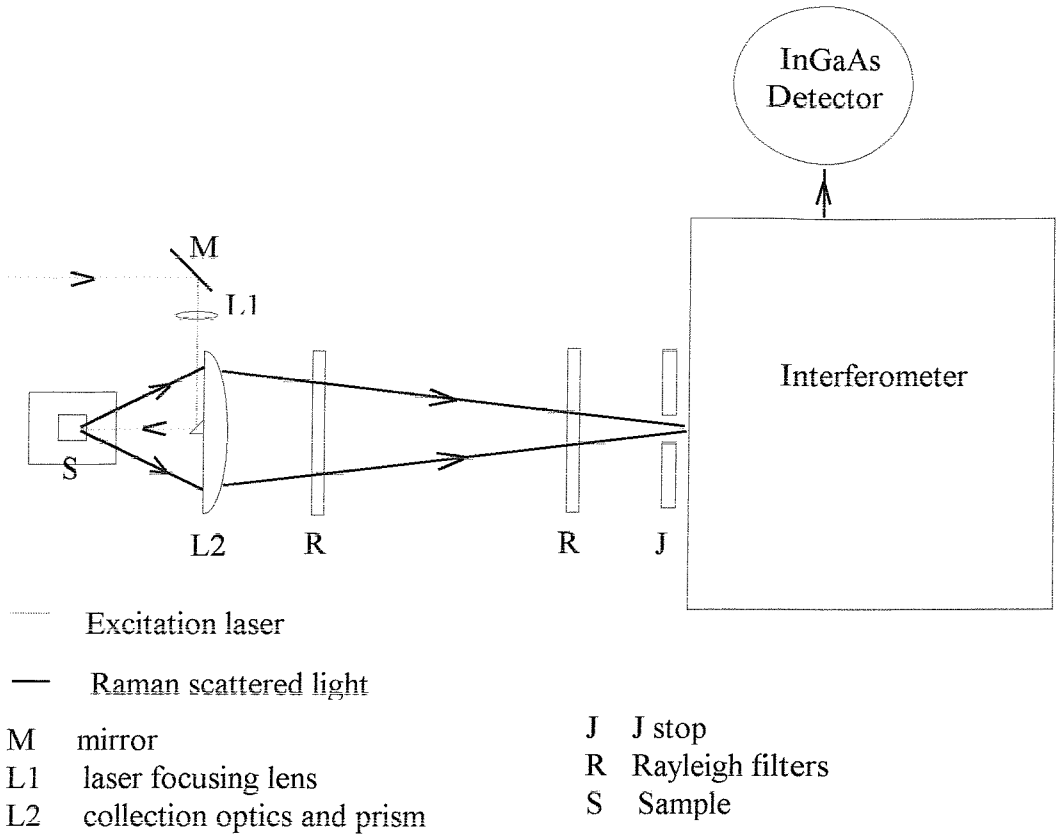

Figure 3.9: Schematic diagram of the PE 1720 FT Raman layout

3.4 The Fluorescence problem with Raman spectroscopy

In Raman spectroscopy, the term *fluorescence* is often used to describe a variety of phenomena which cause the baseline of the spectrum to be non-zero. Fluorescence in a sample can appear from degradation products and impurities/additives as well as the bulk materials, and are almost always more intense than Raman emission.

If fluorescence occurs with conventional visible laser sources, and it is not an intrinsic property of the analyte molecule, it can in some cases be 'bleached-out' (reduced), simply by continuously irradiating the sample area to be analysed with the excitation laser for periods from a few minutes to overnight[9]. With visible laser and NIR sources colour has to be considered, to avoid high energy absorption burning-up the sample, or

electronic absorption band interactions, which may lead to selective intensity enhancements of moieties due to resonance effects.

The initial reason for the development of FT-Raman techniques was to overcome the persistent fluorescent problem in Raman spectroscopy. By exciting in the NIR (most typically 1.064 μm) with a laser wavelength well below the threshold for excitation of the fluorescing electronic state, the fluorescence problems have frequently been circumvented. However, band shape distortions or relative band intensity variations can occur with samples which have their own NIR absorption bands close to or at the laser wavelength or Raman emission wavelengths, e.g. water at ~1.4 μm. There are also still some classes of samples which show unacceptable fluorescence background signals when excited with 1.064 μm radiation e.g. Heat treated Polyethyleneethylketone (PEEK), blue and green based samples based on copper phthalocynine (CuPc)[10].

Chase and Asselin[11] and others[12,13] have shown that operation further in to the NIR (at 1.339 μm) offers additional possibilities for fluorescence minimisation. Thus, the question presents itself as to whether FT Raman spectroscopy should employ a Nd:YAG unit lasing at 1.064 μm or at 1.3 μm. This shall be discussed in the next chapter.

3.5 References

1. J.M.Hollas; Modern Spectroscopy (1987) Wiley 121.
2. A.A. Michelson; Phil. Mag. (5) 31, (1891) 256.
3. R.P.Wayne; Chemistry in Britain May (1987) 440.
4. J.W.Cooley and J.W. Tukey; Mathematics of Computation 19, (1966) 297.
5. P.Jacquinot; Jour. Op. Soc. Am. 44, (1954) 761.
6. P.J.Felgett; Jour. Phys. Radium 19 (1958) 187.
7. J.Connes and P.Connes; Jour. Op. Soc. Am. 56 (1966) 896.
8. D.BChase and T.Hirschfeld; Appl. Spectrosc., 40, (1986) 133.
9. P.J.Hendra, C.Jones and G.Warnes, "Fourier Transform Raman Spectroscopy", Ellis Horwood Ltd., 1991.
10. J.M.Chalmers and G.Dent, "Industrial Analysis with Vibrational Spectroscopy", Editor N.W.Barnett,1997.
11. K.J.Asselin and B.Chase, Appl. Spectroc. 48, (1994) 699.
12. N.Everall, Jour.Raman Spectrosc. (1994), 25 (10).
13. M. Claybourn, J. Raman Spectrosc. (1994), 25(1), 123-9

4.Chapter Four: FT-Raman Spectroscopy at 1.319 Micrometers

The last fifteen years or so has witnessed a significant growth in the utility of Raman measurements in academic, industrial and governmental laboratories. Many improvements in the basic spectroscopic instrumentation have allowed applications to be made to areas such as polymers, biological systems as well as process measurements. Advances with new technology such as holographic notch filters, charged couple-device detectors and diode pumped lasers allow Raman instruments today offering unparalleled sensitivity and ease of use. These benefits have served to establish new areas where Raman spectroscopy can be applied, while also making the use of Raman data as effortless as the comparable technique of infrared spectroscopy.

The foremost choice of laser source for FT-Raman has been the continuous wave neodymium:YAG (Nd:YAG) solid state laser operating at 1.064 μm. The Nd:YAG has proved highly successful as an excitation source since its introduction in 1986 [1] to the application of near-infrared (NIR) FT Raman studies. The laser is relatively cheap and requires minimal maintenance compared with the argon and krypton sources of similar power operating in the visible. The fundamental advantage of NIR sources over those in the visible is however the decreased fluorescence and the subsequent increase in successful recording of Raman spectra.

In contrast there has been a great deal less work carried out utilising the other emission lines of the Nd:YAG laser as a Raman excitation source. Chase and Asselin[2] pioneered work in this area using the 1.339 μm lasing emission from the Nd:YAG. They showed how some classes of compounds with excessive fluorescent background signals at 1.064 μm gave a significant reduction in fluorescence when excited at 1.339 μm. It was further demonstrated that the sensitivity of the instrument used was comparable to that of conventional FT-Raman instruments and that excellent anti-Stokes spectra could be

recorded. Furukawa *et al*[3] recently carried out studies with the 1.319 μm laser line and observed FT-Raman spectra of lightly doped *trans*-polyacetylene for the first time.

Other than these publications little or no other work has been undertaken with either of the excitation lines at 1.339 or 1.319 μm. A study was thus conducted on FT Raman spectroscopy at 1.3 μm in order to fully access the level of sensitivity and the possible potential applications for operation at this wavelength.

4.1 System Characteristics:

4.1.1 The laser source

Excitation at 1.319 μm was achieved with a large frame water cooled Nd^{3+}:YAG Spectron laser . It comprised of two main components, the head and the power supply, connected by an umbilical cable. The laser was essentially a conventional commercial 1.064 μm laser but modified by replacing the high reflection optics to shift the high gain wavelength region to 1.319 μm. The lasing state is actually a doublet with a separation of ~100 cm^{-1}. The manufacturers (Spectron laser systems) were able to produce a single lasing state by inserting an etalon into the laser cavity. By changing the angle of the etalon either component of the lasing doublet could be selected. However, the manufacturers had difficulty in achieving a stable output at the 1.339 μm component of this doublet and thus the laser was supplied operating only at 1.319 μm. Other spurious emissions from the 1.319 μm laser included features at 1.339 μm (very strong), 1.064 μm (very strong) and around 0.9 μm (strong and broad).

The principle problem with the laser apart from the strong emissions (which were subsequently addressed with appropriate filtering) was associated with the power stability. The laser produced a stable maximum output power of 1.3 W. However, at output powers <500 mW the laser was found to be quite unstable, fluctuating at times by ± 5 % of the

selected output power. By operating at the maximum emission level and using a Melles Griot attenuator a stable output power was produced and controlled to provide that desired for the particular Raman application.

4.1.2 Laser filters: Rayleigh rejection filters and bandpass filters.

Each excitation laser wavelength requires a set of Rayleigh rejection filters to block the laser wavelength and transmit the Raman scatter efficiently. A laser bandpass filter (Kaiser Optical Systems) operating at 1.319 μm was used to filter the laser radiation. The filter blocks the white light emitted by the high-pressure xenon lamp which powers the laser and any other spurious laser emissions. Rayleigh line filtering was achieved with three Supernotch ® filters (Kaiser Optical Systems) optimised for maximum attenuation at 1.319 μm. These filters reflect the radiation at the laser wavelength and transmit the Raman scatter

Since the early 1990s holographic notch filters have become the choice for laser rejection filters in FT-Raman systems, replacing various interference filter arrangements. These filters have a high reflectivity (>99.99%, equivalent to an optical density of >4) to the laser line and steep band edges, which provides effective rejection of Rayleigh scattering in FT and other Raman systems[4]. Their high transmission (>80%) allows far greater throughput than triple monochromator Raman systems, however current technology limits the observation of Raman shifts to >50 Δcm^{-1}.

Figure 4.1 shows the transmission spectrum of the Holographic Supernotch® filter and laser bandpass filter for the 1.319 μm set-up. The filters are quite well matched to the laser wavelength with the notch centered at 1.319 μm. Filters change their characteristics when tilted with respect to the optical axis[5]; the effect of this in relation to the 1.319 μm Supernotch filters is shown in Figure 4.2. When the tilt angle was ~10°, the attenuation at the radiation at the laser wavelength was reduced but the shift towards higher wavelengths made it possible to filter a subsequent strong laser emission at 1.339 μm.

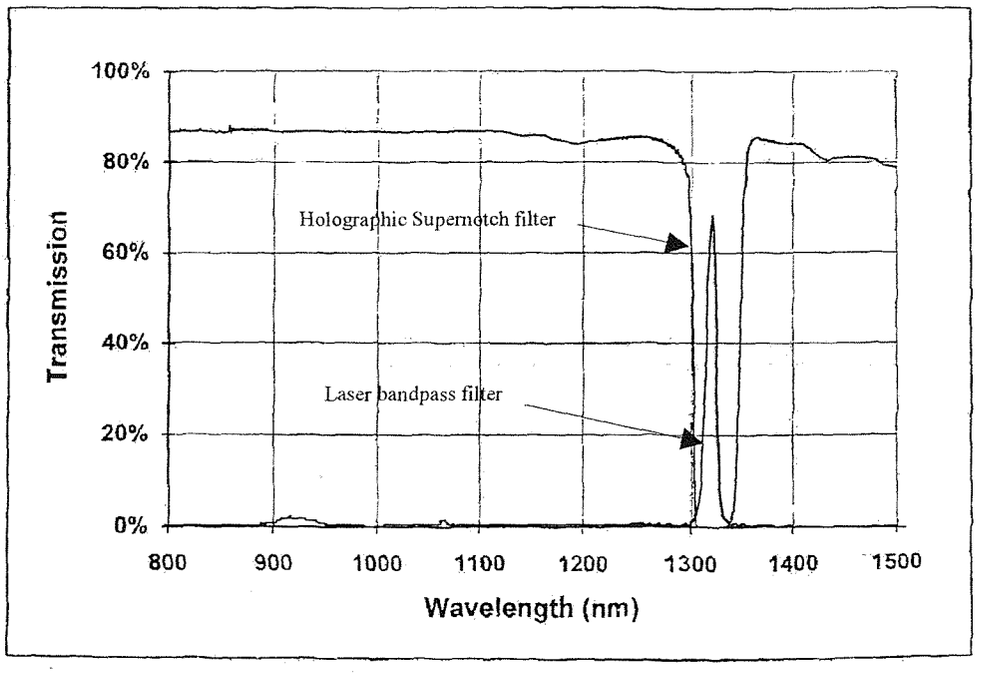

Figure 4.1: Transmission spectrum of the 1.319 μm Holographic Supernotch® filter and laser bandpass filter from Kaiser Optical Systems (USA).

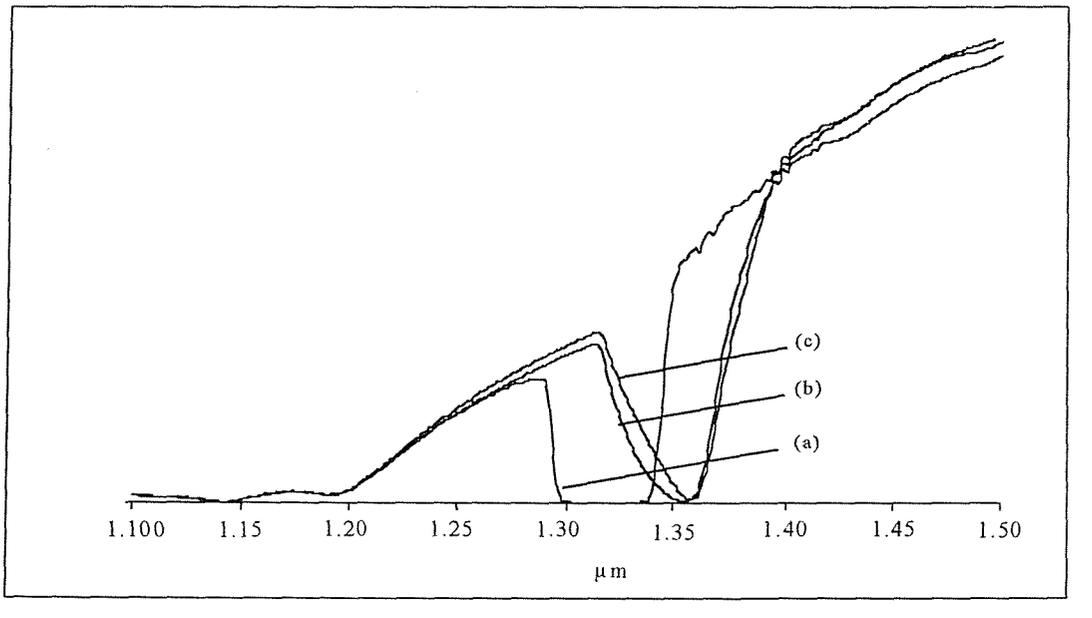

Figure 4.2: The transmission characteristics of the 1.319 μm Holographic Supernotch filter when tilted with respect to the optical axis at (a) 0°, (b) 10° and (c) 15°.

4.2 The design of a NIR FT-Raman instrument to operate at 1.319 Micrometers

The base spectrometer used in this work was a Perkin-Elmer 1720 FT Raman spectrometer. A schematic showing the layout of this instrument used for operation at 1.319 μm is shown in Figure 3. The laser light entered the front end beam steering compartment and was reflected off 2 fold mirrors, M_1 & M_2 and through the laser-focusing lens L_1. It then passed through the 1.319 μm laser bandpass filter, F_1, reflected off the prism P_1 and then onto the sample*. The illumination patch at the sample was ~ 0.5 mm in diameter.

Reflected and scattered light was then collected by a lens, L_2 and focussed through filters at the F_2 position onto the Jacquinot stop J_1. The filtered radiation passed through the interferometer and on through to the infrared sample position where it formed an image at a virtual Jacquinot stop J_2. After passing through J_2, the beam was filtered from residual excitation and Rayleigh scattered light with the use of two more filters identical to F_2 were positioned in the infrared sample compartment area. F_2, F_3 and F_4 were three Supernotch® filters optimised for maximum attenuation at 1.319 μm. The radiation then passed into the main detector compartment where it was focussed onto an InGaAs detector D_1. Initial coarse alignment of the set up was achieved with a white light source and then optimised with samples of crystalline anthracene or calcium tungstate.

The laser bandpass filter was however ineffective in totally attenuating the strong emissions at 1.339 μm and 1.064 μm. Since noise is proportional to the square root of signal bandwidth[5] these emissions reduced the overall sensitivity and performance of the instrument. A standard 1.064 μm notch filter was inserted at the F_2 position and filter F_4 was angled slightly (~10°) with respect to the optical axis inside the infrared sample compartment area. This combination successfully removed these undesired signals.

* Both of the fold mirrors (M_1 & M_2) and the prism (P) from the Perkin-Elmer 1720 Raman spectrometer were performance coated for operation at the standard 1.064 μm wavelength. These optics were replaced with silver mirrors and an uncoated plane glass prism (optics purchased from Comar Instruments).

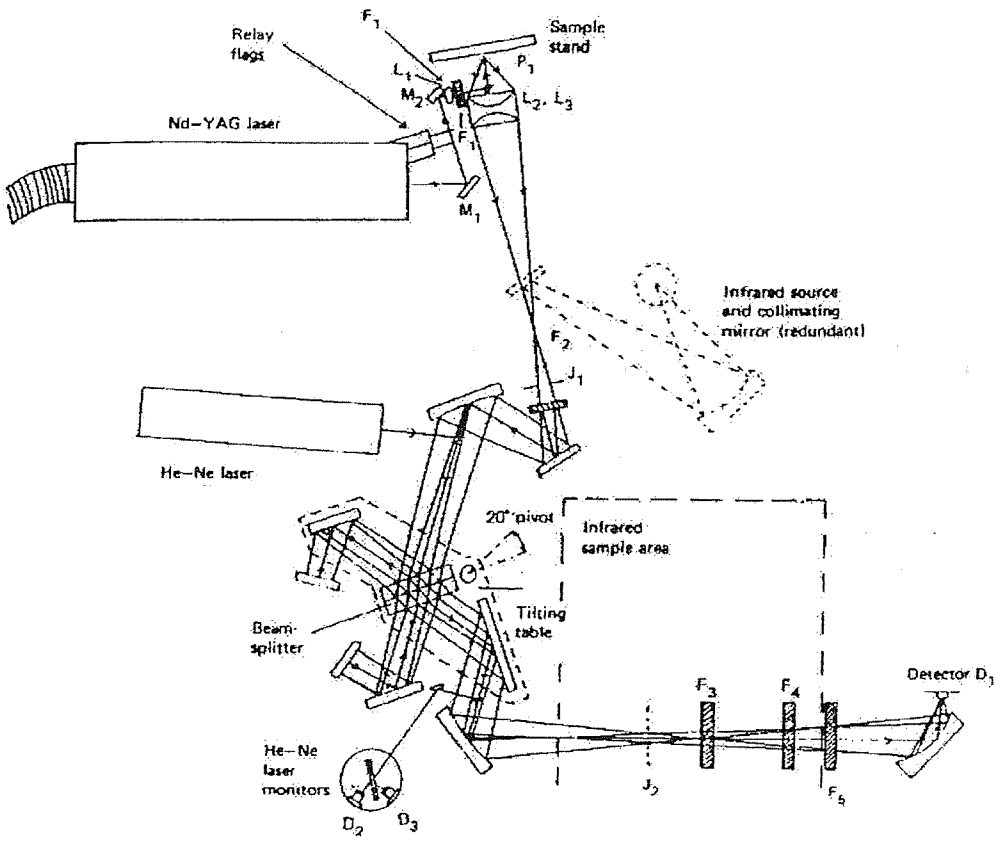

Figure 4.3: A complete optical design of the 1720 FT Raman spectrometer used for operation at 1.319 μm.

The notch filters were positioned at points in the instrument where the beam was small enough to fit through their limited aperature, i.e. J-stop entrance and the imaginary position of the exit J-stop. In general, three 1.319 μm notch filters were employed which completely removed the Rayleigh line in even the strongest scattering samples. However, when the laser frequency was required for calibration purposes one of the filters in the exit aperature was removed.

4.2.1 Instrument response function:

The light that enters a FT-Raman spectrometer passes through, and is reflected by, a large number of optical components. Each optical component possesses a specific optical response that is wavelength dependent. Light passing through the instrument is thus modified by a complex relation which depends on the transmission and reflection characteristics of the optical components of the spectrometer system as well as the responsivity of the detector used. A Raman spectrum displayed on an instrument is not a true representation of the material under examination, but essentially an optical composite of the scattered radiation entering the interferometer and the sensitivity profile of the instrument. Particular regions of the spectrum are attenuated due to the non-specific linear optical response of the instrument, namely at the transmission gradient (edge) of Rayleigh filters and the limit of detector responsivity.

The method of determining the instrument response is to use a blackbody source (e.g. tungsten source) of known temperature in place of the Raman sample and record the emission spectrum[6]. The blackbody source is modeled using Plank's Radiation law and emissivity calculations from the literature[7], and then point by point, divided out of the emission spectrum leaving the instrument response, I_{calc} :-

$$I_{calc}(\nu) = L(T,\nu) \cdot I_{actual}(\nu) / \psi(T,\nu) \cdot \varepsilon(T,\nu) \qquad \ldots\ldots\ldots \text{(Eqn. 4.1)}$$

where

$L(T,\nu)$ is the lamp emission spectrum ν, at temperature T,
I_{actual} is the actual instrument response function,
$\psi(T,\nu)$ is Plank's radiation law for a temperature T,
$\varepsilon(T,\nu)$ is the emissivity of tungsten as a function of wavelength and temperature.

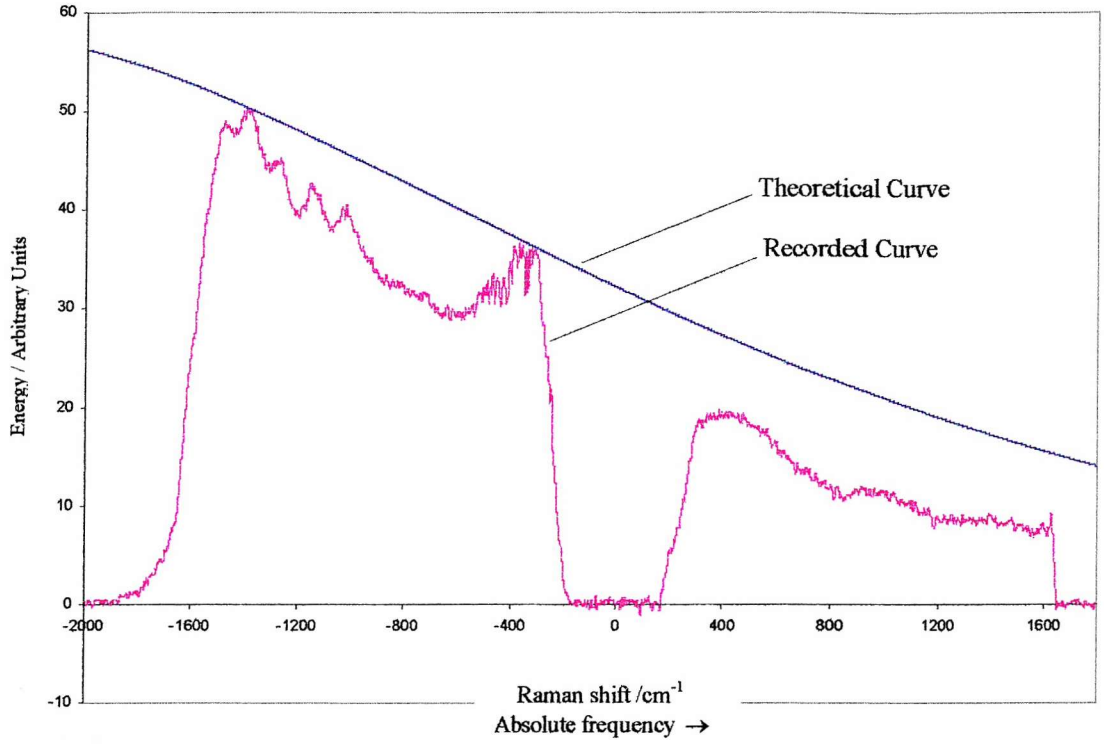

Figure 4.4: Calculated and recorded blackbody spectra superimposed. The abscissa axis is labelled in shift from the 1.319 μm line of the Nd^{3+}:YAG laser. The calculated spectrum is in counts per second. The recorded blackbody curve shows the filter characteristics (1.319 μm and 1.064 μm) and absorptions due to atmospheric water vapour.

This correction curve containing the instrument function can only be applied to Raman data where the instrument resolution (i.e. number of data points in the spectrum), the tilt angle of the Rayleigh filters, and the temperature of the detector are at the same values as the experimentally determined correction curve. Although the accuracy of the technique is probably only in the region of 5-10% [8], it provides invaluable information to the spectroscopist when comparing data from different wavelengths of excitation and also when using different types of instruments.

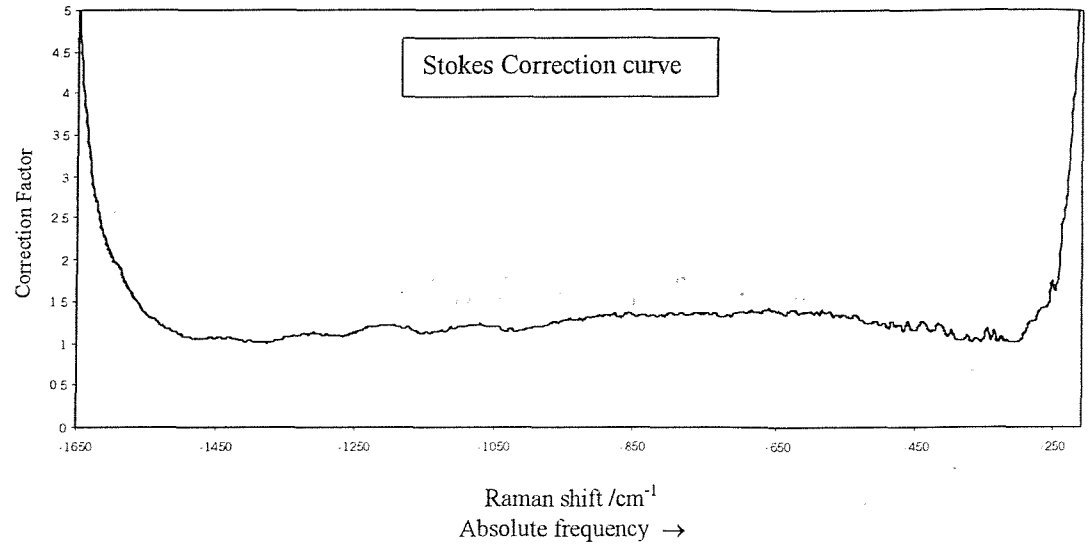

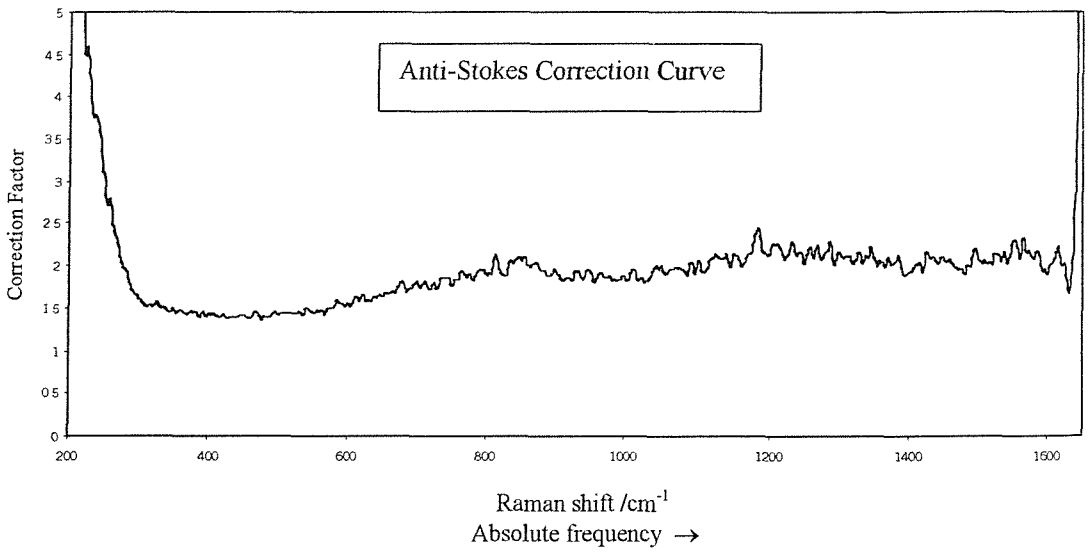

Figure 4.5: The correction curves for the 1.319μm spectra obtained by dividing the theoretical blackbody curve by the recorded one shown in figure 4.4. Where detector sensitivity is low (less than –1650 cm^{-1} Stokes shift) and the filters are not transmissive (-300 to 300 and beyond 1650 cm^{-1} Anti-Stokes shift) the correction factor is very high and these regions of the corrected spectra are ignored.

It is clear from Figure 4.5 that the Stokes shift region will be limited to a range ~1800 cm^{-1} (7580 to 5780 cm^{-1}, absolute frequency). The instrument/detector response is at a maximum within this range. Subsequent FT Raman spectra are corrected for the instrument response by multiplying the regions of interest by the appropriate correction curve.

4.2.2 Signal to noise performance:

The signal to noise ratio (SNR) of all 1.064 μm Perkin Elmer Raman spectrometers are conventionally measured using the 1000 cm^{-1} band of barium sulphate (Aldrich 99.999% pure)[†]. The test conditions were set at 1 scan, 200 mW laser power, Normal apodization function and at 4 cm^{-1} nominal spectral resolution. All Raman spectra were normalised to an instrument response function created with a backbody source. A number of factors must firstly be considered before the comparison of signal to noise ratios at 1.064 μm and 1.319 μm can be made:

(i) *ν^4 Raman scattering term* : According to classical theory[9] the scattering efficiency is a function of the absolute wavenumber ν^4 and so comparing 1.064 μm with 1.319 μm excitation sources one would expect a decrease in signal level for the sulphate band of approximately 2.4 fold.

(ii) *Sample preparation and absorption* : Raman intensities change with particle size for excitation at 1.064 μm as demonstrated by Hendra and Pellow-Jarmen[10] and references contained therein. A master sample was therefore used to record all SNR data to avoid effects due to sample inhomogeneity. The Raman signal also varies with excitation wavelength

[†] The best procedure depends upon the repeatability of the $BaSO_4$ test specimens and this has proved to be a severe limitation. Recently, Perkin-Elmer have adopted a diamond disc as their performance standard.

due to wavelength dependant absorption. The NIR absorption spectrum[8] however shows the range between 10,000 cm^{-1} and 6000 cm^{-1} free from obvious absorptions which would have a significant effect on the Raman intensity.

(iii) *Number of photons per milliwatt*: The energy per photon is inversely proportional to wavelength hence the number of laser excitation photons per milliwatt is proportional to wavelength. Since each spectrum was recorded with the same laser power, the ν^4 term was modified to ν^3 to take this into account. This therefore yields a modified decrease in signal level to approximately 2.1 for the sulphate band when comparing the 1.064 μm and 1.319 μm excitation sources.

(iv) *Raman scattering cross-section:* This is the classical representation of the transition probability and is assumed to be independent of the two excitation wavelengths given: (a) there are no absorptions near the excitation wavelengths and (b) the peak powers in the experiment are sufficiently low not to generate any features due to non-liner Raman effects.

(v) *Instrument response function*: There is a further correction that must be considered relating to the instrument/detector sensitivity. The InGaAs detector has a noise equivalent power* (NEP) value of 7 fW $Hz^{-½}$ (according to the manufacturer[11]), quoted at the peak wavelength of sensitivity namely 1.650 μm. The Raman Stokes shift at 1.319 μm is limited to the range <1800 cm^{-1} (~7500 to 5700 cm^{-1}, absolute frequency)

* The NEP is defined as the amount of optical signal power to give the equivalent level of intrinsic noise from the detector/preamplifier combination, i.e. a signal to noise of 1:1. NEP is expressed in units of W $Hz^{-½}$ and defined at a particular frequency and wavelength to account for wavelength dependence of the quantum efficiency (a measure of the detector's ability to convert incident photons to electrons).

but within this range the instrument/detector response is at a maximum which partially compensates for the loss due to the ν^4 factor [2].

It is therefore reasonable to compare the SNR using excitation wavelengths at 1.064 μm and 1.319 μm as this represents the most potentially significant performance difference. When all of the above factors are taken into account and combined the relative signal to noise ratio was expected to be about 2 times better at 1.064 μm.

Figure 4.6 (a) and (b) compare the actual results obtained with the Nd^{3+}:YAG lasers operating at the different wavelengths. Both sets of data were corrected for instrument response by the method described above.

The data above was typical of the peak to peak values over ten consecutive spectra. The signal to noise performances are similar to the expected values for 1.319 μm however the 1.064 μm set-up performed slightly better. The overall accuracy obtained in this result can be attributed to the high performances of both sets of Rayleigh rejection filters (holographic notch filters) coupled with the alignment of the front end optics.

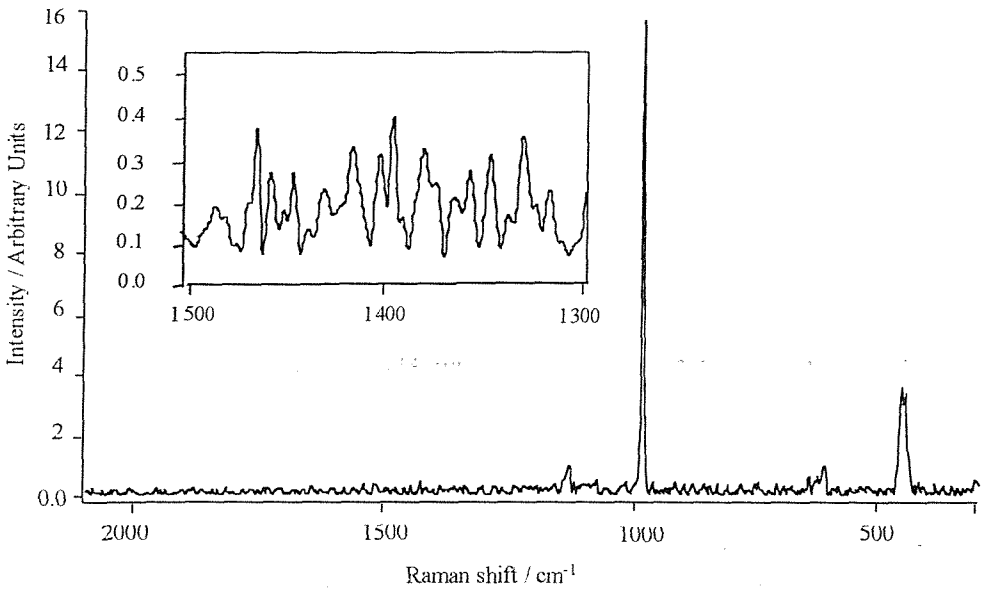

Figure 4.6 (a): Raman spectrum of BaSO4: 200 mW, Scan speed 0.2 cm s^{-1}, 1 scan, 4 cm^{-1} resolution, 1.319 μm; SNR ≅ 64 : 1.

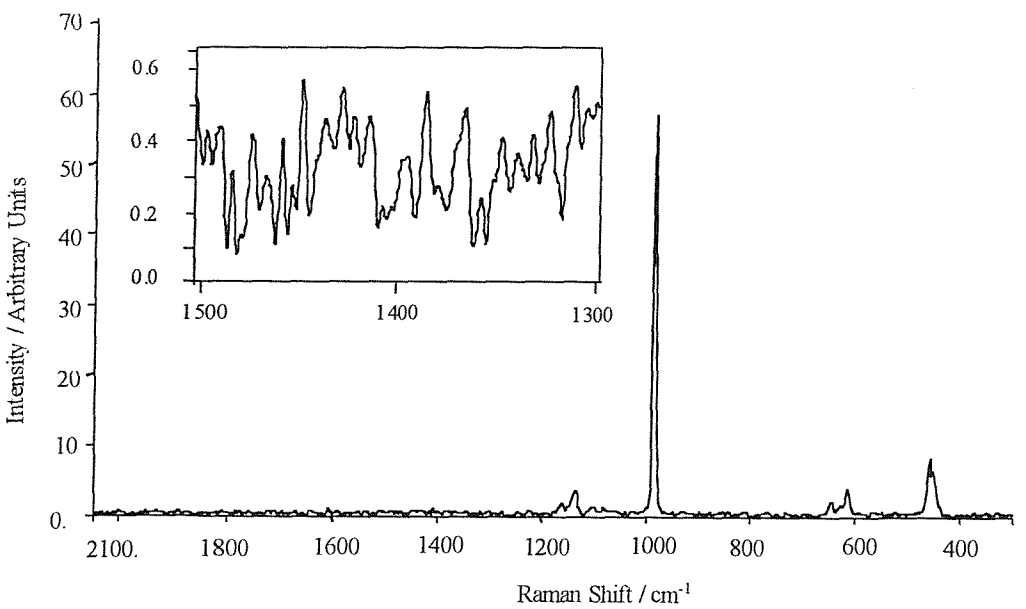

Figure 4.6(b): Raman spectrum of BaSO4: 200 mW, Scan speed 0.2 cm s^{-1}, 1 scan, 4 cm^{-1} resolution, 1.064 μm; SNR ≅ 158 : 1.

4.3 Applications and Selected Results

4.3.1 Use of the FT-Raman spectrum of Na_2MoO_4 to study sample heating by the 1.319 μm laser

Sample heating associated with laser FT Raman spectroscopy has always been a cause for concern[12]. The temperature of the sample may increase when it absorbs incident radiation. A number of factors contribute to the amount of heating that occurs, the extent of which has in the past proven difficult to determine. The temperature rise is dependent on both sample and experiment, being influenced by such factors as the thermal conductivity and color (ability to absorb the radiation), the length of time exposed to the laser radiation, the laser power and brightness as well as the wavelength used. A study carried out on PTFE[13] estimated a 1K temperature rise per 100 mW laser power but this is now considered as an underestimate. The general principle is that sample heating is an inherent limitation of laser Raman spectroscopy.

A later study[14] used the crystal transition of Sodium molybdate, Na_2MoO_4 at about 112 °C as a method of qualitatively assessing the heating effect from a 1.064 μm Nd:YAG laser. It was found that powers of 125 mW were sufficient to raise the sample by 40 °C, whereas powers above 375 mW were required to raise the temperature by 50 °C. The results showed the importance of sample temperature awareness and the need for alternative sampling techniques[15] to minimise the effect. Significant temperature gradients were also found to be present across the sample. For a sample temperature at 70 °C and 125 mW of laser power, it took 10 min of laser heating for all the sample to experience a temperature of 112 °C. Similarly for a sample temperature of 60 °C and 375 mW power, the corresponding time increased to 25 min.

A similar study to the above was thus carried out to ascertain the degree of sample heating from the 1.319 μm laser.

4.3.1.1 Experimental:

Standard anhydrous Na_2MoO_4, purchased from Aldich Chemicals Ltd. was used as supplied for all the studies conducted. All Raman spectra were recorded using a Perkin-Elmer 1720 FT Raman spectrometer powered by a Spectron CW Nd^{3+}:YAG laser with TEM_{oo} output at 1.319 μm as the near infrared excitation source. A solid sample of approximately 2 mm diameter and 1mm deep was heated in a Ventacon hot cell. The sample was estimated as being up to 5 °C cooler than the temperature of the hot cell; the sample faced the collection optics which mean that there was no thermal contact on the sampling face and heat could be exchanged with the cooler surroundings. A fresh sample was used for independent examination because of the non-reversible nature of the crystal transition. The sample was loaded into the hot cell and allowed to stand for ~ 15 min before spectra were recorded to ensure temperature equilibrium. All spectra were recorded using 1 cm^{-1} resolution. All spectra were uncorrected for instrument response.

Three sets of experiments were performed.

(i) Spectra were recorded at sample temperatures of 20, 40, 55 and 70 °C using 250 mW laser power and averaging 5 scans.

(ii) The sample was heated to 55 °C and the FT Raman spectrum recorded as an average of 5 and 10 scans (scanning time ~ 1.1 and 2.2 min respectively) using laser powers of 125, 250, 375 and 510 mW.

(iii) For a sample temperature of 60 °C and 125 mW laser power, the FT Raman spectrum was recorded as an average of 10, 20, 40 and 80 scans.

4.3.1.2 Results and discussion

The vibrational assignments for sodium molybdate in the two crystal forms are listed in Table 1. As mentioned above, the low temperature form exists up to a temperature of about 112 °C. The most notable change between the two spectra is in the ν_1 band and thus gives a qualitative measure of the conversion to the high temperature crystal form. Other noteworthy features include the disappearance of the weak combination bands to the high frequency side of ν_4 and ν_2 in the high temperature form.

Table 1

Band frequencies for solid Na_2MoO_4 assigned according to the tetrahedral symmetry for the relatively free molybdate ion in solution.

Form[a]	ν_1	ν_3	ν_2	ν_4
(a)	891, 896	809, 833, 843	378	302, 320, 330, 340
(b)	890	808	378	302

(a) Low temperature form; (b) high temperature form

Fig. 4.7 shows spectra recorded at four different hot cell temperatures using 250 mW laser power, 1 cm^{-1} resolution and five scans. No transition was observed at room temperature for any laser power used (up to 510 mW) in keeping with previous results obtained[14]. The sample undergoes a gradual transition as indicated by the relative reduction in the peak at 896 cm^{-1}. At 70 °C, the sample has undergone the whole crystal transition within the time for a single scan spectrum (0.4 min). This result indicated an increase in laser heating at 1.319 μm of ~ 10 °C when compared with the results obtained at 1.064 μm.

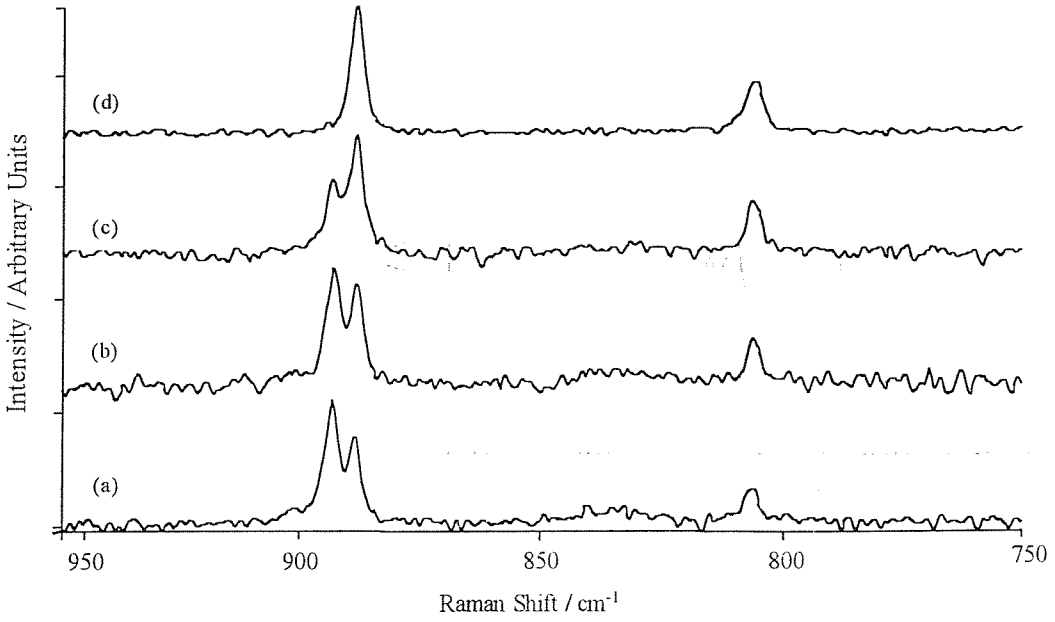

Figure 4.7: Spectra of Na_2MoO_4 recorded at different sample temperatures using a laser power of 250 mW, 1 cm^{-1} resolution and five scans: (a) 20 °C; (b) 40 °C; (c) 55 °C; and (d) 70 °C.

The results from the effect of varying the laser power are illustrated in Fig. 4.8 (A) and (B). The sample temperature was maintained at 55 °C. As expected, there was a greater sample heating effect for a given scanning period as the laser power was increased. The heating effects at 250 and 375 mW appear almost identical, again monitoring the reduction in the peak intensity at 896 cm^{-1}. Examining Fig. 4.8 (B) it can be seen that after 10 scans using 510 mW laser power almost all the sample has undergone the crystal transition indicating a sample heating increase of ~ 45 °C for the given time period. The overall trend was the same for both experiments with the onset of the transition occurring only when the laser power was greater than 375 mW.

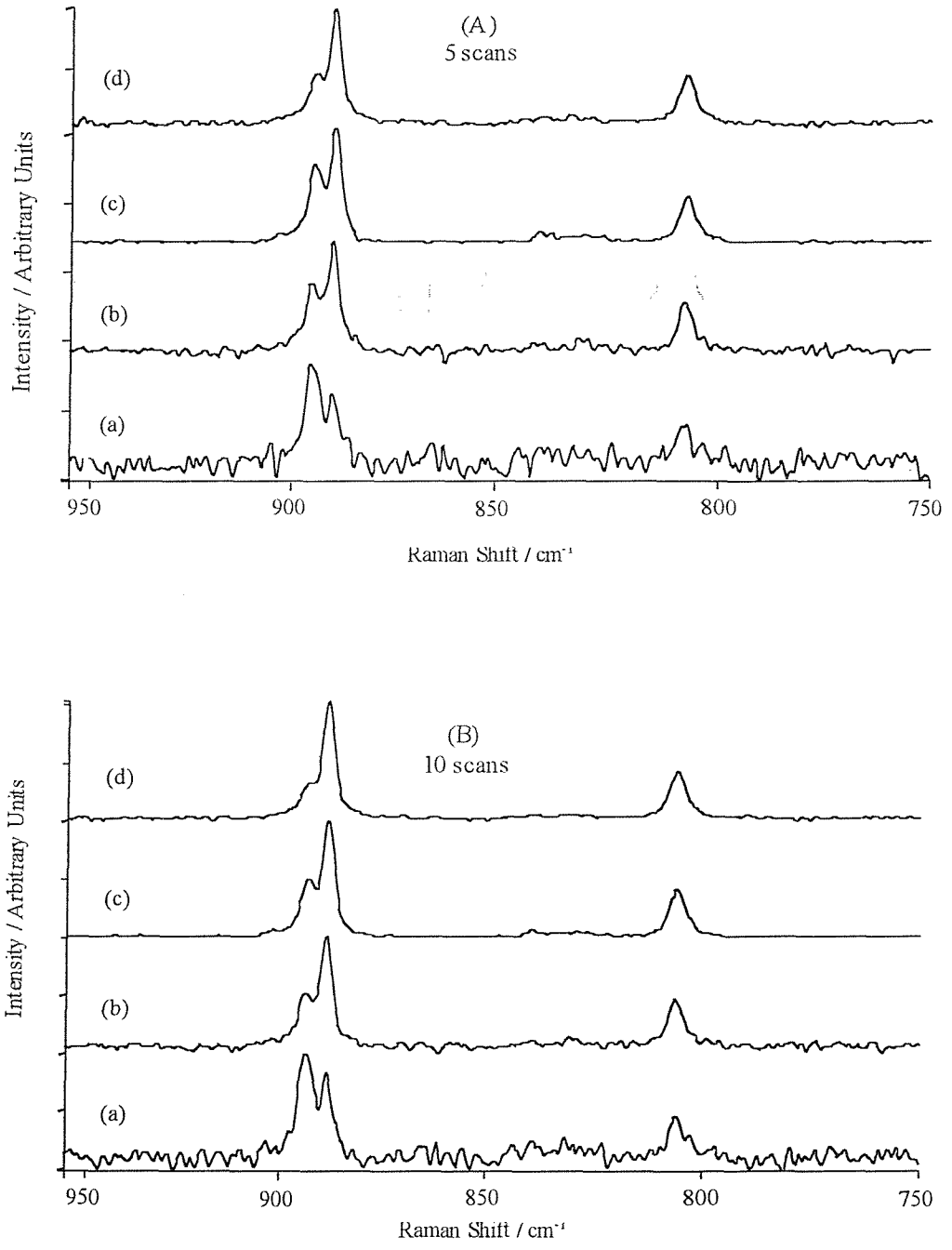

Figure 4.8 (A) and (B): Spectra of Na_2MoO_4 recorded at a sample temperature of 55 °C, 1 cm^{-1} resolution, five and ten scans respectively and using a range of laser powers: (a) 125 mW; (b) 250 mW; (c) 375 mW; and (d) 510 mW.

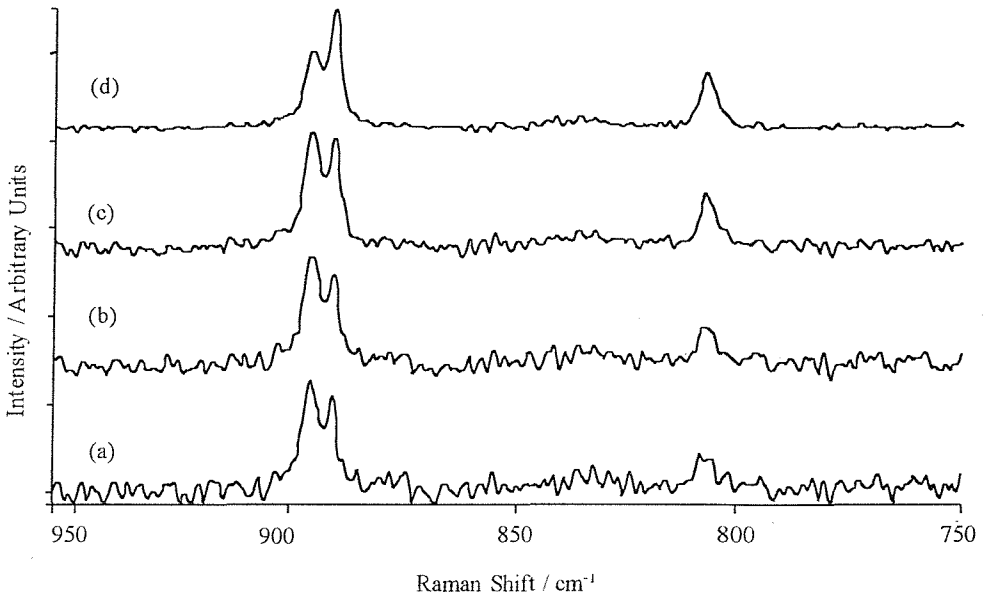

Figure 4.9: Spectra of Na_2MoO_4 recorded at a sample temperature of 60 °C, 1 cm^{-1} resolution and 125 mW laser power: (a) 10 scans; (b) 20 scans; (c) 40 scans; and (d) 80 scans.

There is an obvious temperature gradient across the sample surface (a function of the laser beam diameter and coherence together with spectrometer resolution) observed in all the results. The expectation is that the central point of the laser beam impact would undergo the greatest heating effect, with a reduction at increasing radii. The time for the laser to heat the whole sample area was also studied. Figure 4.9 shows the progress of the transition for different laser heating times at 60 °C. The result shows that the spectrum observed is dependent upon the laser illumination time. Similar to results at 1.064 μm, it took over 10 min for the sample to experience a temperature greater than 112 °C and begin undergoing the transition. The transition is however still incomplete after almost 18 min. while a comparable study at 70 °C with the 1.064 μm laser resulted in almost complete conversion for the same scanning period.

4.3.1.3 Conclusion

The objective of this study was to monitor the heating effects from the 1.319 μm Nd^{3+}:YAG laser and compare against those obtained at 1.064 μm. The study was carried maintaining the samples at lower temperatures and using lower laser powers than those from the study at 1.064 μm in efforts to observe a greater heating effect with the 1.319 μm laser. The results obtained however were in general very similar. Figure 4.7 (laser power of 250 mW, sample maintained at 70 °C) showed a slight increase in laser heating over the 1.064 μm laser, but the overall tends from the other studies showed no significant differences. The ideal study would of course be to correlate the above results against the ratio of Stokes and anti-Stokes line intensities for sample temperature measurement but unfortunately the anti-Stokes lines were indistinguishable from the noise. Nowadays, of course, with the advent of new sampling accessories (e.g. Venatcon sample rotators) the past problems in FT-Raman spectroscopy associated with laser sample heating of temperature sensitive solids are far less of a problem.

4.3.2 The Ratio of Stokes and anti-Stokes Line Intensities at 1.319 μm as a Method of Sample Temperature Measurement.

The introduction of Raman notch type filters for simultaneous Stokes and anti-Stokes FT-Raman at 1.319 μm has facilitated the established technique of measuring sample temperature where it is exposed to the laser [16,17]. As described in equation (3.16) in Chapter 3 Raman scattering efficiency depends on the fourth power of the frequency of light being scattered. Although the intensity of anti-Stokes lines are reduced by the Boltzmann factor, the frequency at which the light is scattered is higher and results in a greater scattering efficiency.

$$\left(\frac{I_{AS}}{I_S}\right) = \frac{(\upsilon_0 + \upsilon)^4}{(\upsilon_0 - \upsilon)^4} \exp\left(\frac{-hc\upsilon}{kT}\right) \qquad (4.1)$$

From equation 4.1 it is thus possible to determine the temperature at the point of sampling directly from the Raman spectrum by using the ratio of the anti-Stokes and Stokes intensities for a particular vibration and assuming a Boltzmann distribution for the levels involved (v=0 and v=1). However, as pointed out by West[15], the overall value of the technique is often meaningless because the reproducibility of the relative intensities reveals absolute errors in the temperature of ~10 K which may be greater than the sample heating effect itself.

Figure 4.10 (A) and (B) show the Stokes and anti-Stokes regions respectively of the FT Raman spectra recorded at 1.319 μm with a series of laser powers (100 mW to 400 mW). All spectra were normalised for instrument response. The band intensities at 395 cm^{-1} were measured in the Stokes and anti-Stokes regions for the different laser powers and the sample temperature was calculated. Table 2 illustrates the obtained results.

Table 4.2

Laser Power (mW)	I_{Stokes}	$I_{anti\text{-}Stokes}$	Sample Temp. (K)
100	7.676	2.048	325
200	18.364	5.122	334
300	24.751	7.094	339
400	30.626	8.974	344

The results defined a sample temperature with an accuracy of ~ 7 °C against a macroscopic temperature measured with a thermocouple in the region of the irradiated volume.

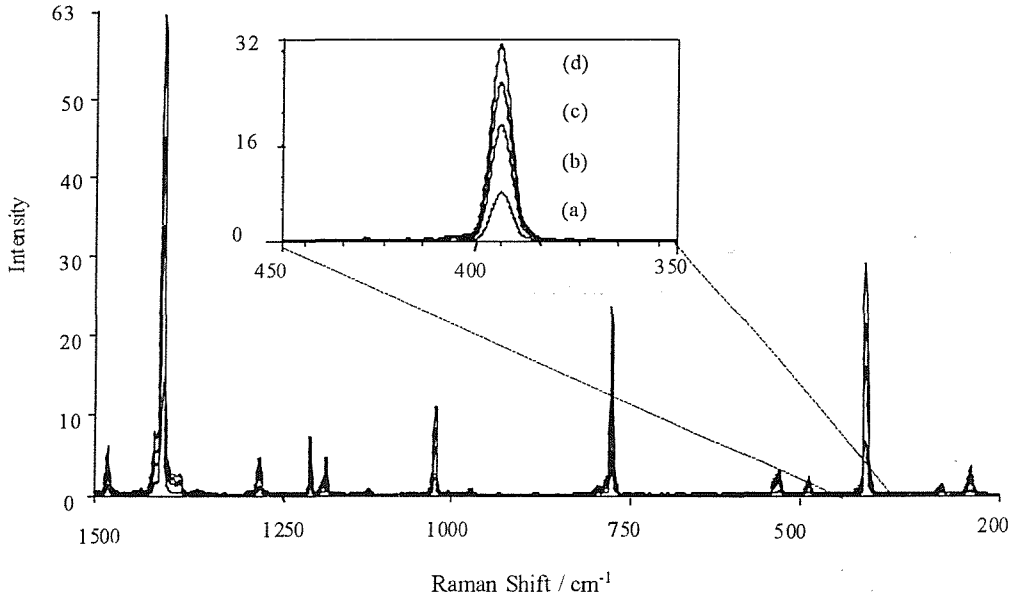

Figure 4.10 (A); Stokes region FT Raman spectra of anthracene obtained with the 1.319 μm laser at 4 cm^{-1} resolution and 10 scans with (a) 100 mW, (b) 200 mW, (c) 300 mW and (d) 400 mW.

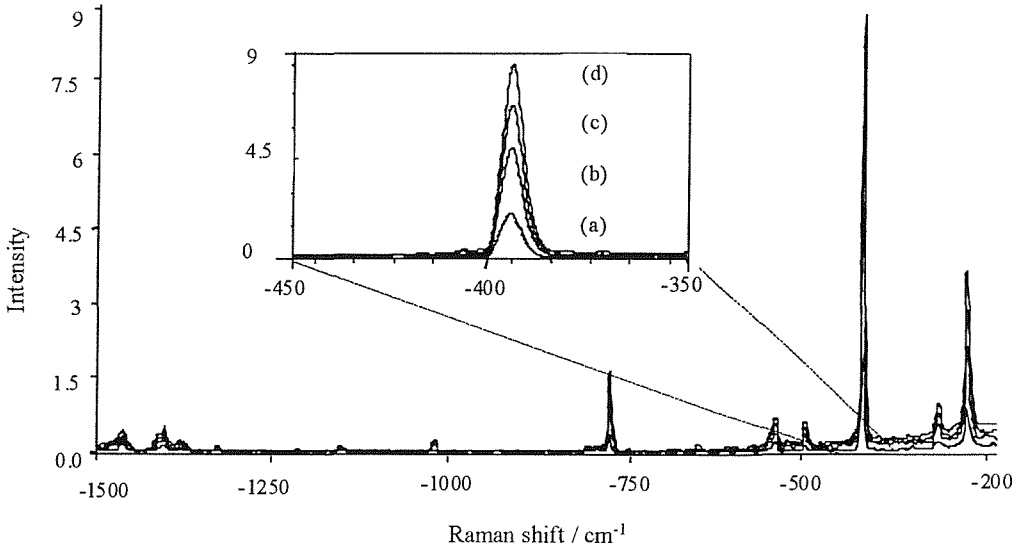

Figure 4.10 (B): Anti-Stokes region FT Raman spectra of anthracene obtained at 1.319 μm at 4 cm^{-1} resolution and 10 scans with (a) 100 mW, (b) 200 mW, (c) 300 mW and (d) 400 mW.

4.3.3 Fluorescence rejection as a function of excitation wavelength

An extensive FT Raman study covering a range of organic and inorganic samples was carried out comparing various lasing lines derived from a Ti:Sapphire-argon ion laser combination with radiation at 1.064 μm from a Nd:YAG laser by a number of workers here at Southampton [18]. Many of the samples yielded respectable spectra with low fluorescence backgrounds at 780 nm and 835 nm, however others, notably nitrile rubber and mercaptobenzoxazole, showed quite significant levels of fluorescence even at 1.064 μm. In the majority of cases a reduction in fluorescence levels was achieved as the excitation wavelength extended further into the near infrared (NIR). In conclusion, to compete with the current 1.064 μm FT systems, purely from an applications point of view, the laser would need to operate in the region of 900 nm. However, by moving the laser wavelength even further into the NIR, the question presented itself as to whether one could eliminate fluorescence altogether and hence generate a system where the range of applications might well exceed that possessed by the 1.064 μm source.

Figure 4.11 and 4.12 show the FT Raman spectra of mercaptobenzoxazole (MBO) and nitrile rubber respectively recorded at 1.319 μm. These figures also show the comparison spectra recorded by Hendra *et al* [18] at 780, 835, 920 and 1064 nm as an illustration of the fluorescence reduction which is achieved by operating at 1.319 μm. Nitrile rubber, recorded with 500 mW laser, gave a slight fluorescent background at 1.319 μm but one which was significantly less than those at the other excitation wavelengths.

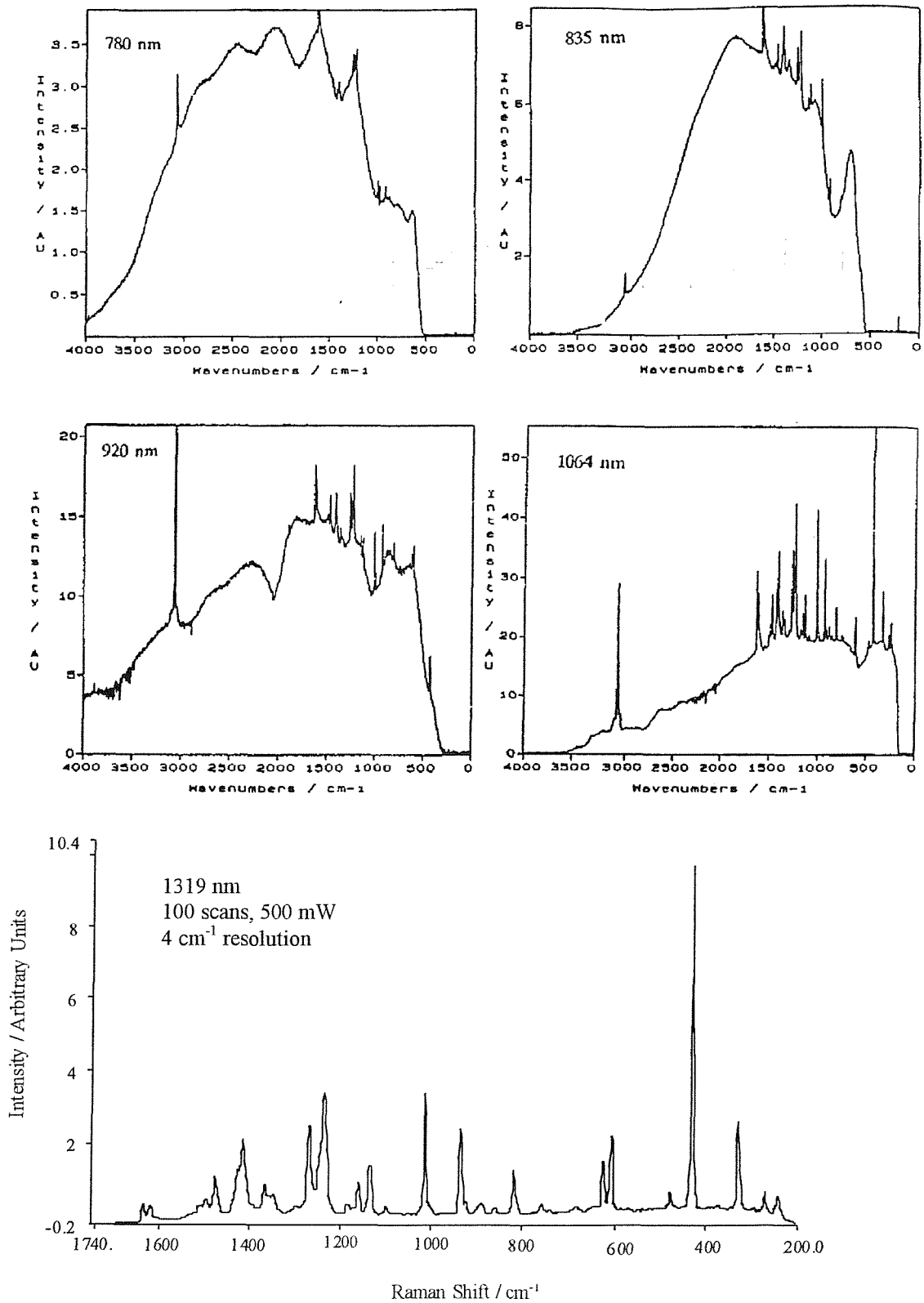

Figure 4.11: FT Raman spectra of mercaptobenzoxazole.

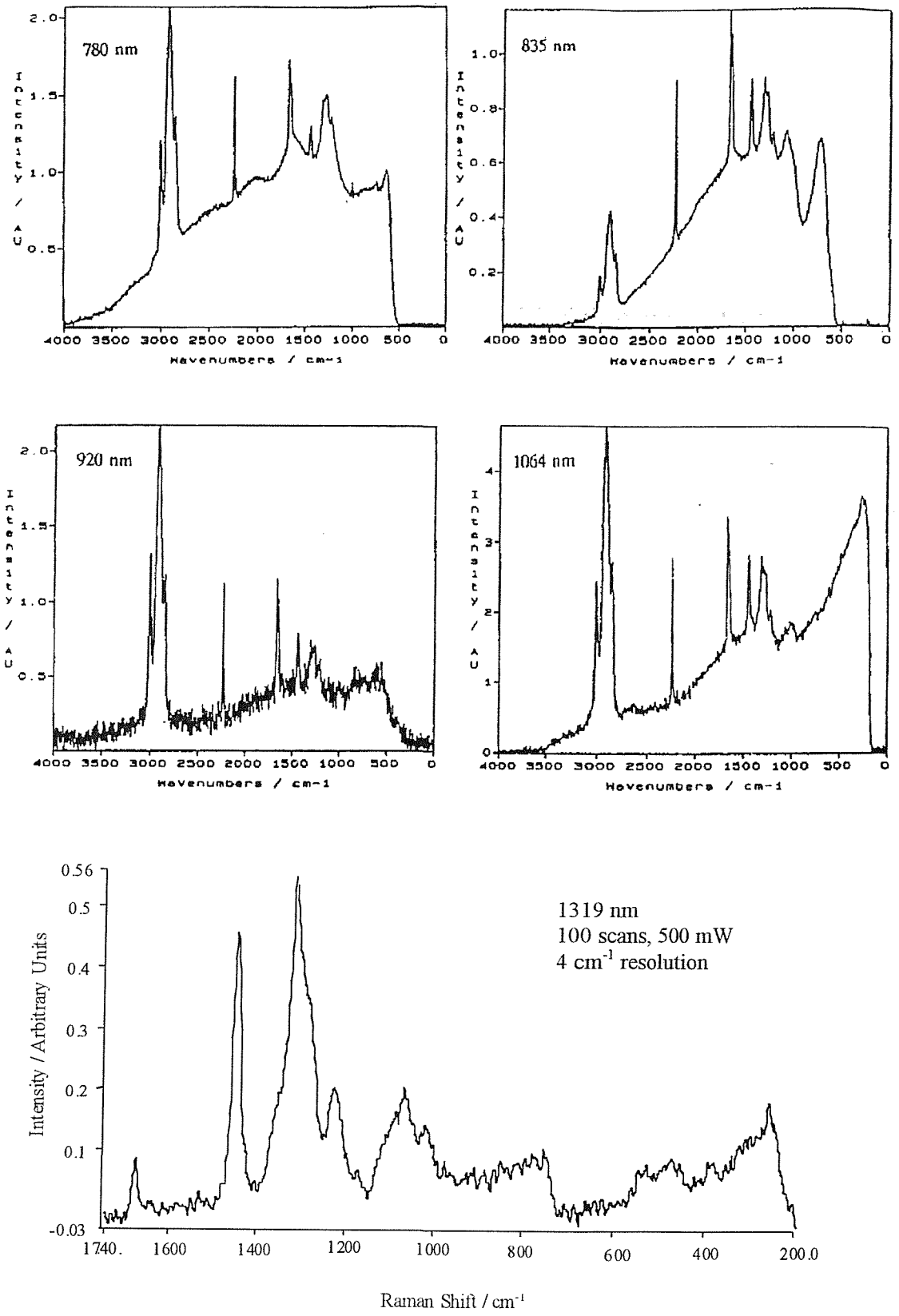

Figure 4.12: FT-Raman spectra of nitrile rubber.

A series of five dye powder samples (IUPAC description not provided for reasons of confidentiality) based on sulphonic salt type materials were obtained courtesy of Kodak Ltd. (UK). All of samples provided showed only broad fluorescence when a FT Raman spectrum was recorded with a 1.064 μm source. Three of the samples (recorded using <5 mW) showed a slight indication of spectral features arising from Raman scattering superimposed on top of a strong fluorescence signal at 1.064 μm. The other two specimens caused an instant detector overload (detector saturation[19]) at 1.064 μm even with <5 mW. Figure 4.13 shows the successful recording of these samples at 1.319 μm. Both samples in figure 4.13 were rotated with a Venatcon sample rotator to minimise any interference from thermal backgrounds. Figure 4.13 represents the fundamental advantage of working at 1.3 μm. There are still traces of a fluorescent background visible from both spectra but these reduced when lower excitation powers were used.

A number of other powder materials provided by Smith Klein Beecham (S.K.B.) and an organophosphate specimen from DERA, Porton Down gave a similar result to the examples in Figure 4.13. Publication of this data was however restricted for reasons of confidentiality.

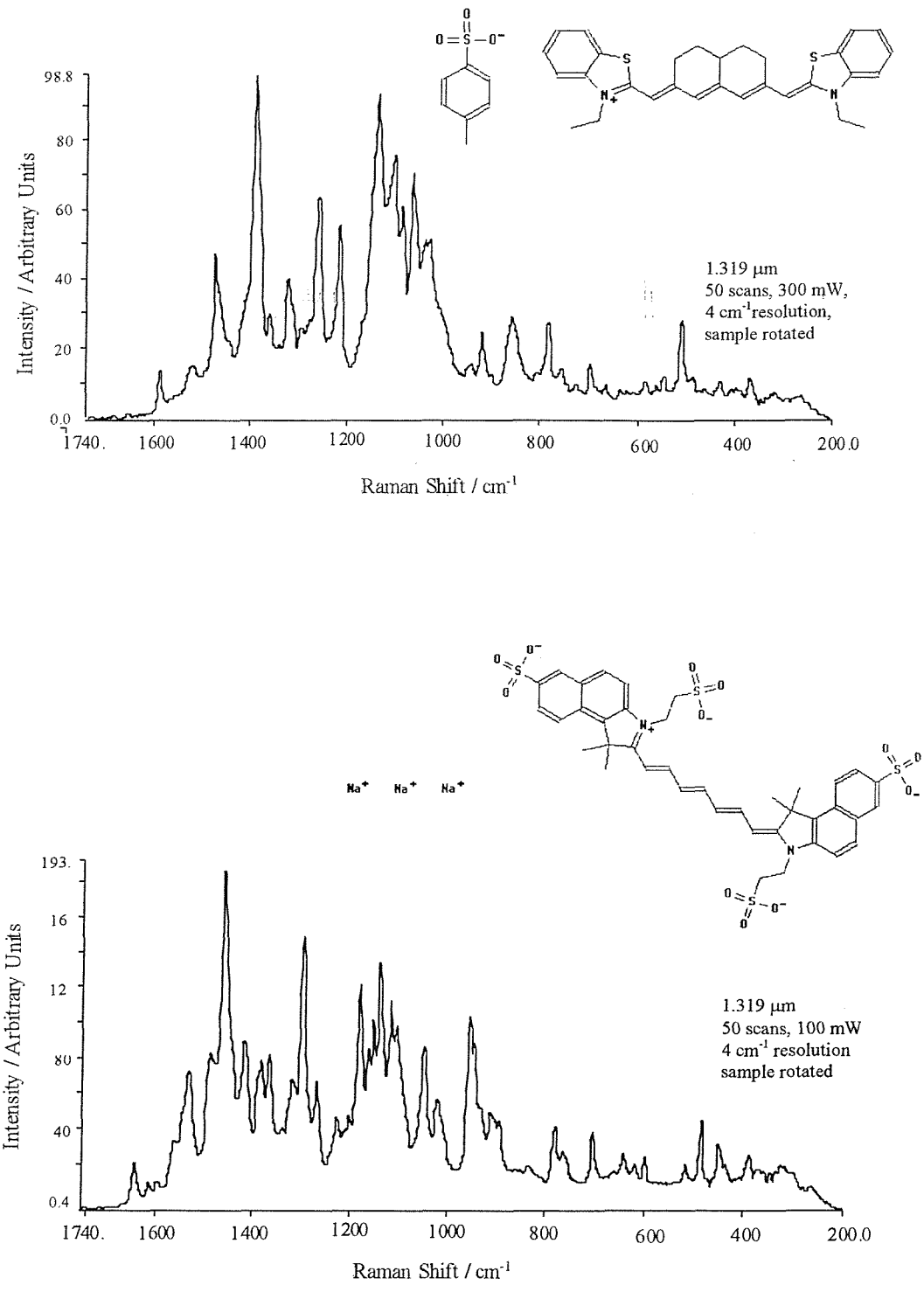

Figure 4.13: FT-Raman spectra recorded at 1.319 μm of two dye powders based on sulphonic salt type structures from Kodak Ltd. (Uncorrected data).

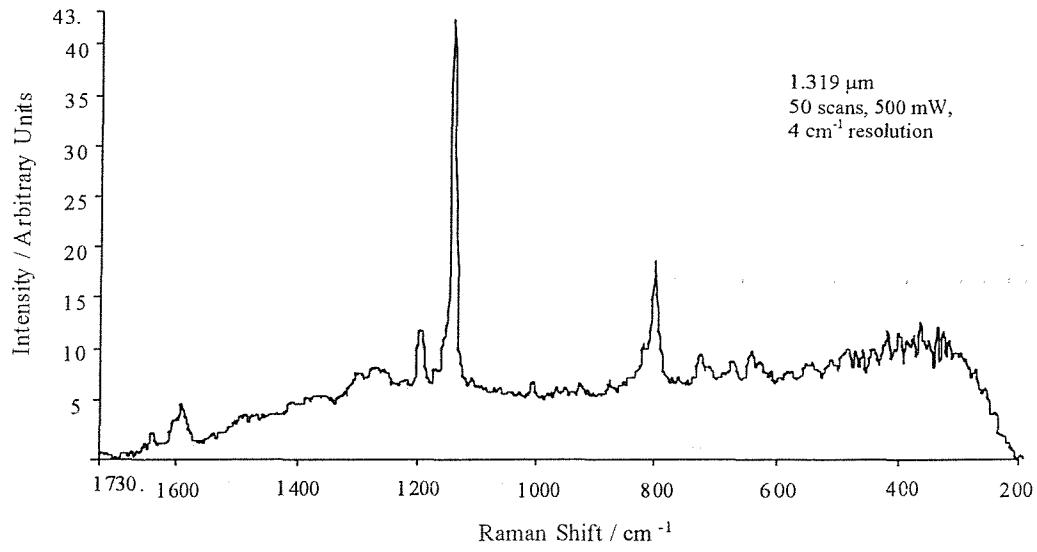

Figure 4.14. FT Raman spectra of 49% crystalline PEEK recorded at 1.319μm (Uncorrected data).

Figure 4.14 shows a spectrum of 49% crystalline PEEK at 1.319 μm. The material fluoresces strongly at 1.064 μm but also shows a significant fluorescent background at higher levels of crystallinity with the 1.319 μm laser. The fluorescence is not fundamental to the polymer but arises because the material has to be heat-treated very strongly indeed to achieve a degree of crystallinity as high as 49 %. It was necessary to use relatively high laser powers (~ 500 mW) to achieve satisfactory spectra due to the loss in sensitivity by operating at 1.3 μm. Almost identical results were achieved however at 1.064 μm recording the spectra with laser powers < 10 mW. In this example there was no significant advantage to be gained by operating further into the NIR.

4.4 Discussion

The 1.319 μm excitation source has been demonstrated with a certain degree of success. Despite the signal to noise (S:N) of the system being slightly lower than the 1.064 μm arrangement, it is more than sufficient to be regarded as a useful analytical tool taking into account the instrument used for this study. Employing a current state of the art FT-Raman instrument with a 1.319 μm laser of greater stability would undoubtedly give a much improved sensitivity resulting in S:N values typical of ~ 400:1. It must not be forgotten that the early FT-Raman pioneers yielded a wealth of applications in the literature with instruments of the same (if not less) sensitivity to that achieved in this study with the 1.319 μm laser.

The application of the source has been successful for the most part to inorganic substances that show indications of scatter superimposed over unacceptable fluorescent backgrounds at 1.064 μm. The further reduction in Raman band intensity due to the ν^4 factor can however lead to difficulties when trying to record spectra from poor scatterers. Laser induced heating through sample absorption of the laser radiation and self-absorption of Raman scatter is a particular hindrance when recording water based samples, e.g. solutions and gels.

It was suggested by Chase *et al*[2] that fluorescence at 1.064 μm is further reduced at 1.3 μm but this is probably true classical fluorescence not the real fluorescence typical of impure organic samples for example. Real fluorescence in a sample can appear from degradation products and impurities/additives as well as bulk materials. Spectra recorded from specimens of this nature (provided by S.K.B) were found to yield similar fluorescent backgrounds at both wavelengths in question.

Although inorganic chemists have found fluorescence a familiar problem when attempting Raman measurements they have also been dogged by problems associated with photodecomposition and absorption. The transitions between *d* states give rise, in almost

all transition elements, to intense absorptions in the visible and also in the near infrared. Unfortunately studies on many transitional metal coordination complexes at 1.3 μm yielded similar results. Thus, whole areas of topical inorganic chemistry were inaccessible, e.g. the study of clays or compounds of certain well-defined and important oxidation states such as potassium manganate and Cu(II).

The Raman shift region at 1.3 μm is limited to a range less than 1800 cm^{-1} with the InGaAs detector. Further shift data (out to 3000 cm^{-1}) can be obtained by switching to an InSb detector, however this is inevitably accompanied by a significant increase in noise[1]. Detector manufactures would have to very convinced of its potential before investing capital in developing high performance devices operating out to 2.5 μm.

The problems encountered when studying samples at temperatures > 150 °C with FT Raman due to large thermal blackbody emissions are certainly exacerbated by the reduced sensitivity at 1.319 μm. Q-switched laser techniques[5] could to used to reduce the thermal background intensity and possibly increase the temperature at which samples can be studied.

The possibility for future applications with the 1.3 μm source are discussed in Chapter 5.

4.5 References:

1. D.B. Chase and T. Hirchfield, Appl. Spectrosc., 40 (1986) 133.

2. K.J. Asselin and B. Chase, Appl. Spectrosc., 48 (1994) 699.

3. J.Y. Kim, S. Ando, A. Sakamoto, Y. Furukawa and M. Tasumi, Synt. Metals, 89 (1997) 149.

4. B. Chase, Appl. Spectrosc, 48, 14A, (1994) 7.

5. P.J. Hendra, C. Jones and G. Warnes, Fourier Transform Raman Spectroscopy, Instrumentation and Applications, Ellis Horwood, Chichester, (1991).

6. C.J. Petty, G.M. Warnes, P.J. Hendra and M.J. Judkins, Spectrochim. Acta, (1991) 47A.

7. J.C. Devos, Physica, 20 (1954) 690.

8. B.Bennett, PhD Thesis, University of Southampton, (1996), Chapter 2.

9. Perkin Elmer, System 2000R Users manual, (1993).

10. M.V. Pellow-Jarmen, PhD Thesis, University of Southampton, (1994), Chapter 2.

11. Epitaax-Optical Devices, Large Area InGaAs Photodiodes, No. 3-91, (1991).

12. J.M. Charmers and G. Dent, Industrial Analysis with Vibrational Spectroscopy, The Royal Society of Chemistry (1997).

13. R.J. Lehnert, Ph.D. Thesis, University of Southampton, 1994.

14. S.J.A. Pope and Y.D. West, Spectrochim. Acta Part A. 51 (1995) 2011.

15. Y.D. West, Spectrochim Acta Part A 53 (1997) 35-42.

16. M. Lapp and C.M. Penney, Laser Raman Gas Diagnostics, Plenum Press, New York, (1974).

17. J.G. Radziszewski and J. Michl, Appl. Spectrosc. 44, (1990) 414.

18. H.M.M. Wilson, M.V. Pellow-Jarman, B. Bennett and P.J. Hendra, Vib Spectrosc., 10 (1996) 89.

19. B. Bennett, PhD Thesis, University of Southampton, (1996) Chapter 1.

5. Chapter Five: Conclusions

The objective of the work presented in this thesis was to develop FT-Raman spectroscopy using a variety of excitation wavelengths and to apply these spectroscopic methods to the study of polymer fibres and dyes.

These areas of research arose because the Southampton Applied Spectroscopy Group has over a considerable number of years dedicated itself to the application of FT-Raman and Infrared absorption spectroscopy to analytical science and in particular the study of polymers. There have been extensive contributions to the field using the excitation sources operating at 1.064 μm along with others at various wavelengths between the deep red and one micron wavelength. In contrast there has been a great deal less work carried out utilising other emission lines of the Nd:YAG laser as a Raman excitation source.

There has also been a longstanding programme at Southampton aimed at the effect of quench cooling on the crystallisation of polyolefins and other polymers. The role of cooling rate, molecular weight of the polymer, pressure and shear have all been investigated. However, the main difficulty in studying crystallisation kinetics is the need to achieve a high degree of control over the processing conditions. In particular the rates of extrusion, extension and heat transfer are thought to directly determine the mechanical properties of the final material. The conditions must be highly reproducible and achieved at a commercially realistic rate.

The specific aims of the project were as follows:

(i) To design/alter and experiment with a purpose built extruder incorporating a molten metal bath in efforts to maintain accurate control over the processing conditions for the production of polymer fibres (Chapter 2).

(ii) To conduct experiments to assess the affect of drawing fibres (produced with the molten metal bath) at elevated temperatures; to analyse a series of the resulting high modulus fibres for mechanical strength (Chapter 2).

(iii) To carry out a study of FT Raman spectroscopy at 1.3μm to access the level of sensitivity and investigate the possible potential applications for operation at this wavelength (Chapter 4).

The result obtained from the polymer studies was that high modulus polyethylene fibres attaining a tensile modulus of the order of 25 GPa and a tensile strength approaching 1 GPa can be produced by the process of extruding polyethylene through a molten metal bath (at 125 °C) and annealing, then further cold drawing at a particular temperature to a draw ratio of 15. Further studies of a series of these high modulus polyethylene fibres were carried out using Raman-microscopy[1,2]. Although my name was not listed as an author in these papers, I contributed significantly to the work. The results were achieved working in collaboration with Dr. S. Lu during his post-doctoral appointment at Southampton. In these studies the high degree of orientation in polyethylene fibres meant that upon 90° rotation of the sample and/or polarisation analyser, marked variations in band intensities occured throughout the spectra. Measurements of the 1131:1064 cm^{-1} band intensity ratio of the fibre were made and related to their Young's modulus. The 1131:1064 cm^{-1} band intensity ratio therefore can be related to Young's modulus of fibres and can be used to evaluate molecular orientation of the fibres.

Raman-microscopy was also used to investigate the melting point of high modulus polyethylene. The 1131:1064 cm^{-1} band intensity ratio was studied as a function of temperature and was related to the molecular orientation of polyethylene within the fibre. The microscopy study was carried out with a specially designed heating cell that enabled the melting temperature of both oriented and unoriented polyethylene specimens to be estimated. The 1131:1064 cm^{-1} band intensity ratio is indicative of molecular orientation, which changes dramatically as the melting point is approached. This technique, with

appropriate caution, can be useful in estimation of the melting point of both oriented and unoriented polyethylene specimens.

It is quite clear that this report as in perhaps every thesis is of course only an interim report. The thesis throws up more questions than it answers – the nature of scientific investigation. The results from the production of polyethylene fibres serve merely as an indication of the potential that molten metal bath melt spinning coupled with effective cold drawing offers for the production of high modulus fibres. A catalogue of engineering problems encountered during the project restricted the time necessary to carryout a comprehensive investigation into all the processing conditions. It is strongly felt that the results obtained can be further improved upon using a more suitable grade of polyethylene for the technology and varying the processing conditions. A wide range of characterisation techniques should be employed to fully understand the physical and morphological properties of the produced fibres, e.g. D.S.C., X.R.D. and FT Infrared and Raman microscopies, etc.

An investigation was also undertaken using the 1.319μm line from a Nd^{3+}:YAG laser as an excitation source for FT-Raman spectroscopy. Chase *et al* [3] indicated that using the 1.319 μm laser for FT Raman was considerably more useful laser line than 1.064 μm because fluorescence was reduced. I doubt this conclusion. There is little point in changing the laser wavelength for FT-Raman from 1.064 to 1.3 μm except for very specific examples. It is true that there is some reduction in fluorescence but for the most part the effect is not significant enough to justify its use. I would suggest that by pure chance the wavelength of the laser line for the Nd:YAG turns out to be the optimum. I am sure this has been indicated to some extent before. I feel it is clear that the use of red or deep red sources is of little advantage and that radiation around 1 micron is ideal and longer wavelengths simply present further problems. All the disadvantages associated with the use of NIR sources are exacerbated by using longer wavelength excitation.

One of the possible potential applications for the 1.3 μm excitation source is in the study of adsorbed species using SERS. In electrode studies using visible lasers, species adsorbed

to the electrode were shown to be both generated and removed by laser radiation[5]. As the photon energy in the near infrared is reduced, photochemical changes are less likely to be induced by the laser at 1.3 μm. SERS spectra frequently
appear over an intense fluorescence background which again might well be reduced or possibly avoided with the 1.3 μm source.

Another quite specific area worth investigating is in the field of conducting polymers. Tanaka's *et al* [4] showed the 632.8 nm excited Raman spectra of trans-polyacetylene (*t*-PA) doped with Na at various concentrations. As the Na concentration was increased, doping-induced Raman bands appeared at about 8 mol% and become dominant at 13 mol%. However, at dopant concentrations less than about 8 mol%, Raman spectra showed no significant changes from the case of pristine *t*-PA. Raman spectra taken with a laser line of wavelength longer than 1.064 μm are more informative, because the electronic absorption of Na-doped PA appear from the visible to infrared.

Furukawa *et al* [5] investigations demonstrated how Raman spectra of lightly to fully Na-doped PAs could be recorded at 1.3 μm. It should thus be possible to apply the 1.3 μm excitation source to other species that show similar absorptions to the above example.

References

1. S. Lu., P.J. Hendra and A.E. Russell *Journal of Materials Science* 33 (1998) 4271
2. S. Lu., P.J. Hendra and A.E. Russell *Spectrochimica Acta,* Part A 55 (1999) 3
3. K.J. Asselin and B. Chase, Appl. Spectrosc., 48 (1994) 699.
4. J.Tanaka, Y. Saito, M. Shimizu, C. Tanaka and M. Tanaka, Bull. Chem. Soc. Jpn., 60 (1987) 1595.
5. J.Y. Kim, S. Ando, A. Sakamoto, Y. Furukawa and M. Tasumi, Synt. Metals, 89 (1997) 149.